Magnetism of Chemically Modified Ultrathin Metal films and Nanorods Studied by Magneto-Optical Methods

A Thesis Submitted to
The Graduate University for Advanced Studies (Sokendai)
for the Degree of
Doctor of Philosophy

Ma, Xiao-Dong

Department of Structural Molecular Science,
School of Physical Sciences,
The Graduate University for Advanced Studies (Sokendai)

2006

Contents:

1 General introduction 1

1.1 Magnetic properties of reduced dimensional materials 5

1.2 Aims of this dissertation 20

2 Experimental techniques details 26

2.1 X-ray magnetic circular dichroism (XMCD) 26

2.2 Surface magneto-optical Kerr effect (SMOKE) 38

2.3 X-ray absorption fine structure (XAFS) 44

3 Magnetism of Co nanorods on Cu(110)(2×3)N 49

3.1 Introduction 50

3.2 Experiments 54

3.3 Structural properties 56

3.4 Magnetic anisotropy of Co nanorods 59

3.4.1 SMOKE results 59

3.4.2 XMCD results 63

3.5 Experimental results of critical behavior 66

3.6 Monte-Carlo simulation of the critical behavior 67

Conclusion: 70

4 Chemisorption effect on spin reorientation of Fe/Ag(001) 72

4.1 Introduction 73

4.2 Experiments 79

4.3 SMOKE results 81

4.4 XMCD results 84

4.5 Discussion: adsorption effect on spin reorientation 88

Conclusion: 93

5 Structure of novel molecular photomagnets of Cu-Mo cyanides 96

5.1 Introduction 97

5.2 Experiments 102

5.3 Electronic states from X-ray absorption near edge structure (XANES) 103

5.4 Structure from extended X-ray absorption fine structure (EXAFS) 108

5.5 Discussion 119

Conclusion: 121

6 Summarization 124

Acknowledgements 126

1 General introduction

Each milestone in the evolution of mankind is marked by the big breakthrough in materials, and for many centuries the discovery of magnetism has stimulated progress in science and technology. Magnetic materials and magnetic devices have occupied a major place in our lives for most of the twentieth century and played a very important role in the emergence of the digital computer by providing both ferrite core and plated wire memories. The investigation of magnetism, for a long time, had been focused on the macroscopic scale. Atomic scale magnetic phenomena, as exemplified by the exchange interaction, crystal field effect and spin-orbit interaction, were revealed in the first half of the last century and are still now under extensive exploration [1]. Nanomagnetism, which bridges the gap between atomic-scale magnetism and macroscopic magnetism of extended bulk and films, has received great attention in recent decades. The existence of varieties of nanostructure ranging from nanomagnets to artificial nanostructure is the direct reason for the scientific and technological importance of magnetic nanostructure. Moreover, the nanoscale and lowered dimensionality effect involved in explaining and improving the properties of advanced magnetic material has also largely accelerated the investigation of nanomagnetism. The last significant point is that the nanomagnetism has opened the door for new technology such as the emerging area of spintronics.

One of the applications for low dimensional magnetic nanostructure is the recording media technology. The magnetic thin film has long been used as recording media in the traditional longitudinal recording technology.

Nowadays there is a transition from traditional longitudinal to perpendicular recording technique. The popular explanation for the advantage of perpendicular recording is that it achieves higher storage densities by aligning the poles of the magnetic elements, which represent bits, perpendicularly to the surface of the disk platter, as shown in the Fig.1. In this not quite accurate explanation, aligning the bits in this manner takes less platter than what would have been required had they been placed longitudinally. So they can be placed closer together on the platter, thus increasing the number of magnetic elements that can be stored in a given area. This technique requires that the magnetic material with perpendicular magnetization. It is this

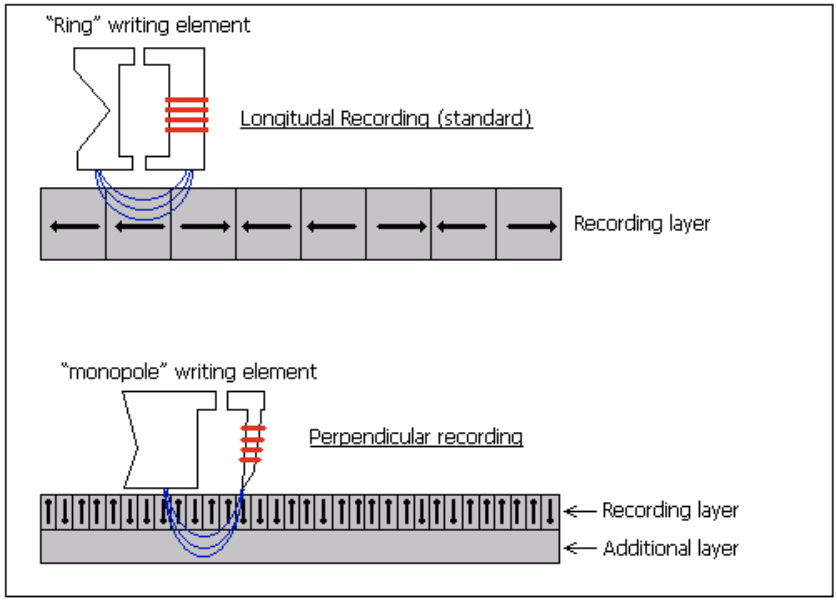

Fig.1 Longitudinal and Perpendicular recording illustration.

background that has triggered a great deal of fundamental research on understanding, exploring and manipulating perpendicular magnetization in magnetic thin film.

Another new research area emerging from nanomagnetic structure is the spintronics. Conventional electronic devices and data storage media are rapidly reaching their limits due to the increasing heat dissipation challenges of charge current and

quantum size effects in small devices. Spin electronics or in short spintronics along with nanofabrication technology are expected to ensure sustainable Moore's law in the future information technology(IT) industry [2]. Spintronics, which combines both the charge and spin degrees of freedom in the device with new functionality and upgraded

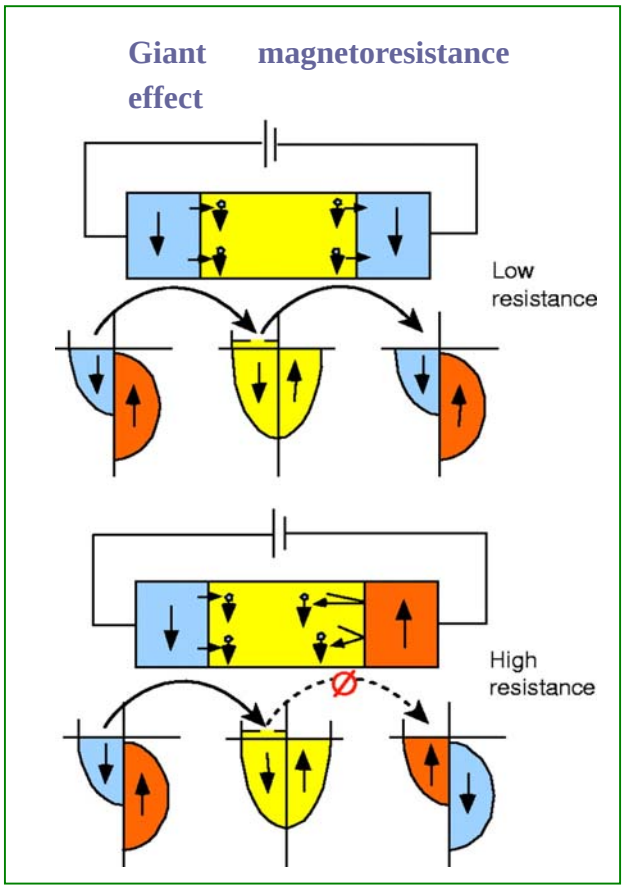

Fig.2 Schematic representations of spin-polarized transport from a ferromagnetic metal, through a normal metal, and into a second ferromagnetic metal for aligned and anti-aligned magnetic moments.

performance, are anticipated to be nonvolatile, versatile, fast, and capable of simultaneous data storage and processing while consuming less electric power. The heart of a spintronic device is a chip containing nanosized "spin transistors," which would operate using a "spin current" that flows only when the spins in the transistor's source and drain electrodes have the same orientation. Such a spin transistor could be used as either a very fast on-off switch or to store digital information. As an illustrative example [3] shown in Fig.2, the giant magnetoresistance effect (GMR) can be regarded

as the earliest prototype spintronic device. GMR is a quantum mechanical effect observed in layered magnetic thin-film structures that are composed of alternating layers of ferromagnetic and nonmagnetic layers. When the magnetic moments of the ferromagnetic layers are parallel, the spin-dependent scattering of the carriers is minimized, and the material has its lowest resistance. When the ferromagnetic layers are anti-aligned, the spin-dependent scattering of the carriers is maximized, and the material has its highest resistance. It has been estimated that the market for GMR related product is on the order of $1 billion per year and will increase the storage on a disk drive from 1 to 20 gigabits, merely by the incorporation of the new GMR materials.

In technology, the key to have a large GMR effect heavily relies on the quality of the magnetic thin film structure [4]. The indirect exchange coupling between the two magnetic layers is the decisive factor for GMR effect. This indirect coupling has an oscillatory behavior which favors either parallel (ferromagnetic coupling) or antiparallel alignment (antiferromagnetic coupling) depending on the non magnetic interlayer thickness. For a complete antiferromagnetic coupling, the interlayer must be uniformly thick in space. It has been gradually realized that the promise to all the emerging spintronic technology depends strongly on two pillars. One is to fabricate high quality magnetic nanostructure such as thin films, multilayers as well as much lower dimensional nanoobjects such as nanowire, nanorod as well as nanodot. This has not always been an easy task due to a fact that nanostructure growth is influenced by many parameters. Moreover thermodynamic nonequilibrium growing conditions along with the hybrizadation effect from the underneath substrate have also added more complexity to the artificially control the growth of nanostructure. Another one is to obtain a fundamental understanding of the magnetic behavior in nanostructure. This is much greater challenge because the nanomagnetism problem is closely related to distinctive

material with lowered dimensionality, symmetry, and crystallographic structure compared to the conventional bulk material which we have known for a long time. In the next section, I will summarize some fundamental concepts involved in the nanomagentism in low dimensional systems.

1.1 *Magnetic properties of nanostructure in low dimension*

Fundamental magnetic properties such as the spontaneous magnetization, the anisotropy, and the temperature dependence of ordered magnetic states in low-domensional nanostructure systems deviate substantially from those of bulk systems. We will present here some general properties in low dimensional nanosystem.

1.1.1. Magnetism of metallic ultrathin film:

It was once believed in the middle of the 1960s that a 2D system would not exhibit long range magnetic order at finite temperatures if the system is magnetically isotropic by both experiment and theory[5]. Although these results are now known to be inappropriate in theory and the artifacts from contamination in the film preparation process, they have stimulated great interest in studying magnetic properties of surfaces and thin films. The long-range magnetic ordering does exist in ultrathin film and is now revealed that the magnetic uniaxial anisotropy along with long-range dipolar interaction have played the decisive role in stabilizing ferromagnetic ordering. The following are several unique features found in 2D ultrathin magnetic films[6,7], which have made the 2D ultrathin film distinctive from 3D bulk material (PS: these features are also usually encountered in most 1D nanostructure).

(i) ***Magnetic anisotrop*:**

Phenomenological view of magnetic anisotropy

The magnetic anisotropy energy (MAE) is the change of the free energy of a crystal during the rotation of magnetization. It is very small (10^{-5}~10^{-6} eV/atom) compared to the exchange interaction (0.1~1eV/atom) in bulk Co, Fe, Ni) but it plays a very important role in describing the ferromagnetic property. The exchange interaction is invariant with rotation of the quantization axis of the spin S_i, namely, $S_i \cdot S_j$(scalar product) is completely isotropic. The MAE determines the preferential orientation and the stability of the magnetization within a ferromagnetic single domain. It is of both scientific and technological importance to gain the understanding of the principle involved in MAE.

Basically, there are two main sources for MAE: the shape anisotropy[8] which originats from the magnetostatic self-energy from the classical magnetic dipolar interaction and the magnetocrystalline anisotropy which is due to spin-orbit interaction. Due to its long range character, the dipolar interaction generally results in a contribution to the anisotropy, which depends on the shape of the specimen. It is of particular importance in thin films, and is largely responsible for the in-plane magnetization usually observed. The dipolar magnetostatic energy E_d can be expressed as

$$E_d = \frac{1}{2\mu_0} M_s^2 \cos^2\theta \qquad (1.1)$$

where μ_0 is the permeability of vacuum, M_s is the saturation magnetization and θ is angle between the magnetization and principle axis of the system. In the absence of spin–orbit and dipolar interaction, the total energy of the electron–spin system does not depend on the direction of the magnetization. In a localized picture the spins are coupled via the spin–orbit interaction to the orbit which, in turn, are influenced by the crystal lattice. For itinerant materials the spin–orbit interaction induces a small orbital momentum, which then couples the total (spin plus orbital) magnetic moment to the

crystal axes. This results in a total energy which depends on the orientation of the magnetization relative to the crystalline axes, and which reflects the symmetry of the crystal [9]. This is known as the magnetocrystalline contribution to the anisotropy. The lowered symmetry at an interface strongly modifies this contribution as compared to the bulk, yielding, as mentioned already, a so-called interface anisotropy as pointed out by Néel (1954). From a phenomenological point of view, the MAE for a uniaxial system is usually expressed as $E_a = -K_s \cos^2\theta$, here K_s is the effective anisotropy constant defined in J/m^3 or eV/atom. In conjunction with the overlap in wavefunctions between neighbouring atoms, the spin–orbit interaction is also responsible for the magneto-elastic or magnetostrictive anisotropy induced in a strained system, a situation which is frequently encountered in multilayers due to the lattice mismatch between the adjacent layers. In magnetic thin film systems, it is more convenient to distinguish volume anisotropy (K_v), and surface (interface) anisotropy(K_s/t, here, t is the thickness of magnetic layer), $K = K_{eff} = K_v + K_s/t$. The total magnetic anisotropy energy can be given phenomenologically as follow.

$$\Delta E = -\frac{1}{2\mu_0}\pi M_s^{\,2} + K_v + K_s/t$$

Usually a positive ΔE indicates perpendicular magnetization and a negative value of ΔE represents an in-plane magnetization. The sign of ΔE is variable due to the variation in surroundings such as thickness and temperature as well as some adsorption on surface. The sign change ΔE is accompanied by a phenomenen called ***spin reorientation*** which showes the easy axis of the magnetic system has changed from one direction to another.

Physical origin of magnetic anisotropy driven by spin- orbit interaction

The physical origin of the magnetocrystalline anisotropy still remains largely in

controversial within theoreticians [10-15]. The idea that the spin-orbit interaction plays a decisive role in magnetic anisotropy comes from Van Vleck and can be traced back to more than 60 years ago. Only recently, however, Bruno [14] has put the basis for a perturbative treatment of the spin-orbit coupling which allows to derive the anisotropy constants from the unperturbed tight-bonding band structure. This treatment has the advantage of providing intuitive physical insights over *ab initio* methods and will be briefly outlined here. Another important reason to outline the physical origin of magnetocrystalline anisotropy here is to motivate our XMCD experiments and to provide a context in which the measured XMCD results can be interpreted.

Assuming that the origin of the magnetic anisotropy(shape anisotropy excluded) is essentially due to the spin-orbit interaction (SO):

$$H_{so} = \xi S \cdot L \qquad (1.2)$$

where ξ is the spin-orbit interaction constant. The spin-orbit interaction is quite localized and the constant ξ depends on the variation of the potential near the nucleus and does not vary too much for either a free atom or a solid. In addition,since for 3*d* transition metals ξ is between 30~80meV, which is small compared to the *d* bandwidth of a few eV, we can treat Eq.(1.2) as a perturbation of the Hamiltonian that describes the 3*d* electron states. The anisotropy energy can be given by

$$E_a = E_{so}(\hat{S}_z) - E_{so}(\hat{S}_x) = \Delta E_{so} \qquad (1.3)$$

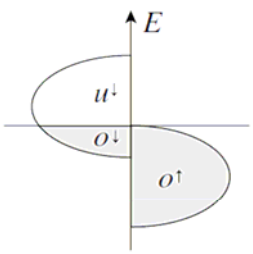

where $E_{so}(\hat{S})$ represents the spin-orbit correction to the unperturbed Hamiltonian for a given direction $\hat{S}$ of the magnetization. For partity resons the lowest-order contribution to the SO induced change in the total energy is second order:

$$E_{so}(\hat{S}) = \xi^2 \sum_{o,u} \frac{|\langle o | S \hat{S} \cdot L | u \rangle|^2}{\varepsilon_o - \varepsilon_u} \qquad (1.4)$$

where o and u represent the occupied and unoccupied states, respectively. For the limit case of strong exchange splitting (which is good approximation for Co), we may consider that the spin-up band is almost fully occupied, and all empty states belong to the spin-down band, as in Fig.. We can therefore exclude the effects from the empty spin-up states in Eq.(1.4), and have:

$$E_{so}(\hat{S}) \approx -E_{so}^{\downarrow\downarrow}(\hat{S}) - E_{so}^{\uparrow\downarrow}(\hat{S}) \quad (1.5)$$

where

$$E_{so}^{\downarrow\downarrow}(\hat{S}) = \frac{\xi^2}{4} \sum_{o^{\downarrow},u^{\downarrow}} \frac{|\langle o^{\downarrow} | \mathrm{S}\,\hat{S}\cdot L | u^{\downarrow}\rangle|^2}{\varepsilon_{o}^{\downarrow} - \varepsilon_{u}^{\downarrow}} \quad (1.6)$$

$$E_{so}^{\uparrow\downarrow}(\hat{S}) = \frac{\xi^2}{4} \sum_{o^{\uparrow},u^{\downarrow}} \frac{|\langle o^{\uparrow} | \mathrm{S}\,\hat{S}\cdot L | u^{\downarrow}\rangle|^2}{\varepsilon_{o}^{\uparrow} - \varepsilon_{u}^{\downarrow}} \quad (1.7)$$

and $o^{\downarrow}(u^{\downarrow}), o^{\uparrow}(u^{\uparrow})$ represent occupied(empty) majority and minority spin states. It can be shown that the terms $E_{so}^{\downarrow\downarrow}$ and $E_{so}^{\uparrow\downarrow}$ derived from Eqs. 1.3 and 1.5 have opposite sign. However, the spin flip contribution $E_{so}^{\uparrow\downarrow}$ is one order of magnitude smaller than $E_{so}^{\downarrow\downarrow}$ in 3*d* metals due to the large exchange splitting ($\Delta_{ex} \approx \varepsilon_{u}^{\downarrow} - \varepsilon_{o}^{\uparrow} \approx 3\mathrm{eV}$) [11,15], and it will be neglected in the following treatment. Within this approximation the anisotropy energy in Eq.1.3 can be written

$$E_a = E_{so}^{\downarrow\downarrow}(\hat{S}_z) - E_{so}^{\downarrow\downarrow}(\hat{S}_x) = \frac{\xi^2}{4} \sum_{o^{\downarrow},u^{\downarrow}} \frac{|\langle o^{\downarrow} | L_z | u^{\downarrow}\rangle|^2 - |\langle o^{\downarrow} | L_x | u^{\downarrow}\rangle|^2}{\varepsilon_{o}^{\downarrow} - \varepsilon_{u}^{\downarrow}} \quad (1.8)$$

The spin-orbit driven magnetic anisotropy depends on the number of spin-down electrons(band filling) because of the sum over the $o^{\downarrow}$ and $u^{\downarrow}$ states, and on the orbital character of the occupied states, on their coupling with the empty states through the orbital momentum operator, and on the minority spin band width ($\varepsilon_{o}^{\downarrow} - \varepsilon_{u}^{\downarrow}$). It is easy to recognize in the above expression the expectation values of the orbital momentum $\langle L \rangle$ in the directions x and z given by first –order perturbation theory:

$$\left\langle L_{x,z}\right\rangle = \sum_{o,u} \langle u \mid L_{x,z} \mid o\rangle \frac{\langle u \mid H_{so} \mid o\rangle}{\varepsilon_o - \varepsilon_u} + c.c.. \qquad (1.9)$$

Note that the $\langle L\rangle$=0 for the filled spin-up band, therefore the sum in Eq.1.9 is restricted to spin-down states. By substituting the expression for $\langle L\rangle$ into Eq.1.8 we obtain the fundament expression of magnetic anisotropy:

$$E_a = \frac{\xi}{4}(\langle L_z\rangle - \langle Lx\rangle = \frac{\xi}{4\mu_B}(\mu_L^x - \mu_L^z), \qquad (1.10)$$

where μ_L^x and μ_L^z represent the projection of the orbital magnetic moment in the x and z directions, respectively. The spin-orbit energy anisotropy is therefore proportional to the orbital momentum anisotropy of the minority band. The easy magnetization direction is given as the direction with largest component of **L,** In transition metals, the orbital momentum is determined by the interplay of the spin-orbit coupling with the much stronger crystalline field interaction. As a consequence, we obtain different values of **L** if the spins are oriented along different crystal directions by a strong external magnetic field. The relationship between the orbital momentum and the magnetic anisotropy has been experimentally verified by Weller [16] and by Dürr [17] et al. In the presence of an external magnetic field applied in a direction other than the easy axis, the spins will tend to follow the external field. The rotation of the orbital magnetic moment, on the other hand, is partially counteracted by the crystal field, which pulls u_L towards the easy axis. Because of the spin-oribit interaction which couples u_s to u_L, the rotation of the spin will also be affected. Hence, the energy that is necessary to turn the overall magnetization(which is mainly due to u_s) is proportional, through the spin-orbit constant, to the difference of the orbital magnetic moments that 'pull' the spins along and away from the easy axis.

A further point remains to be addressed: the magnetic anisotropy has been

calculated as a second order perturbation due to spin-orbit interaction. The reason to deal with this by second order is as follows. In fact, in Eq.1.10 ξ appears only in first order. The point is the spin-orbit interaction is also responsible for the non zero expectation values of the orbital momentum operator L in Eq.1.9; in other words, there would be no net orbital momentum without the spin-orbit interaction. This is easy to understand in 3D cubic crystal: The electronic states created by the crystal field alone (the $d_{x^2-y^2}, d_{3z^2-r^2}, d_{xy}, d_{xz}, d_{yz}$ states) posses no orbital momentum, since all d orbitals have a perfect balance of $\pm m_l$ (± 2, ± 1 ,0) contributions [Here $d_{x^2-y^2} = 1/\sqrt{2}(|2+2\rangle + |2-2\rangle)$ $d_{xy} = i/\sqrt{2}(|2+2\rangle + |2-2\rangle)$ $d_{3z^2-r^2} = |20\rangle$ $d_{yz} = i/\sqrt{2}(|2+1\rangle + |2-1\rangle)$ $d_{xz} = 1/\sqrt{2}(|2+1\rangle + |2-1\rangle)$]. The m_l balance is broken by the spin-orbit interaction which mixes different d orbitals in a way to produce a non-zero angular momentum. Since this momentum is small, the magnetic anisotropy is also very small, the order of 10^{-6} eV/atom. It is also intuitive from Eq.1.10 that a high symmetry environment does not favor the SO interaction related magnetic anisotropy. In low dimensional systems such as thin films and small cluster, nanowire, however, the crystal field does not quench the orbital momentum as it does in cubic systems. Its direction is determined by the particular symmetry of the system; however, in the absence of long range interaction, the orientation of single moments is free to fluctuate and the net orbital moment of the system is zero. It is the spin-orbit interaction which defines, trough the long-range exchange interaction carried by the spin, a common orientation for all the atomic orbital moments.

From the above it is apparent that low dimensional structures should have larger u_L values with respect to bulk crystals. Enhanced orbital moments have in fact been observed with XMCD for Co films on Cu(100) [18], for Co clusters on Au(111) [19] and in a number of other systems [20]. Larger values of the magnetic anisotropy are

also expected: asymmetric bonding configurations will result in an anisotropic d electron distribution and correspondingly in a marked anisotropy of the orbital momentum. As an example given in Fig.4, the case of a free-standing Co monolayer. Asymmetric bonds result in different in-plane and out of plane bandwidth, $W^{//}$ and $W^{\perp}$, respectively. The orbital momentum is basically related to the freedom degree of the electron and its value of orbital moment is determined by the average bandwidth W which determines the average separation of the filled and empty states which are mixed by the spin-orbit interaction. For a free standing monolayer, the out of plane DOS has a narrower bandwidth because of smaller overlap (π bonding) with atoms on the layer surface relative to the in plane DOS (σ bonding). Therefore narrow bandwidth is expected to contribute a larger orbital momentum, as illustrated in Fig.3 Because the orbital momentum direction is perpendicular to the plane of the orbiting electrons, the in-plane momentum is determined by the out-of-plane orbitals and their bandwidth and vice verse. A perturbation treatment gives u_L or $m_o \propto \xi / W$, where ξ is the spin-orbit interaction constant with the value~70meV, and W is the bandwidth.

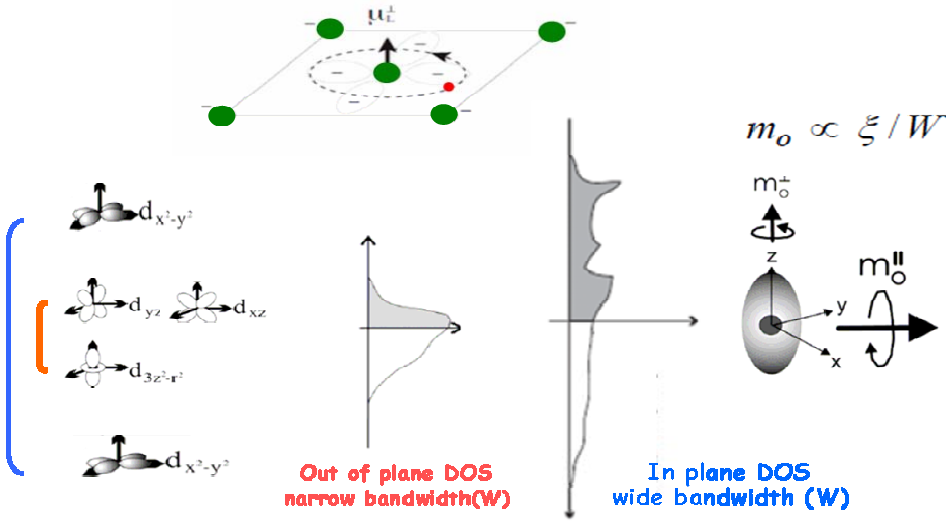

Fig.3 Origin of the orbital magnetic moment illustrated in a d-orbital based bonding model as long as with projected densities of states (DOS)

(ii) Curie temperature and critical behavior

Dimensionality of a magnet has effect on its temperature dependence of magnetic order. The Curie temperature, which separates the ferromagnetic and paramagnetic phases, is determined by the strength of magnetic anisotropy and dipolar interaction because the Mermin-Wagner theorem mentioned before [5] shows that isotropic exchange interaction gives no long-range order. Because the strength of both magnetic anisotropy and dipolar interaction are often smaller than the strength of exchange coupling, the Curie temperature is, not surprisingly, reduced for a 2D film. However, as pointed out by Erickson and Mills [21], the Curie temperature of the films increases with thickness and will be close to that of the bulk when the films reach several monolayer thickness. The thickness dependence of the Curie temperature is most properly expressed by finite-size scaling theories [22], which were backed by various experimental results on ultrathin films of Fe [23] , Co [24], and Ni [25].

The temperature dependence of spontaneous magnetization near the Curie temperature is called the critical behavior, which is often characterized by the exponent of a phenomenological power-law fitting of the magnetization vs. temperature data ($M = M_0(1-T/T_C)^{\beta}$,where M and M_0 are the magnetizations at temperatures T and T=0, respectively, and Tc the Curie temperature). The smaller the power-law exponent (β), the faster the magnetization falls to zero when approaching the Curie temperature. The amplitude of the power law exponent depends on the anisotropy and the dimensionality of the magnetic system. Generally the lower the dimensionality, the smaller the power-law exponent. Huang et al. have reported the values of the power-law exponents for various ultrathin films and their cross-over from 2D to 3D when increasing the film thickness [26].

However, it is worthwhile mentioning here that so far little is known for the critical

behavior regarding one-dimensional nanostructure. In this thesis, we have for the first time investigated both experimentally and theoretically the critical behavior for one dimensional Co nanorods grown on Cu(110)(2×3)N surface with several atoms wide . A full description regarding this issue will be given in chapter 2.

(iii) Enhancement of spin and orbit magnetic moment

The enhancement of the magnetic moment in a 2D system can be generally attributed to the reduced nearest neighbor coordination atoms and can be understood as follows [8]. The reduced coordination will narrow the d-bands and in general increase the density of states at the Fermi level. An LDA calculation for a 3d atom will spin-polarize and have the maximum moment permitted by the exclusion principle. The intra-atomic exchange which will spin polarizes the atom is the principal factor driving a system to ferromagnetism. The factor opposing ferromagnetism is that the creation of a moment in paramagnetic system requires that a certain number of electrons be transported from spin band across the Fermi level to the other spin band. The cost is in energy to do this is inversely proportional to the density of states at the Fermi level. Thus reduced coordination will in general favor the onset of ferromagnetism and, because it makes the atoms of a system more atomic-like, will cause an increase in the moment per atom. Take Fe as an example, the magnetic moment of an Fe atom is $4.0\,\mu_B$ in isolated form, and is reduced to $2.2\,\mu_B$ in bulk crystal (eight nearest neighbors). A 2D Fe film, which has an intermediate numbers of nearest neighbors, should thus have a moment between that of the bulk and a free atom. Theoretical calculation of a free-standing Fe (100) single-atomic-layer (monolayer) thick film has indeed revealed a moment of $3.07\,\mu_B$ [27]. An Fe film has to be supported by a substrate. Since the electronic hybridization between film and substrate

often counteract with the reduced dimensionality, the best substrates are those whose electronic structure is clearly separated from that of the substrate. Fe on Ag(001) system represents a very good example. Fig.4 shows energy bands along high-symmetry directions for a monolayer of Fe on Ag(001) [28]. Majority spin bands are on the left and minority-spin bands are on the right. In (a) are those bands that are odd with respect to reflection in the mirror plane perpendicular to the surface and (b) exhibits the even bands. The solid (dashed) energy bands correspond to wave functions symmetric (anti-symmetry) with respect to the reflection in the $z = 0$ plane. The Fe *d* bands lie essentially within the horizontal solid lines above

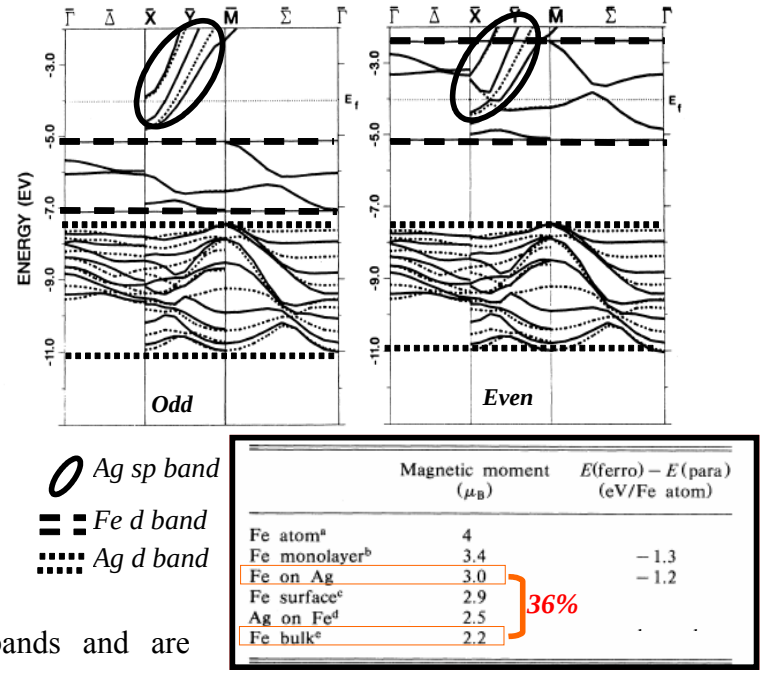

	Magnetic moment (μ_B)	E(ferro) − E(para) (eV/Fe atom)
Fe atom[a]	4	
Fe monolayer[b]	3.4	−1.3
Fe on Ag	3.0	−1.2
Fe surface[c]	2.9	
Ag on Fe[d]	2.5	
Fe bulk[e]	2.2	

36%

the Ag *d* bands and are quite narrow. Also the Ag minority-spin *d* bands differ relatively little from the majority-spin bands, while the *sp* bands show large difference. The most striking feature of Fig.1 is the large splitting between minority- and majority- spin d bands of Fe. This 3d splitting is slightly larger than the Fe d-band width, leading a separation of majority- and minority-spin bands. This system is extremely unique because the Fe d bands do not overlap the Ag d bands even after spin polarization. The total energy difference listed

Fig.4 The band structure feature of epitaxial Fe thin film grown on Ag(001)

in Fig. confirms this. The total energy of the Fe/Ag(100) system is lowered by 1.2 eV per Fe atom as a result of spin polarization, that of the isolated Fe monolayer is lowered by1.3eV. Thus the change in binding energy of Fe layer to the Ag is −0.1eV, the bond is weakened very slightly. Enhanced magnetic moments have also been observed in ultrathin film systems such as Fe/ W(1 1 0) [29] and Fe/MgO(1 0 0)[30]. Experimental measurements of magnetic moments of 2D films are generally very challenging, although torsion magnetometry and polarized neutron reflection as well as X-ray magnetic circular dichroism(XMCD) have been successfully applied. In this respect, theoretical calculation based on the first principle usually has big advantage to provide very reliable results in calculating magnetic moment.

Recently, it has also realized that the orbital magnetic moment can be strongly enhanced in reduced dimension material. Various reasons have been put forward to explain the enhancement of the orbital moment at the surface [15].

① at the surface the d band is narrower, resulting in an increase of the spin moment. This can be understood as follows. The net orbital moment is composed of a spin-up and a spin-down electron contribution, each with a different sign. If one spin band is filled, the orbital moment associated to this band is zero. Thus a large spin moment, which saturates one spin band and has a nonnegligible occupation of the other spin band, enhances the orbital moment.

② The symmetry is reduced at the surface, which can remove the quenching of the orbital moment, that often occurs in high lattice symmetries, such as cubic structure.

③ The density of states (DOS) at the Fermi level, E_F on surface, is larger than in the bulk because a large DOS at E_F results in an enhanced orbital moment. This can be understood by considering the spin-orbit interaction ΔH_{SO} as a weak perturbation. With $\Delta H_{SO} = \xi / 2s \cdot l$ we obtain, to first order in the spin-orbit parameter ξ, for the expectation

value l_z of l in the direction of the magnetization,

$$l_z \cong -\xi \frac{1}{\pi} \mathrm{Im} \int^{E_F} dE\{[4g_e^{(+)}(E) + g_t^{(+)}(E)] \times g_t^{(+)}(E) - [4g_e^{(-)}(E) + g_t^{(-)}(E)] \times g_t^{(-)}(E)\}$$

where $g_e^{(\pm)}(E)$ and $g_t^{(\pm)}(E)$ are the tight-binding matrix elements of the nonrelativistic impurity Gree's function for e_g and t_{2g} symmetry and for the (+) or(-) spin direction. If we assume, as in the Anderson model, that the e_g and t_{2g} Green's functions are degenerate, and that the local density of states are Lorentzian, then the energy integration can be carried out analytically, yielding

$$\langle l_Z \rangle \cong -\xi[n^{(+)}(E_F) - n^{(-)}(E_F)]$$

where $n^{(+)}(E)$ and $n^{(-)}(E)$ are the local *d* densities of states for spin-up and spin-down direction. If we assume the spin-up band is completely filled, the large DOS near the Fermi level will cause an increase of orbital momentum

④ Surface roughness, interdifussion, steps and terraces increase the electron localization, leading to more localized wave function with increased orbital moments compared to the bulk.

⑤ Thin film can give a confinement of the electronic wavefuntion leading to symmetry breaking and localization.

⑥ Thin films can show a strain-induced anisotropy due to the lattice mismatch of the substrate, which breaks the lattice symmetry of the film. For example, the Ni/Cu(001) shows Perpendicular magnetic anisotropy with face-centered tetragonal symmetry(fct) from the mismatch

1.1.2 One dimensional nanostructure

In theory, the magnetic behavior of condensed matter system is usually described either in terms of localized moments(Heisenberg model) or in terms of itinerant electrons belonging to exchange split bands (Stoner model). The Heisenberg model is

particularly suited for treating the thermal properties and explains the formation of magnetic domains. On the other hand, it does not take into account the delocalization of the valence electrons in a metal which is responsible for the observed non-integer values of the magnetic moments as illustrated in the Fig.5. The itinerant feature in Stoner model has the advantage of being consistent with general band theory and describes fairly well the transport properties of magnetic materials. However, it cannot describe the spatial dependence of the magnetization. Unfortunately, the reality is neither of the

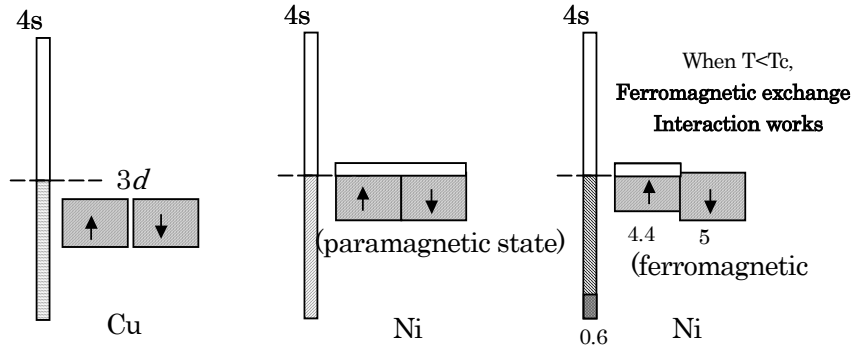

Fig.5 Band model of for the non-integer value of magnetic

two models has succeeded in building a unified theory of magnetic phenomena based on realistic physical assumption. For a system of Co nanorod on Cu(110) surface, which will address in detail in chapter 2, by taking into the metallic substrate effect on the magnetic anisotropy into consideration, the band structure based stoner model will be considered more appropriate.

As mentioned before, Mermin and Wagner theorem does not give ferromagnetism for 1D and 2D spin lattice with periodic boundary conditions [5]. As it is, it excludes any long range magnetic order for systems which can be described by the Heisenberg Hamiltonian

$$H = -\sum_{i,j} J_{ij}(r) S_i \bullet S_j - g\mu_B B \cdot \sum_i S_i \quad (1.11)$$

where i j are lattice point labels, $J_{ij}(r)$ the exchange interaction parameter and has

spatial dependence on r. B is an external field and g is the Lande factor. However, it takes only a tiny modification of this Hamiltonian such as, e.g. the introduction of dipolar coupling or an arbitray small anisotropy of spin-orbit origin, to obtain a ferro-(or antiferro-) magnetic 2D system [32]. The Ising model, which can be regarded as a particular anisotropic version of Eq.1.11, does give stable ferromagnetism in 2D, but it predicts zero mangetizaion at zero applied field for a 1D system. This result, which is often cited in conjunction with studies of low-dimensional magnetic structures, is actually correct only in the thermodynamic limit, i.e. for structures made of a large number of atoms. Consider a chain consisting of N spins described by the Ising Hamiltonian $H = -J\sum_{i=1}^{N-1} S_{zi}S_{zi+1,}$ with J>0(ferromagnetic coupling). The ground state energy of the system is $E_0 = -J(N-1)$ and corresponding to the situation where all spins are aligned. The lowest lying excitations are those in which a single break occurs at any of the N sites, as shown below:

Ground state

Lowest excited state

There are N-1 such excited states, all with the same energy $E = E_0 + 2J$. At temperature T the change in free energy due to these excitations is $\Delta G = 2J - k_B T \ln(N-1)$. For $N \to \infty$ we have ΔG <0 at any finite temperature and it is clear that the ferromagnetic(ground)state becomes unstable against thermal excitations. For $(N-1) < e^{2J/k_B T}$, however, the argument does not hold any more.

1D nanostructure can only be prepared by deposition onto a specified substrate in the experiments. The redistribution of the electronic states due to the hybridization with the substrate can lead to substantial changes in the magnetic behavior of the supported wires. Pastor and Dorantes-Davila have caculated in a tight-binding approach that one

of the major effects due to the presence of a metallic substrate is on the magnetic anisotropy of the wires [31]. Their results predict a strong magnetic anisotropy reduction (from 10 to 1 meV/atom) in passing from free-standing wire to Pd(110) supported wires, accompanied by a rotation of the easy axis of magnetization from the longitudinal to the tranverse direction perpendicular to the substrate.

Experimentally a large number of work on 1D magnetism were performed on organic or inorganic compounds with chains of 3d ions. The large intra-chain interaction (on the order of 10-100 K) and a much weaker inter-chain interaction (typically 100 or 1000 times smaller) have made these compounds quasi-1D magnetic systems. These compound materials have provided a large playground to study some fundamental magnetism issues such as 1D magnetic excitations and correlation between magnetic order and chain‧chain interactions[33,34].

So far only a very limited amount of work has been done on 1D magnetic nanostructure. The magnetic measurements were pioneered by Elmers et al. on Fe stripes grown on W(1 1 0) substrate [35]. These Fe stripes showed a strong in-plane anisotropy perpendicular to the stripe axis and a magnetic critical behavior similar to that of a 2D film with uniaxial anisotropy, despite their quasi-1D appearance. The details on this topic and some other 1D nanostructure including the atomic chain will be fully described in chapter 2.

1.2 The aim of this dissertation:

In this thesis, I am going to tackle the following targets.

(i) The magnetic anisotropy for the nanorods with several atoms width and height.

(ii) Critical behavior of one-dimensional nanostructure [the nanorod in (i)].

(iii) Origin of the gas adsorption induced spin reorientation on Fe/Ag(001) ultrathin film

(i) Local structure and electronic state of Cu-Mo cyanide molecular magnets.

As the aforementioned, when dimensionality and size of a physical system is reduced, the magnetic ordering tends to become more complicated as the fluctuations become relatively more pronounced. For instance, magnetic nanorod array with diameter of 30nm buried in a self-organized porous alumina nanohole template shows easy axis along the rod indicating the shape anisotropy is the dominating. However, the study of atomic Co chains on Pt(997) revealed a perpendicular magnetization with respect to the chain axis. This shows that the spin-orbit interaction rather shape anisotropy has become dominating for magnetic anisotropy when the size is ultimately reduced. On the other hand, the critical behavior in low dimensional material represents another fascinating topic although no data regarding The value of the critical exponent β of one-layer ribbons on stepped W(110) has been reported to be close to the two-dimensional Ising model while quite less than that of three-dimensional one. However, so far there is no report concerning magnetic anisotropy and critical behavior of one-dimensional nanostructure within several atoms width and several atoms height. This is mainly because the magnetic layers in these previous studies grow on step edges of the substrate surfaces in a layer-by-layer fashion and the one-layer ribbon structure is eventually merged before the second or higher layer grows.In this thesis, I have succeeded for the first time in the investigation of the critical behavior of and magnetic anisotropy of Co nanorods within several atoms range by cooperating with a STM group (Prof. Leibsle) at University of Missouri, Kansas city. The novel results from this research will fill the gap between magnetic properties of atomic-chain and large scale nanorods(>20nm). And the results

for the magnetic critical behavior of this nanorod will be the first reliable report for the one-dimensional nanostructure.

Meanwhile, the chemisorption effect on the magnetic anisotropy of Fe ultra thin film on Ag(001) surface is also studied systemically in this thesis. It is well known that the variation in surroundings such as chemical adsorption can have a significant effect on the morphology in thin film, which accordingly alters the magnetic anisotropies, resulting in the spin reorientation toward the easy axis of the magnetization. Previous study of Fe/Ag(001) system revealed a destabilization of perpendicular magnetization due to the oxygen adsorption but failed to provide a sound proof to show what is the causation for this spin reorientation. The answer to this problem has been wrapped in mystery since then. It is therefore the purpose of this work to tackle this subject and probe what is decisive factor responsible for the observed destabilization of perpendicular magnetization after oxygen adsorption. In order to clarify this puzzle, we have performed a systematic investigation on the effect from surface chemisorption by comparing with three different gases adsoption behavior measured by surface MOKE and XMCD.

The last part of this thesis contains the determination of local structure and electronic state of a novel molecular photomagnets of Cu-Mo cyanides. This photomagnet is unique for many reasons. The photoinduced phase is essentially different in this sample because unlike all the other samples studied, there is no high temperature phase in this sampler Moreover, these compounds, which show ferromagnetism, consist only of magnetic ions of Cu and Mo, which seldom exhibit ordered magnetism. No typical magnetic ions such as Mn, Fe, Co, or Ni are present. In addition, the change of local structures around Cu in a redox cycle is an important issue in catalysis and biology. The results from this study are expected to provide a deep

insight into these regards.

Reference:

[1] Skomski J. Phys.: Condens. Matter 15 R841–R896(2003).

[2] Y.B Xu Spintronic Materials and Technology , Taylor & Francis Group publish

[3] Gary A. Prinz SCIENCE Vol 1660 282

[4] J. Shen , J. Kirschner Surface Science 500 300-322 (2002).

[5] N.D. Mermin, H. Wagner, Phys. Rev. Lett. 17 1133. (1966)

[6]M. Bander, D.L. Mills, , Phys. Rev. B 38 12015 (1988).

[7] Y. Yafet, J. Kwo, E.M. Gyorgy, , Phys. Rev. B 33 6519 (1986).

[8] J.A.C Bland B. Heinrich ultrathin magnetic structures I Springer 1992.

[9] M T Johnson, et al, Rep. Prog. Phys. 59 1409-1458 (1996).

[10] G. Daalderop, P.Kelly, M.Schuurmans, Phys.Rev.B 50, 9989 (1994).

[11] J. Dorantes-Dávila* and G. M. Pastor Phys. Rev. Lett. 81, 208 - 211 (1998).

[12] Ding-sheng Wang Phys. Rev. B 47, 14932 - 14947 (1993).

[13] I. V. Solovyev Phys. Rev. B 52, 13419 - 13428 (1995).

[14] Patrick Bruno Phys. Rev. B 39, 865 - 868 (1989).

[15] G. van der Laan, J. Phys.: Condens. Matter 10, 3239 (1998).

[16] D. Weller et al Phys. Rev. Lett. 75, 3752 - 3755 (1995).

[17] H. A. Dürr et al Science 277 213-215. 1997.

[18]M. Tischer Phys. Rev. Lett. 75, 1602 - 1605 (1995).

[19] H. A. Dürr Phys. Rev. B 59, R701 - R704 (1999).

[20] S. S. Dhesi Phys. Rev. B 60, 12852 - 12860 (1999).

[21] R.P. Erickson, D.L. Mills, Phys. Rev. B 43 11527 (1991).

[22] M.E. Fisher, M.N. Barber, , Phys. Rev. Lett. 28 1516; (1972).

[23] M. Stampanoni, et al, Phys. Rev. Lett. 59 2483(1987).

[24] C.M. Schneider, et al Cu(100) surfaces, Phys. Rev. Lett. 64 1059 (1990).

[25] R. Bergholz, et al . J. Magn. Magn. Mater. 45 389(1984).

[26] F. Huang, et al. Phys. Rev. B 49 3962 (1994).

[27] C. Li, et al. Phys. Rev. B 43 780(1991).

[28] Roy Richter, et al. Phys. Rev. Lett. 54, 2704 - 2707 (1985)

[29] U. Gradmann,et al, Appl. Phys. A 49563 (1989).

[30] J.A.C. Bland, J. Magn. Magn. Mater. 104 (1992) 1909

[31] J. Dorantes-Dávila , G. M. Pastor Phys. Rev. Lett. 81, 208 - 211 (1998).

[32] Myron Bander and D. L. Mills Phys. Rev. B 38, 12015 - 12018 (1988).

[33] M. Hase, et al , Phys. Rev. Lett. 70 3651(1993).

[34] F.D.M. Haldane, Phys. Rev. Lett. 50 1153(1983).

[35] H.J. Elmers, el al Phys. Rev. Lett. 73 898(1994).

2.1 X-ray magnetic circular dichroism (XMCD):

Synchrotron radiation in the soft x-ray(100eV~2000eV) allows access to the strong dipole-permitted (core 2p→valence 3d) excitations in transitional –metal ferromagnets, and (core 3d, 4d→valence 4f) in rare-earth magnetic materials. X-ray absorption experiments with polarized light in this energy range allow therefore extracting great deal of information on the magnetic states of such system. After the first practical demonstration of x-ray magnetic dichroism (XMD) using linear polarized light in 1986, XMD with circular dichroism has been developed both experimentally and theoretically into a powerful quantitative magnetometry tool. XMCD is element-specific, has sub-monolayer sensitivity, and can be used to measure magnetization loops. It allows us to identify the moment orientation in ultrathin films of magnetic materials, unique among surface-sensitive magneto-optical techniques, to determine the spin and orbital magnetic moments separately of elements together with their anisotropies.

The absorption of polarized light by a magnetized sample depends on the orientation of magnetization **M** relative to the light polarization direction. XMCD is defined as the difference in the absorption coefficients for parallel and antiparrallel orientation of the magnetization direction of the sample with respect to the helicity of the circularly polarized exciting light. For 3d transition metals the dipole selection rules allow the following transitions:

-K 1s ---- $4p_{1/2}$

-L_2 $2p_{1/2}$----------$3d_{3/2}$, 4s

-L_3 $2p_{3/2}$ ---------$3d_{3/2,\ 5/2}$, 4s

where the subscript indicates the total angular momentum quantum number *j*. The properties of 3d electrons are probed.

Single particle models

In calculation soft X-ray core-level absorption and XMCD spectra in 3d transition metals, two simple atomic models have been used, besides more complex band structure calculations. The first one, so called Erskine-Stern model, is based on the single-particle model of optical transition from a core state of prescribed symmetry into valence-band states with symmetry corresponding to allowed dipole transitions. Only the core states are treated relativistically (spin-orbit split levels) and we make the assumption that the empty valence-band states are exclusively of minority character. We treat here the case relevant for the L_3 and L_2 edges.

From the dipole approximation principles it allows that the absorption coefficient μ is proportional to the square of the matrix element of angular part.

$$\langle \phi_f \mid \varepsilon \cdot r \mid \phi_i \rangle$$

The initial 2p states are split by the spin orbit interaction into two levels, which in the $|jm\rangle$ base are given by $|\frac{1}{2}m\rangle$ and $|\frac{3}{2}m\rangle$, degenerate with respect to $m=-\frac{1}{2},\frac{1}{2}$ and $m=-\frac{3}{2}-\frac{1}{2},\frac{1}{2}\frac{3}{2}$ respectively. Since the spin-orbit interaction is neglected in the final states, the latter can be described in the $|l_z s_z\rangle$ representation or equivalently in the spherical harmonics $Y_{l,l_z}^{s_z}$ representation. The $\varepsilon \cdot r$ operator can be expressed as

$$\varepsilon \cdot r = \sqrt{\frac{4\pi}{3}(\varepsilon_z Y_{1,0} + \frac{-\varepsilon_x + i\varepsilon_y}{\sqrt{2}} Y_{1,1} + \frac{\varepsilon_x + i\varepsilon_y}{\sqrt{2}} Y_{1,-1})},$$

Where for Right and Left circular polarization only the middle and last term survive, respectively (PS: the term of right and left polarization used here is an expression convenience, to be more accurate and universal, the polarization should be described by using the helicity of +1 and –1). In order to calculate the matrix element in 2.1, it is reasonable to express the initial state $|jm\rangle$ as superposition of $Y_{l,l_z}^{s_z}$ states and to

integrate over the spherical coordinates r,θ,φ. For left circular polarization(LCP) light $x+iy=r\sin\theta\ e^{i\varphi}$ for left polarization, the integral $\int e^{i(m-m'-1)\varphi}d\varphi$ is non vanishing only if $m=m'+1$ and for the right circular polarization(RCP) light, only if $m=m'-1$:

Final state *Initial state*

For left polarization light:

$$Y_{2,2}^{\downarrow *}=(\sqrt{\frac{5}{4\pi 4!}}P_2^2(\cos\theta)e^{i2\varphi})^*=\sqrt{\frac{5}{4\pi}}\ \sqrt{\frac{1}{24}}P_2^2 \qquad Y_{1,1}=\sqrt{\frac{3}{4\pi 2!}}P_1^1(\cos\theta)e^{i\varphi}=\sqrt{\frac{3}{4\pi}}\ \sqrt{\frac{1}{2}}P_1^1$$

$$Y_{2,1}=\sqrt{\frac{5}{4\pi 3!}}P_2^1(\cos\theta)e^{i2\varphi}=\sqrt{\frac{5}{4\pi}}\ \sqrt{\frac{1}{6}}P_2^1 \qquad Y_{1,0}=\sqrt{\frac{3}{4\pi}}P_1^0(\cos\theta)e^{i\varphi}=\sqrt{\frac{3}{4\pi}}\ P_1^0$$

$$Y_{2,0}=\sqrt{\frac{5}{4\pi}}P_2^0(\cos\theta)e^{i2\varphi}=\sqrt{\frac{5}{4\pi}}\ P_2^0 \qquad Y_{1,-1}=\sqrt{\frac{3\cdot 2!}{4\pi}}P_1^{-1}(\cos\theta)e^{i\varphi}=\sqrt{\frac{3}{4\pi}}\ \sqrt{2}P_1^{-1}$$

for right polarization light:

$$Y_{2,0}=\sqrt{\frac{5}{4\pi}}P_2^0(\cos\theta)e^{i2\varphi}=\sqrt{\frac{5}{4\pi}}\ P_2^0 \qquad Y_{1,1}=\sqrt{\frac{3}{4\pi 2!}}P_1^1(\cos\theta)e^{i\varphi}=\sqrt{\frac{3}{4\pi}}\ \sqrt{\frac{1}{2}}P_1^1$$

$$Y_{2,-1}=\sqrt{\frac{5}{4\pi}\cdot 3!}P_2^0(\cos\theta)e^{i2\varphi}=\sqrt{\frac{5}{4\pi}}\ \sqrt{6}\ P_2^0 \qquad Y_{1,0}=\sqrt{\frac{3}{4\pi}}P_1^0(\cos\theta)e^{i\varphi}=\sqrt{\frac{3}{4\pi}}\ P_1^0$$

$$Y_{2,-2}=\sqrt{\frac{5}{4\pi}\cdot 4!}P_2^0(\cos\theta)e^{i2\varphi}=\sqrt{\frac{5}{4\pi}}\ \sqrt{24}\ P_2^0 \qquad Y_{1,-1}=\sqrt{\frac{3\cdot 2!}{4\pi}}P_1^{-1}(\cos\theta)e^{i\varphi}=\sqrt{\frac{3}{4\pi}}\ \sqrt{2}P_1^{-1}$$

with recursion formula:

$\sin\theta P_l^m=\frac{1}{2l+1}(P_{l+1}^{m+1}-P_{l-1}^{m+1})$ and $\sin\theta P_l^m=\frac{1}{2l+1}\{(l+m)(l+m-1)P_{l-1}^{m-1}-(l-m+1)(l-m+2)P_{l+1}^{m-1}\}$,

we can obtain:

$\sin\theta P_1^1=\frac{1}{3}\{P_2^2-P_0^2\}=\frac{1}{3}\{2P_0^0-2P_2^0\}$; $\sin\theta P_1^0=\frac{1}{3}\{P_2^1-P_0^1\}=\frac{1}{3}\{-6P_2^{-1}\}$;

$\sin\theta P_1^{-1}=\frac{1}{3}\{P_2^0-P_0^0\}=\ \frac{1}{3}\{-12P_2^{-2}\}$

with formula $P_l^m P_l^m=\frac{(l+m)!}{(l-m)!}\frac{2}{2l+1}$ and $P_l^m P_{l'}^m=0$ if $l\neq l'$ we have:

$P_2^2P_2^2=4!\times\frac{2}{5}$ $P_2^1P_2^1=3!\times\frac{2}{5}$ $P_2^0P_2^0=\frac{2}{5}$ $P_2^{-1}P_2^{-1}=\frac{1}{3!}\times\frac{2}{5}$ $P_2^{-2}P_2^{-2}=\frac{1}{4!}\times\frac{2}{5}$

Setting R as the radial wave function.

LCP

$$|R\iint \sin\theta d\theta d\varphi Y_{2,2}^{\downarrow *}(\theta,\varphi)\sin\theta Y_{1,1}^{\downarrow}(\theta,\varphi)|^2 = A|\sqrt{12}|^2 R^2 = 2/5\ R^2.$$

$$|R\iint \sin\theta d\theta d\varphi Y_{2,1}^{\downarrow *}(\theta,\varphi)\sin\theta Y_{1,0}^{\downarrow}(\theta,\varphi)|^2 = A|\sqrt{6}|^2 R^2 = 1/5\ R^2$$

$$|R\iint \sin\theta d\theta d\varphi Y_{2,0}^{\downarrow *}(\theta,\varphi)\sin\theta Y_{1,-1}^{\downarrow}(\theta,\varphi)|^2 = A|\sqrt{2}|^2 R^2 = 1/15\ R^2$$

RCP

$$|R\iint \sin\theta d\theta d\varphi Y_{2,0}^{\downarrow *}(\theta,\varphi)\sin\theta Y_{1,1}^{\downarrow}(\theta,\varphi)|^2 = A|\sqrt{2}|^2 R^2 = 1/15\ R^2$$

$$|R\iint \sin\theta d\theta d\varphi Y_{2,-1}^{\downarrow *}(\theta,\varphi)\sin\theta Y_{1,0}^{\downarrow}(\theta,\varphi)|^2 = A|\sqrt{6}|^2 R^2 = 1/5\ R^2$$

$$|R\iint \sin\theta d\theta d\varphi Y_{2,-2}^{\downarrow *}(\theta,\varphi)\sin\theta Y_{1,-1}^{\downarrow}(\theta,\varphi)|^2 = A|\sqrt{12}|^2 R^2 = 2/5\ R^2$$

For L_2 edge under LCP

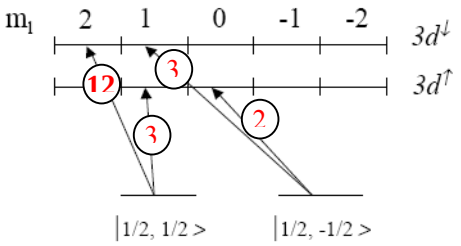

$|l,s,J,m_j\rangle$	$|l,m_l,s,m_s\rangle$ basis
$|\frac{1}{2},\frac{1}{2}\rangle$	$-\frac{1}{\sqrt{3}}Y_{10}^{\uparrow}+\frac{\sqrt{2}}{\sqrt{3}}Y_{11}^{\downarrow}$
$|\frac{1}{2},-\frac{1}{2}\rangle$	$-\frac{\sqrt{2}}{\sqrt{3}}Y_{1,-1}^{\uparrow}+\frac{1}{\sqrt{3}}Y_{10}^{\downarrow}$

The intensity of transition to up spin is

$$I^{\uparrow} = \sum_{i,f}|\langle f|e\cdot r|i\rangle|^2 = \{\frac{1}{3}|\langle Y_{2,1}|e\cdot r|Y_{1,0}\rangle|^2 + \frac{2}{3}|\langle Y_{2,0}|e\cdot r|Y_{1,-1}\rangle|^2\}R^2$$

$$= \{1/3 * 1/5 \quad +2/3*1/15\}R^2 = \{3/45 +2/45\}R^2 = 1/9\ R^2$$

$$I^{\downarrow} = \sum_{i,f}|\langle f|e\cdot r|i\rangle|^2 = \{\frac{2}{3}|\langle Y_{2,2}|e\cdot r|Y_{1,1}\rangle|^2 + \frac{1}{3}|\langle Y_{2,1}|e\cdot r|Y_{1,0}\rangle|^2\}R^2$$

$$=\{2/3*2/5+1/3*1/5\}\ R^2 = \{12/45+3/45\}\ R^2 1/3\ R^2$$

LCP : $I^{\uparrow}/(I^{\uparrow}+I^{\downarrow}) = \mathbf{0.25}$ $I^{\downarrow}/(I^{\uparrow}+I^{\downarrow}) = \mathbf{0.75}$

For RCP at the L_2 edge, the intensity of transition to up spin is

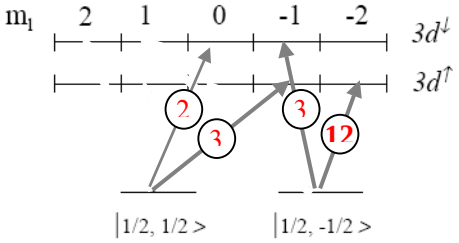

$|l,s,J,m_j\rangle$	$|l,m_l,s,m_s\rangle$ basis
$\left\|\frac{1}{2},\frac{1}{2}\right\rangle$	$-\frac{1}{\sqrt{3}}Y^{\uparrow}_{1,0}+\frac{\sqrt{2}}{\sqrt{3}}Y^{\downarrow}_{1,1}$
$\left\|\frac{1}{2},-\frac{1}{2}\right\rangle$	$-\frac{\sqrt{2}}{\sqrt{3}}Y^{\uparrow}_{1,-1}+\frac{1}{\sqrt{3}}Y^{\downarrow}_{1,0}$

$$I^{\uparrow}=\sum_{i,f}|\langle f|e\cdot r|i\rangle|^2=\{\frac{1}{3}|\langle Y_{2,-1}|e\cdot r|Y_{1,0}\rangle|^2+\frac{2}{3}|\langle Y_{2,-2}|e\cdot r|Y_{1,-1}\rangle|^2\}R^2$$

$$=\{1/3 * 1/5\ R^2+2/3*2/5\}R^2=\{3/45+12/45\}R^2=1/3\ R^2$$

$$I^{\downarrow}=\sum_{i,f}|\langle f|e\cdot r|i\rangle|^2=\{\frac{2}{3}|\langle Y_{2,0}|e\cdot r|Y_{1,1}\rangle|^2+\frac{1}{3}|\langle Y_{2,-1}|e\cdot r|Y_{1,0}\rangle|^2\}R^2$$

$$=\{2/3*1/15+1/3*1/5\}\ R^2=\{2/45+3/45\}\ R^2=1/9\ R^2$$

RCP : $I^{\uparrow}/(I^{\uparrow}+I^{\downarrow})=\mathbf{0.75}$ $I^{\downarrow}/(I^{\uparrow}+I^{\downarrow})=\mathbf{0.25}$

For L_3 edge:

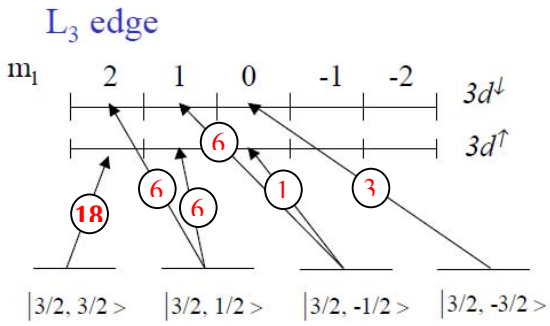

$\left\|\frac{3}{2},\frac{3}{2}\right\rangle$	$Y^{\downarrow}_{1,1}$
$\left\|\frac{3}{2},\frac{1}{2}\right\rangle$	$\frac{\sqrt{2}}{\sqrt{3}}Y^{\uparrow}_{1,0}+\frac{1}{\sqrt{3}}Y^{\downarrow}_{1,1}$
$\left\|\frac{3}{2},-\frac{1}{2}\right\rangle$	$\frac{1}{\sqrt{3}}Y^{\uparrow}_{1,-1}+\frac{\sqrt{2}}{\sqrt{3}}Y^{\downarrow}_{1,0}$
$\left\|\frac{3}{2},-\frac{3}{2}\right\rangle$	$Y^{\downarrow}_{1,-1}$

For LCP:

$$I^{\uparrow}=\sum_{i,f}|\langle f|e\cdot r|i\rangle|^2=\{|\langle Y_{2,2}|e\cdot r|Y_{1,1}\rangle|^2+\frac{2}{3}|\langle Y_{2,1}|e\cdot r|Y_{1,0}\rangle|^2+\frac{1}{3}|\langle Y_{2,0}|e\cdot r|Y_{1,-1}\rangle|^2\}R^2$$

$$=\{2/5+2/3*1/5+1/3*1/15\}R^2=\{18/45+6/45+1/45\}\ R^2=5/9\ R^2$$

$$I^{\downarrow}=\sum_{i,f}|\langle f|e\cdot r|i\rangle|^2=\{\frac{1}{3}|\langle Y_{2,2}|e\cdot r|Y_{1,1}\rangle|^2+\frac{2}{3}|\langle Y_{2,1}|e\cdot r|Y_{1,0}\rangle|^2+|\langle Y_{2,0}|e\cdot r|Y_{1,-1}\rangle|^2\}R^2$$

$= \{1/3*2/5 + 2/3*1/5 + 1/15\}R^2 = \{6/45 + 6/45 + 3/45\}\ R^2 = 1/3\ R^2$

LCP(μ^+): $I^{\uparrow}/(I^{\uparrow}+I^{\downarrow}) = \mathbf{0.625}$ $I^{\downarrow}/(I^{\uparrow}+I^{\downarrow}) = \mathbf{0.375}$

For Ni, Co strong magnet, there is only d↓

For RCP:

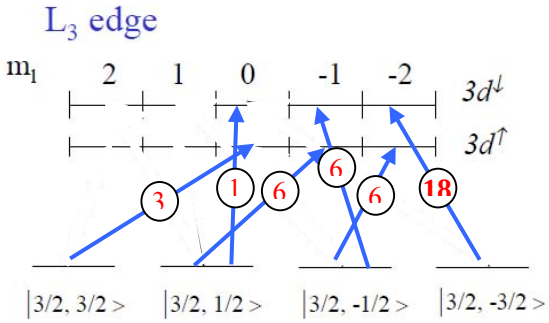

$|\frac{3}{2},\frac{3}{2}\rangle \quad Y^{\uparrow}_{1,1}$

$|\frac{3}{2},\frac{1}{2}\rangle \quad \frac{\sqrt{2}}{\sqrt{3}}Y^{\uparrow}_{1,0}+\frac{1}{\sqrt{3}}Y^{\downarrow}_{1,1}$

$|\frac{3}{2},-\frac{1}{2}\rangle \quad \frac{1}{\sqrt{3}}Y^{\uparrow}_{1,-1}+\frac{\sqrt{2}}{\sqrt{3}}Y^{\downarrow}_{1,0}$

$|\frac{3}{2},-\frac{3}{2}\rangle \quad Y^{\downarrow}_{1,-1}$

$$I^{\uparrow} = \sum_{i,f} |\langle f | e\cdot r | i\rangle|^2 = \{|\langle Y_{2,0} | e\cdot r | Y_{1,1}\rangle|^2 + \frac{2}{3}|\langle Y_{2,-1} | e\cdot r | Y_{1,0}\rangle|^2 + \frac{1}{3}|\langle Y_{2,-2} | e\cdot r | Y_{1,-1}\rangle|^2\}R^2$$

$= \{1/15 + 2/3*1/5 + 1/3*2/5\}R^2 = \{3/45 + 6/45 + 6/45\}R^2 = 1/3\ R^2$

$$I^{\downarrow} = \sum_{i,f} |\langle f | e\cdot r | i\rangle|^2 = \{\frac{1}{3}|\langle Y_{2,0} | e\cdot r | Y_{1,1}\rangle|^2 + \frac{2}{3}|\langle Y_{2,-1} | e\cdot r | Y_{1,0}\rangle|^2 + |\langle Y_{2,-2} | e\cdot r | Y_{1,-1}\rangle|^2\}R^2$$

$= \{1/3*1/15 + 2/3*1/5 + 2/5\}R^2 = \{1/45 + 6/45 + 18/45\}R^2 = 5/9\ R^2$

RCP (μ^-): $I^{\uparrow}/(I^{\uparrow}+I^{\downarrow}) = \mathbf{0.375}$ $I^{\downarrow}/(I^{\uparrow}+I^{\downarrow}) = \mathbf{0.625}$

For Ni, Co strong magnet, there is only empty d↓

L_2 total $(\mu^+ + \mu^-) \propto (1/3+1/9)R^2 = 4/9\ R^2$

L_3 total $(\mu^+ + \mu^-) \propto (1/3+5/9)R^2 = 8/9\ R^2$

Branchin ration $L_3 : L_2 = 2 : 1$

L_2 XMCD $(\mu^+ - \mu^-) \propto (1/3-1/9)R^2 = 4/9\ R^2$

L_3 XMCD $(\mu^+ - \mu^-) \propto (1/3-5/9)R^2 = -4/9\ R^2$

Branchin ration $L_3 : L_2 = -1 : 1$

This result explains the larger intensity of the L_3 edge relative to the L_2 edge and the opposite sign of the dichroic contribution observed in the experiment spectra. However these calculated ratio values are usually not consistent with those derived from the measured XMCD spectra. In fact, considering the final *d* states as equally probable, the intensity ratio is determined only by the degeneracy of the initial states. In the model given above, we have only considered the exchange splitting effect at 3d shell. However, the symmetry between the final states is broken if valence-band spin-orbit coupling is included. The model based on both exchange splitting and spin –orbit interaction are given in following figure Here, again we assume the down spin band is completely occupied therefore the transition can be omitted here.

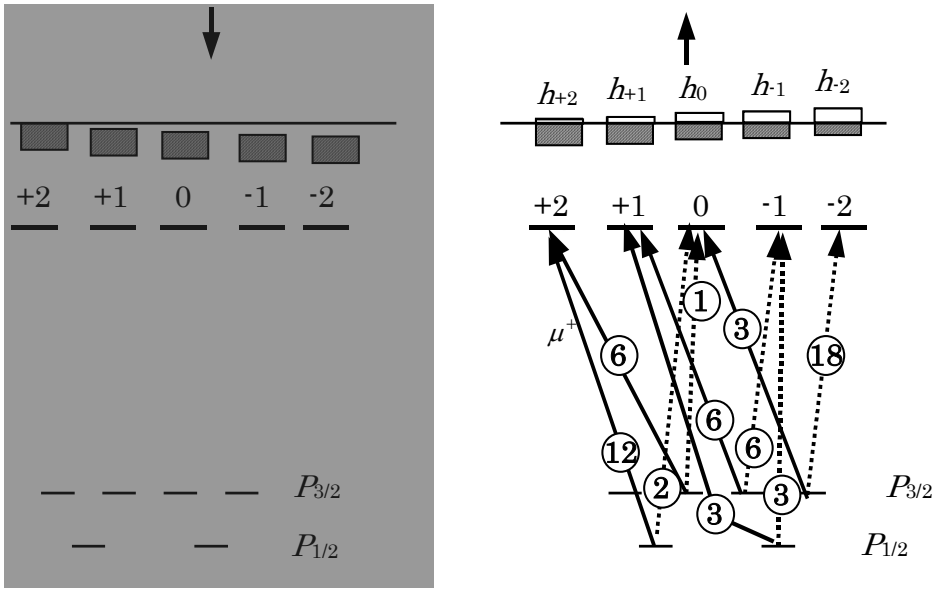

The hole number at each m_d states are expressed by h_{+2}, h_{+1},……, therefore we can obtain

$$\langle L_z \rangle = -(2h_{+2} + h_{+1} - h_{-1} - 2h_{-2})\hbar$$
$$\langle S_z \rangle = -(h_{+2} + h_{+1} + h_0 + h_{-1} + h_{-2})\frac{\hbar}{2} = \frac{n_h}{2}\hbar$$

Using the transition probability calculated in the above, the relative transition intenstity for L_3 and L_2 are given by:

$$L_3 : \Delta I_{L3} \propto 6h_{+2} + 6h_{+1} + 2h_0 - 6h_{-1} - 18h_{-2}$$
$$L_2 : \Delta I2 \propto 12h_{+2} + 3h_{+1} - 2h_0 - 3h_{-1}$$

and $\Delta I_{L3} + \Delta I_{L2} \propto 9(2h_{+2} + h_{+1} - h_{-1} - 2h_{-2}) \propto -9\langle L_z \rangle$

Therefore, if the SO interaction is ignored, then the hole number at all 3d states are equal and the XMCD of L_3 and L_2 will be proportional to $\langle S_z \rangle$. Meanwhile the summation of XMCD intenstity over L_3 and L_2 will be zero. These are exactly same with the one we worked out from the calculation where the ratio for XMCD at L_3 and L_2 are –1:1. Thus the asymmetry of $\Delta I_{L3} + \Delta I_{L2}$ can be used as an indicator to describe the value of $\langle L_z \rangle$. By referring the results calculated the references [1-3], the sum rule can be given as follow.

Sum rules of XMCD

Sum rules relate dichroism and total absorption to the ground-state orbital and spin magnetic moment of the probed element and shell.

The orbital moment sum rule can be expressed as follows:

$$\langle L_z \rangle = \frac{2l(l+1)(4l+2-n)}{l(l+1)+2-c(c(c-1)} \bullet \frac{\int_{j^+ + j^-} (\mu^+ - \mu^-) dw}{\int_{j^+ + j^-} (\mu^+ + \mu^- + \mu^0) dw}$$

where

l = orbital quantum number of the valence state,

c =orbtital quantum number of the core state,

n = number of electrons in the valence state

$\mu^+(\mu^-)$ = absorption spectrum for the left(right) circularly polarized light.

μ^0 = absorption spectrum for linearly polarized light,..

$j^+(j^-)$ = (l +1/2).(l -1/2) (ex. $2P_{1/2}$, $2P_{3/2}$)

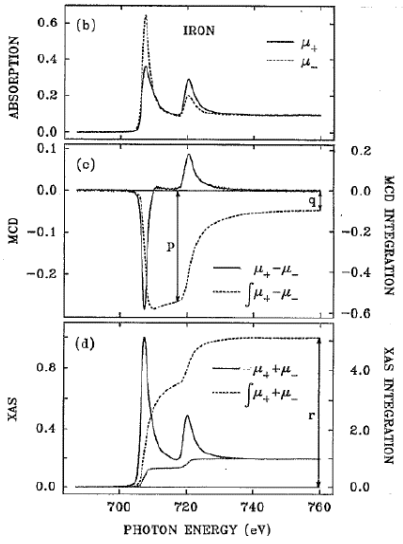

For $L_{2,3}$-edge c=1*(2p)*, l=2*(d)*

$$\langle L_z \rangle = 2n_h \cdot \frac{(\Delta L_3 + \Delta L_2)}{\int_{L3+L2} (\mu^+ + \mu^- + \mu^0) dw}$$

$$= \langle L_z \rangle = 2n_h \cdot \frac{(\Delta L_3 + \Delta L_2)}{3/2(I_{L3} + I_{L2})}$$

$m_{orb} = -\mu_B L / \hbar$ and $L = \langle L_z \rangle \hbar$

$$m_{orb} = -\frac{4}{3} n_h [\frac{(\Delta L_3 + \Delta L_2)}{(I_{L3} + I_{L2})}] \mu_B$$

Adding the circular polarization factor and the angle θ between the wave vector k and magnetization M.

The accurate value of orbital momentum is given by

$$m_{orb} = -\frac{4n_h}{3P_c \cos\theta} [\frac{(\Delta L_3 + \Delta L_2)}{(I_{L3} + I_{L2})}] \mu_B$$

Similarly, the spin moment sum rule can be written:

$$\langle S_z \rangle + c_2(n) \langle T_z \rangle = c_1(n) \frac{[\int_{j^+} dw(\mu^+ - \mu^-) - [(c+1)/c] \int_{j^-} dw(\mu^+ - \mu^-)]}{[\int_{j^+ + j^-} (\mu^+ + \mu^- + \mu^0) dw]}$$

here, $c_1(n) = 3c(4l + 2 - n) / [l(l+1) - 2 - c(c+1)]$

$$c_2(n) = \{l(l+1)[l(l+1) + 2c(c+1) + 4] - 3(c-1)^2 (c+2)^2\} / 6lc(l+1)(4l + 2 - n)$$

$\langle T_z \rangle$ =expectation value of magnetic dipole operator

$$T = S - r(r \cdot s)/r^2$$

For For $L_{2,3}$-edge c=1*(2p)*, l=2*(d)*

$$\langle S_z \rangle + (7/2) \langle T_z \rangle = (3/2) n_h [(\Delta L_3 - 2\Delta L_2) / \int_{L3+L2} dw((\mu^+ + \mu^- + \mu^0)] = n_h \frac{[(\Delta L_3 - 2\Delta L_2)}{I_{L3} + I_{L2}}$$

with the relation: S=$\langle S_z \rangle \hbar$ and $m_{spin} = -2\mu_B S / h$ therefore, m_{spin} can be given by

$$m_{spin} \text{-}7\langle T_z\rangle = \text{-}2\frac{n_h}{P_c\cos\theta}\frac{[(\Delta L_3 - 2\Delta L_2)}{I_{L3}+I_{L2}}\mu_B$$

$\langle T_z\rangle$ can be determined by two ways:

① Stöhr et al has found: $\langle T_x\rangle + \langle T_y\rangle + \langle T_z\rangle = 0$ when measurement along three perpendicular directions(with saturation field) allow to eliminate $\langle T_z\rangle$ and obtain m_{spin}. And in most of polycrystalline sample, $\langle T\rangle$ is already averaged over different angles. So $\langle T_z\rangle$ can be neglected.

② $\cos(54.7^0)(\ \langle T_x\rangle + \langle T_y\rangle + \langle T_z\rangle\ )=0$ because $3\cos 54.7^0\text{-}1=0$; therefore measurement along magic angle 54.7^0 also allows to cancel $\langle T_z\rangle$ and absolute value of m_{spin} is thus obtained.

Experiment setup:

The XMCD experiment setup is schematically shown in Fig.1. The XMCD spectra are taken at the bending-magnet station Beamline 4B at UVSOR-II, Institute for Molecular Science (IMS), Okazaki, Japan. Circularly polarized X-rays are obtained by using the upper (0.4±0.1 mrad, positive helicity) or lower (–0.4±0.1 mrad, negative helicity) part from the synchrotron orbit plane. The circular polarization factor P_c is estimated to be 0.70 from the storage ring and beamline parameters, and is in good agreement with the evaluation from the reference spectra of thick Co films. The energy

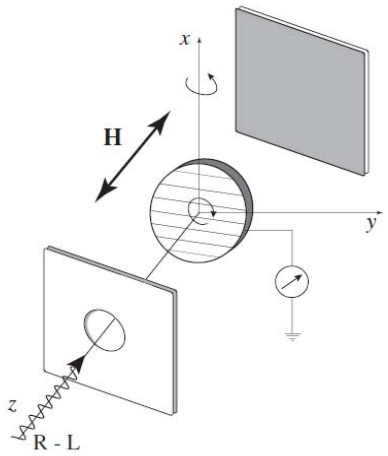

Fig.1 Schematic setup of the XMCD

resolution is $\Delta E/E$~10^{-3} around ~700 eV. The sample is mounted in the

temperature-variable manipulator which can be rotated over 180° (Fig.1). By rotating the sample, the incident angles of X-rays are set at 0° for normal X-ray incidence and at 60° for grazing X-ray incidence. During the XMCD measurements, a magnetic field is applied to saturate the sample magnetization along the easy axis, and the XMCD spectra were recorded with the reversal of the magnetic field as well as the helicity of X-rays. We take all the XAS by monitoring the total electron yield, and simultaneously we measure the intensity of the incident X-rays (I_0) with an Au-coated *W* mesh placed in front of the sample which serves as a measure of the incident photon flux.

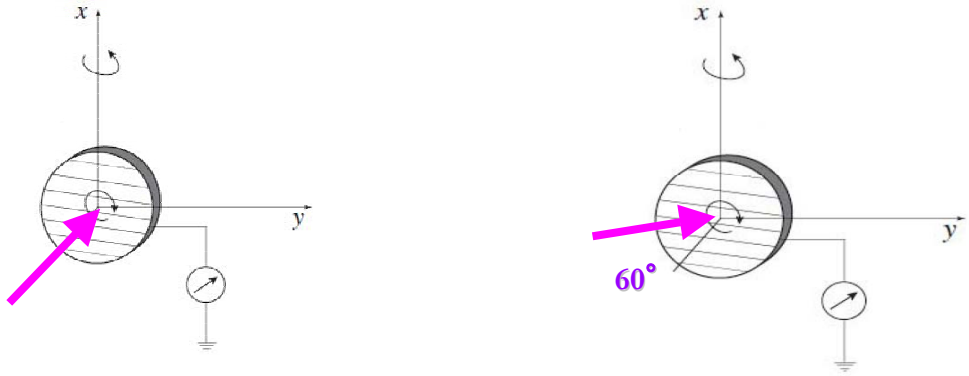

Normal incidence
Perpendicular magnetization

Grazing incidence
In plane magnetization

Appendix: The calibration of the polarization parameter:

The circularly polarized light is generated at the BL4B in UVSOR, where the grazing-incidence varied-line spacing grating monochromator is installed. The beamline optics is given in the picture below. An aperture is placed in the upstream to obtain circularly polarized X rays as well as linearly polarized X rays. The left side of the picture shows the calculated Stokes S3 parameter for BL4B [4], and the X rays with circularly polarization factor of 0.70 available with a reasonable intensity. Since the electrons in the UVSOR storage ring rotates in counterclockwise, the upper part of the synchrotron radiation gives positive helicity (negative S3) while the lower part

yields negative helicity (positive S3).

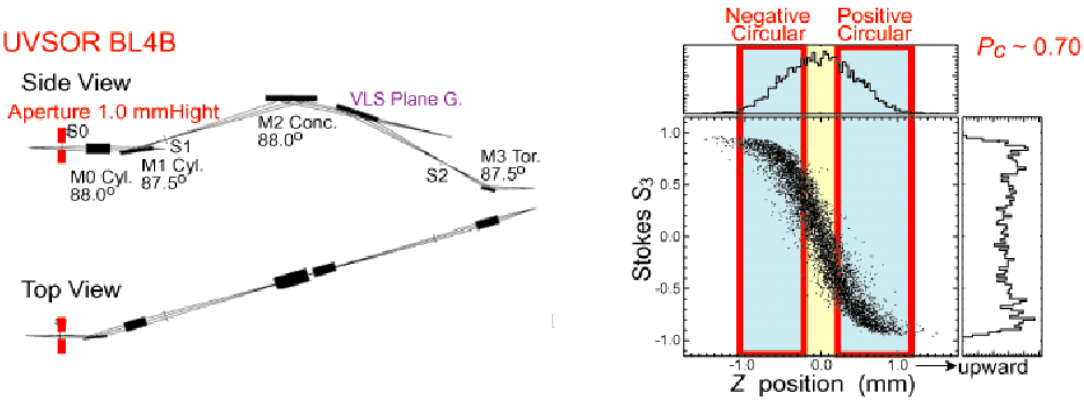

Reference:

1 G. van der Laan *et al.*, Phys. Rev. B. **34**, 6529 (1986).

2 B.T.Thole et al. Phys.Rev.Lett 68,1943 (1992)

3 M. Altarelli et al. Phys.Rev.B 47, 597 (1993)

4 C.T.Chen et al. Phys.Rev.Lett 75,152 (1995)

5 T Gejo et al Chemical *Physics*, *289*, P*15, 2003*,

2.2 Surface magneto optical Kerr effect (SMOKE)

Michael Faraday discovered the first magneto-optic effect (MOE) in 1845. Magnetic Kerr effect was found by John Kerr in 1877, thirty-two years later, while he was examining the polarization of light reflected from a polished electromagnet pole. The application of the Kerr effect to study surface magnetism was introduced by Moog and Bader in 1985 along with the acronym SMOKE to denote the surface magneto-optic Kerr effect. The first system studied was ultrathin Fe films grown epitaxially onto a Au(1 0 0) single crystal [1,2]. Magnetic hysteresis loops were obtained with monolayer sensitivity. Since then SMOKE has emerged as a indispensable surface magnetism technique which can be found in many laboratories worldwide. The broad acceptance of the SMOKE technique is due to its simplicity and its ability to generate the 'universal currency' in magnetism–the hysteresis loop. SMOKE has thus been applied successfully to address various contemporary issues in low-dimensional magnetism [3].

Principle of SMOKE:

Plane polarized light can be viewed as being made up of the superposition of two circular components, *Left* and *Right*-circularly polarized light. In the view of classical motion of electrons, as a beam of light propagates through a medium, the electrical field of the light generates the motions of the electrons in the medium. Without presence of external magnetic field, it is obvious that a left-circularly polarized electric field will drive the electrons into left circular motion, and a right-circularly polarized electric field will drive the electrons into right circular motion. The radius of the electron orbit for left and right circular motion will be the same. After an external magnetic field is applied in the propagation direction of the electromagnetic wave, there will be an additional Lorentz force acting on each electron. This force points toward or away from the circle's center for left or right circular motion. Thus, the radius for left circular

motion will be reduced and the radius for right circular motion will expand. The difference in the radii of the left- and right-circularly polarized modes will give different dielectric constants correspondingly. Thus, it is the Lorentz force of the external magnetic field that generates magneto-optic effect.

In theory, for *L* and *R*-circularly polarized light, the magnetic medium has different refractive indices for these two polarized modes. Therefore the two circular modes travel with different velocities and attenuate differently in the material. Upon reflection from the material, the two modes recombine to produce the Kerr rotation and ellipticity. The macroscopic description of Kerr effects relies on the two modes having different refractive indices within the material. The general form of the dielectric tensor which represents the effects of a magnetic medium is given as[5]:

$$\varepsilon = \varepsilon_0 \begin{pmatrix} 1 & -iQ_z & iQ_y \\ iQ_z & 1 & -iQ_x \\ -iQ_y & iQ_x & 1 \end{pmatrix}$$

The two normal modes are left-circularly polarized light with refraction index $n_L = n(1 - \frac{1}{2} Q \cdot k)$ and right-circularly polarized light with refraction index $n_R = n(1 + \frac{1}{2} Q \cdot k)$. Where $n = \sqrt{\varepsilon}$ and $Q_{x,y,z}$ is the Voigt magneto optic constant which describes the magneto optical effect and k is the unit vector along the direction of the light propagation.. This Voigt term is to the first order proportional to the magnetization of the material. It is this complex Voigt term (the off diagonal terms) which generally modifies the polarization.

There are principally three Kerr effects which are classified depending upon the magneto optic geometry being employed. These are shown in Fig.1. The effects are dependent on the orientation of the magnetization with respect to the incident and sample planes. In the longitudinal Kerr effect, the magnetization is in the plane of the sample and

parallel to the incident plane. In the transverse Kerr effect, the magnetization is also in the plane of the sample, but is perpendicular to the incident plane. In the polar Kerr effect,

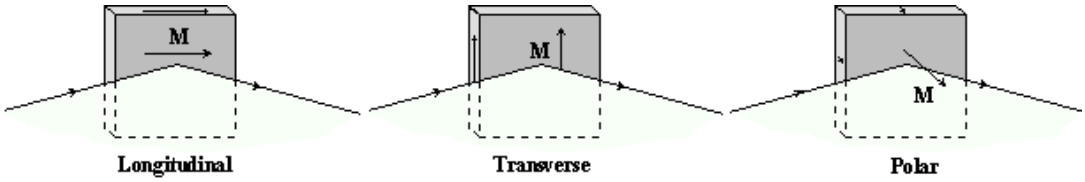

Fig.1 Three conventional Kerr experiment setups.

the magnetization is perpendicular to the sample plane and is parallel to the plane of incidence. Consideration of these three magneto optic geometries simplifies the understanding of the Kerr effect. The longitudinal and transverse Kerr effects are generally used to study the in-plane magnetic anisotropy, whereas the polar configuration is used to study thin films, which exhibit perpendicular anisotropy. Upon reflection the longitudinal and polar Kerr effects, generally, alter the polarization of the incident light from plane to elliptically polarize with the major axis rotated (Kerr rotation). In the transverse effect there is no change in the polarization of the incident light. This is more clearly illustrated in Figure 2, where a vector representation using the idea of a Lorentz force indicates how p and s-polarized light interact in the three magneto optic geometries. The electric field of the plane-polarised light which is incident upon the material can be thought of as exciting the electrons so that they oscillate parallel to the incident polarization. This gives rise to the normal component (E_N) of light in the reflected light. The additional Kerr component, E_K, arises because of the Lorentz force. The Lorentz force induces a small component which is perpendicular to both the primary motion (normal component) and the direction of the magnetization. Generally, the two components are not in-phase and it is the superposition of these two components which gives rise to a magnetization dependent rotation of the polarization. In the longitudinal and polar Kerr effects (Fig. 2 a,b), p or s-polarized light will generally become elliptically

polarized with its major axis rotated (Kerr rotation). This is a consequence of an

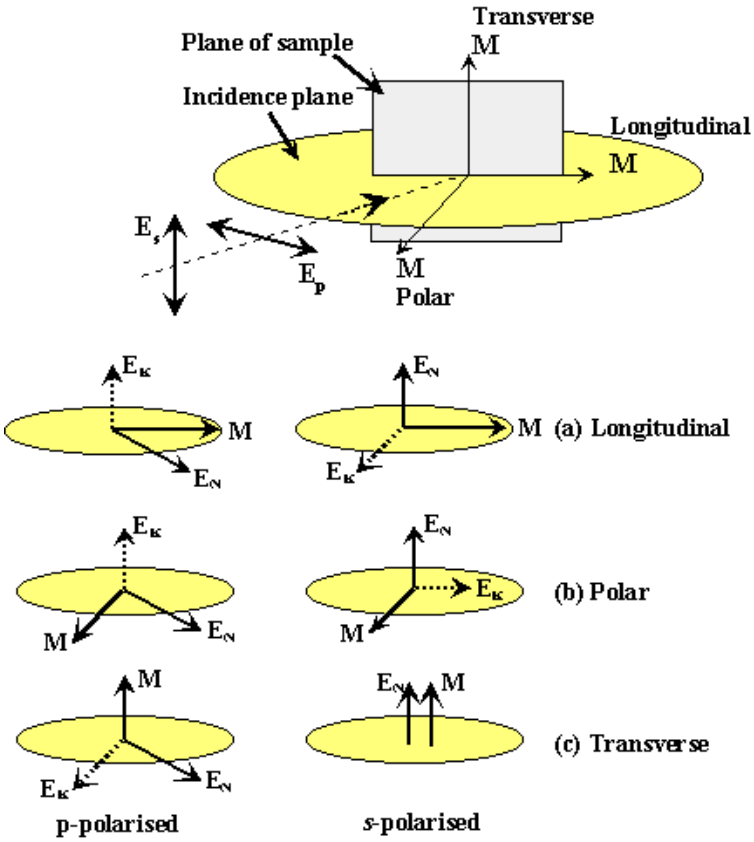

Fig.2. The interplay between polarized light, magnetization in terms of Lorentz force

orthogonal electric field component being induced because of the Lorenz force. The directions of the Lorentz force, and therefore the induced components, are shown by the dashed arrows ($\mathbf{E_K}$). The Kerr effect diminishes as the angle of incident approaches the normal to the sample plane in the longitudinal effect because either the Lorentz force vanishes (*p*-polarized) or points along the direction of the light (*s*-polarized). This is not the case for the polar Kerr effect because the magnetization is out of the sample plane and a Lorentz force always exists at normal incidence. The polar effect is independent of the incident polarisation at normal incidence. The angle of incidence usually tends to vary in the range 5-60^0 depending on the experimental arrangement for the longitudinal and transverse modes. The transverse effect involves no change in polarisation, since there is either no Lorentz force present (*s*-polarised) or the induced component (*p*-polarised) has the same polarisation as the incident polarisation (Fig.2 c).

In the ultrathin film system, the polar Kerr effect is usually an order of magnitude larger than the longitudinal Kerr effect. This can be understood as follows [3]:

$$\phi^{Pol} = -(\frac{4\pi}{\lambda})(\frac{N^2}{1-N_{sub}^2})Qd \quad \text{and} \quad \phi^{Lon} = (\frac{4\pi}{\lambda})(\frac{N_{sub}}{1-N_{sub}^2})\theta Qd$$

where:

N is the refractive index

Q is themagneto-optic (Voigt) constant of the medium.

d is the thickness

θ is the angle of incidence measured from the surface normal, is assumed small.

Therefore, $\phi^{Pol} >> \phi^{Lon}$ because of the extra N factor and the lack of θ factor in ϕ^{Pol}.

Experiment set up

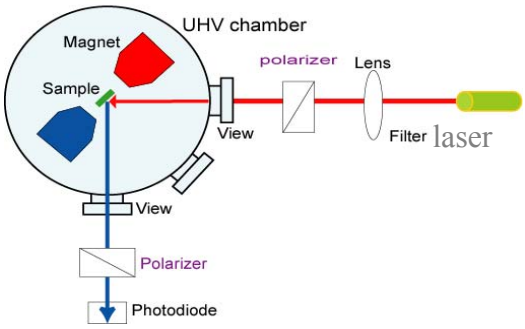

Longitudinal Kerr

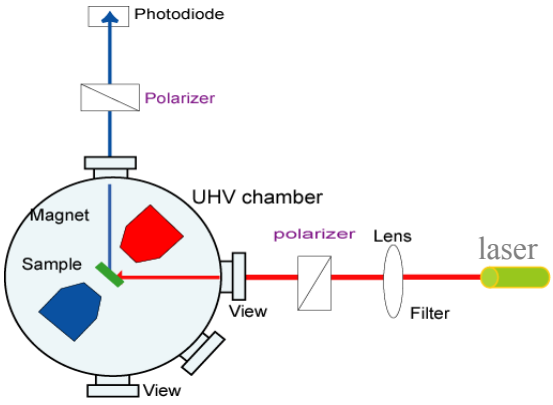

Polar Kerr

The above are the SMOKE experiment set-ups used in this work. The measurment is performed using a diode laser (635 nm)with an available magnetic field of 2500 G. The laser is focused onto the sample ($\varphi \sim 0.2mm$) with the incident angle of 45° for both longitudinal and polar configuration. The two measuring modes are realized by rotating sample 90° with respect to the surface normal. Kerr intensity, measured by the photodiode

after the light has passed through an analyzing polarizer that is set at an angle δ from extinction, is [4]:

$$I = | E_p \sin\delta + E_s \cos\delta |^2 \approx | E_p \delta + E_s |^2$$

since $E_s / E_p = \phi' + i\phi''$ ϕ' is the kerr rotation and ϕ'' is the ellipticity.

$$I = | E_p |^2 | \delta + \phi' + i\phi'' |^2 \approx | E_p |^2 (\delta^2 + 2\delta\phi') = I_0 (1 + \frac{2\phi'}{\delta})$$

with $I_0 = | E_p |^2 \delta^2$

Therefore the light intensity passing through the analyzer is propotional to the Kerr rotation.

Referrence:

1 E.R. Moog, S.D. Bader, Superlattices Microstruct. 1 543 (1985).

2 S.D. Bader, E.R. Moog, P. GruK nberg, J. Magn. Magn. Mater. 53 L295 (1986).

3 S.D. Bader, J. Magn. Magn. Mater. 100, 440 (1991)

4 Z.Q. Qiu, S.D. Bader. J. Magn. Magn. Mater. 200, 664-678 (1999)

5 J. Zak, E.R. Moog et al, J. Appl. Phys. 68(8) 4203 (1990).

2.3 X ray absorption fine structure

X-rays are light with energies ranging from 500 eV to 500 keV, or wavelengths from 25Å to 0.25 Å. At this energy regime, light is absorbed by all matter through the *photo-electric effect*. In this process, an x-ray photon is absorbed by an electron in a tightly bound quantum core level (such as the 1s or 2p level) of an atom.In order for a particular electronic core level to participate in the absorption, the binding energy of this core level must be less than the energy of the incident x-ray. If the binding energy is *greater than* the energy of the x-ray, the bound electron will not be perturbed from the dell-defined quantum state and will not absorb the x-ray. If the binding energy of the electron is *less than* that of the x-ray, the electron may be removed from its quantum level. In this case, the x-ray is destroyed (i.e, absorbed) and any energy in excess of the electronic binding energy is given to a photo-electron that is ejected from the atom. This process has been well understood for nearly a century. The full implications of this process when applied to molecules, liquids, and solids will give rise to XAFS. When discussing x-ray absorption, we are primarily concerned with the *absorption coefficient*, μ which gives the probability that x-rays will be absorbed according to Beer's Law:

$$I = I_0 e^{-\mu t}$$

where I_0 is the x-ray intensity incident on a sample, t is the sample thickness, and I is the intensity transmitted through the sample. For x-rays, as for all light, the x-ray intensity is proportional to the number of x-ray photons. At most x-ray energies, the absorption coefficient μ is a smooth function of energy, with a value that depends on the sample density, the atomic number Z,

atomic mass A, and the x-ray energy E roughly as $\mu \approx \frac{\rho Z^4}{AE^3}$. The strong dependence of μ on both Z and E is a fundamental property of x-rays, and is the key to why x-ray absorption is useful for medical and other imaging techniques, including x-ray computed tomography. Due to the Z^4 dependence, the absorption coefficient for O, Ca, Fe, and Pb are very different – spanning several orders of magnitude – so that good contrast between different materials can be achieved for nearly any sample thickness and concentrations by adjusting the x-ray energy. When the incident x-ray has an energy equal to that of the binding energy of a core-level electron, there is a sharp rise in absorption: an *absorption edge* corresponding to the promotion of this core level to the continuum. For XAFS, we are concerned with the intensity of μ as a function of energy, near and at energies just above these absorption edges. An XAFS measurement is simply a measure of the energy dependence of μ at and above the binding energy of a known core level of a known atomic species. Since every atom has core-level electrons with well-defined binding energies, we can select the element to probe by tuning the x-ray energy to an appropriate absorption edge. These absorption edge energies are well-known (usually to within a tenth of percent), and tabulated.

XAFS theory:

A simple physical description of the XAFS process and the origin of the EXAFS equation will be given as follows. As described above, we start with the photoelectric effect shown in Fig.1left, in which an x-ray is absorbed by a core-level with binding energy, and a photo-electron with wave number k is created and propagates away from the atom. An important point for the discussion here is that the absorption due to a given core-level relies on there

being an *available state* for the photo-electron: a quantum state at exactly the right energy, and also the right angular momentum state. If there is no available state, there will be no absorption from that core level. For example, at energies below the 1s binding energy, a 1s electron could only be promoted to a *p* valence level below the binding energy (or Fermi level). Since all the

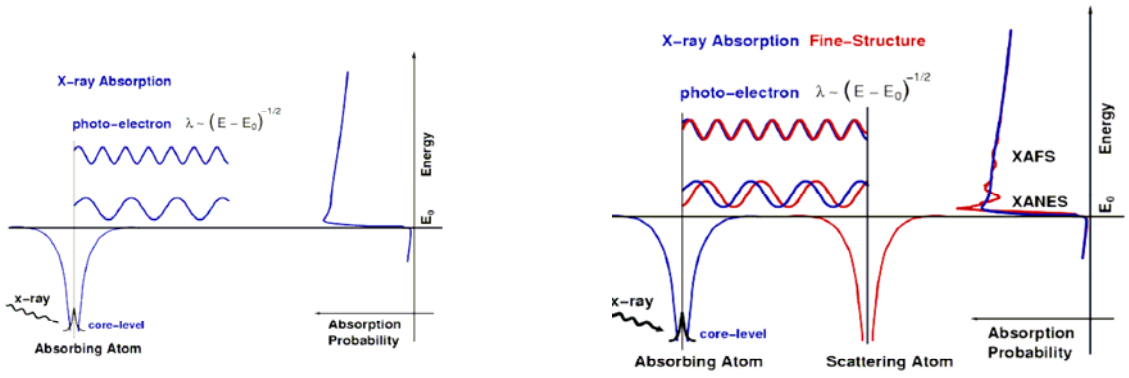

Fig.1 Schematic illustration of principle in X-ray absorption (left) and X-ray absorption fine-structure (right)

available valence levels are filled by the valence electrons, there is no state for the 1s electron to fill, and so there is no absorption from that core-level. When a neighboring atom is included in the picture (Fig.1 right), the photo-electron can scatter from the electrons of this neighboring atom, and the scattered photo-electron can return to the absorbing atom. Since the absorption coefficient depends on whether there is an available electronic state (that is whether there is an electron at the location of the atom and at the appropriate energy and momentum), the presence of the photo-electron scattered back from the neighboring atom will alter the absorption coefficient: This is the origin of XAFS. We'll now develop the XAFS equation using a slightly more formal description of this simple physical picture. Since x-ray absorption is a *transition* between two quantum states (from an initial state

with an x-ray, a core electron, and no photo-electron to a final state with no x-ray, a core hole, and a photo-electron), we describe μ(E) with Fermi's Golden Rule:

$$\mu \propto \sum \left| \langle \varphi_f | H' | \varphi_i \rangle \right|^2 \delta(E_f - E_i - \hbar\omega)$$

$$H' = -\frac{e}{mc} A(r) \cdot P$$

$$A(r) = \mathbf{e} A_0 e^{i\mathbf{k}_x \cdot \mathbf{r}}$$

$$\left| \langle \varphi_f | H' | \varphi_i \rangle \right| = \left| \langle \varphi_f | \mathbf{e} \cdot \mathbf{p} | \varphi_i \rangle \right| = im\omega \left| \langle \varphi_f | \mathbf{e} \cdot \mathbf{r} | \varphi_i \rangle \right|$$

$\mu \propto \sum \left| \langle \varphi_f | \mathrm{e} \cdot \mathrm{r} | \varphi_i \rangle \right|^2 \delta(E_f - E_i - \hbar\omega)$ By omitting the detaied derivation process we can finally obtain:

$$\chi(k) = \sum_j \frac{S_0^2 N_j f_j(k) e^{-2R_j/\lambda(k)} e^{-2k^2\sigma_j^2}}{kR_j^2} \sin[2kR_j + \delta_j(k)]$$

where $\chi(k) = \dfrac{\mu(E) - \mu(E_0)}{\mu(E_0)}$

$f(k)$: amplitude;

$\delta(k)$: phase shift

N: coordination number of neighboring atoms

R : distance to neighboring atoms

σ^2: mean-square disorder of neighbor atoms

Data Reduction: Strategy

Step for reducing measured data to μ(E) and then to $\chi(k)$

1. Convert measured intensities to μ(E)

2. Subtract a smooth pre-edge function, to get rid of any instrumental background, and absorption from other edges.

3. Normalize μ(E) to go from 0 to 1, so that it represents the absorption

of 1 x-ray.

4. Remove a smooth post-edge background function to approximate μ_0(E) to isolate the XAFS _.

5. Identify the threshold energy E_0, and convert from E to k space:

$$k = \sqrt{\frac{2m(E - E_0)}{\hbar^2}}$$

6. weight the XAFS $\chi(k)$ and Fourier transform from k to R space.

7. isolate the $\chi(k)$ for an individual "shell" by Fourier filtering.

XAFS modeling

$$\chi(k) = \sum_j \frac{S_0^2 N_j f_j(k) e^{-2R_j/\lambda(k)} e^{-2k^2\sigma_j^2}}{kR_j^2} \sin[2kR_j + \delta_j(k)]$$

These days, we can calculate $f(k)$ and $\delta(k)$ easily using the computer program FEFF.

XAFS experiment setup:

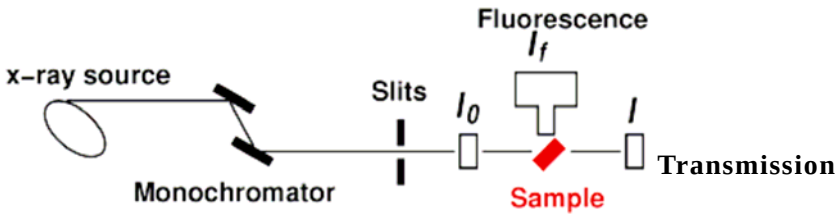

XAS measures the energy dependence of the X-ray absorption coefficient μ(E) at and above the absorption edge of a selected element. μ(E) can be measured in two ways:

Transmission: The absorption is measured directly by measuring what is transmitted trough the sample: $I = I_0 e^{-\mu(E)t}$ and $\mu(E)t = -\ln(I/I_0)$.

Fluorescence: The re-filling the deep core hole is detected, Typically the fluorescent x-ray is measured. $\mu(E) \propto I_f / I_0$.

Transverse magnetic anisotropy and staggered critical behavior of self-assembled Co nanorods grown on Cu(110)-(2 ✕3)N

Xiao Dong Ma, Takeshi Nakagawa, Fred M. Leibsle, and Toshihiko Yokoyama

(*Submitted*)

3.1 Introduction:

The understanding of the comprehensive magnetism in low dimension is extremely crucial for assembling of nanometer-sized structures with desired magnetic properties in future spintronics [1-8]. For two-dimensional systems, such as ultrathin epitaxial films and superlattices the novel magnetic properties such as ssurface magnetic anisotropy and spin reorientation, enhanced magnetic moment, increased curie temperature as well as unique critical behavior, has made it dramatically distinct from bulk materials. Research in magnetism is currently aiming at structures with much lower dimensionality**.** As generally known, with the further reduction in dimensionality of a physical system, magnetic ordering tends to decrease as fluctuations become relatively more pronunced. For instance, magnetic nanorod array with diameter of 30nm buried in a self-organized porous alumina nanohole template (Fig.1) shows easy axis along the rod indicating the shape anisotropy is the dominating [1].

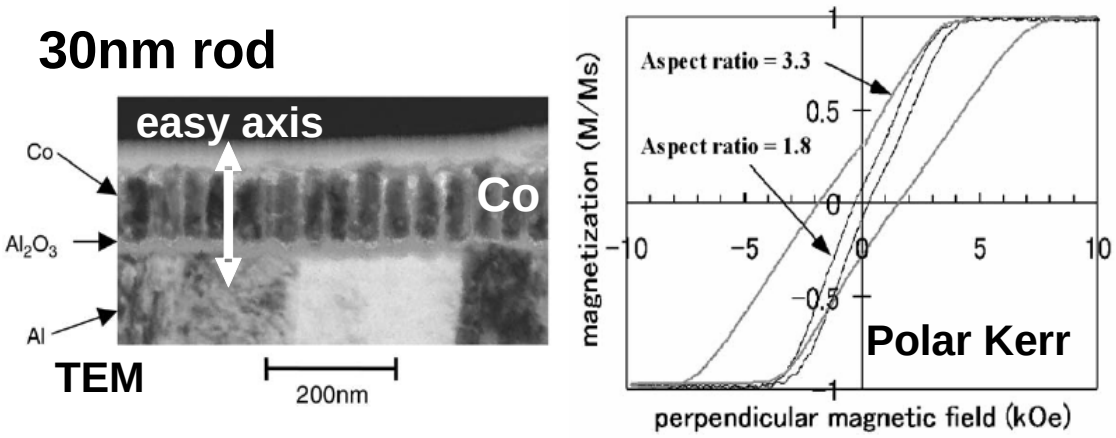

Fig.1: right: Cross-sectional TEM micrograph of Co wire array deposited by AC electroplating of 1 kHz., Left: Coercive field as a function of the AR of Co wire array under perpendicular magnetic field.

However, the study of atomic Co chains on Pt(997) revealed a perpendicular magnetization with respect to the chain axis. This shows that the spin-orbit interaction rather shape anisotropy has become dominating for magnetic anisotropy when the size is ultimately reduced. Gambardella *et al.* [2] have reported one-dimensional ferromagnetism

of Co atomic chains grown on a Pt(997) stepped surface, which cannot be expected thermodynamically. Fig.2 shows the STM topograph of the atomic chains. The monatomic chains are obtained by evaporating 0.13 monolayers of Co onto the substrate

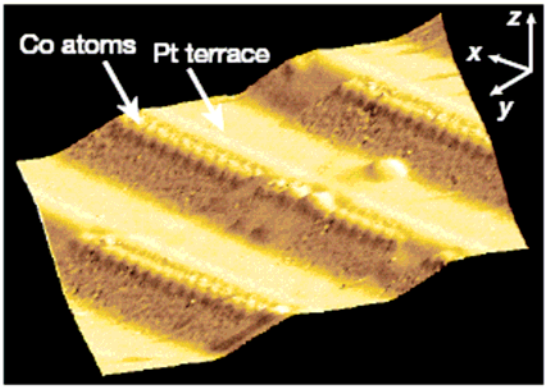

Fig.2 STM topograph of Co monatomic chains decorating the Pt(997)

held at T= 260 K and previously cleaned by ion sputtering and annealing cycles in ultrahigh vacuum (UHV). The chains are linearly aligned and have a spacing equal to the terrace width. The reduced atomic coordination of the monatomic chains compared to

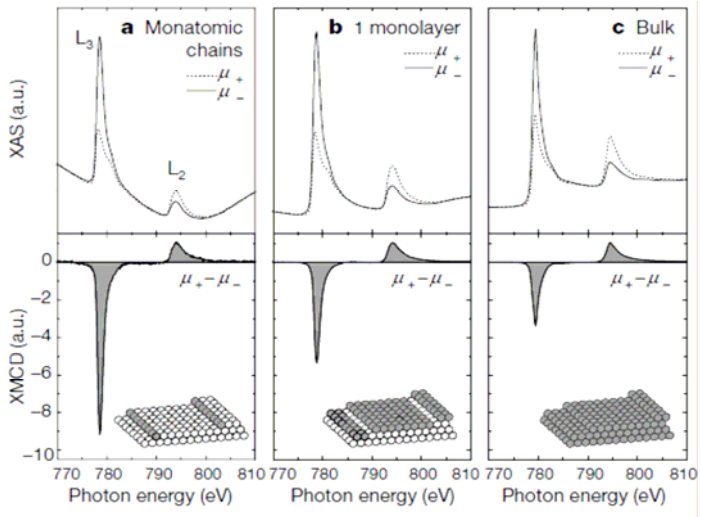

Fig.3 Co X-ray absorption spectra for parallel (m+) and antiparallel (m-) direction of light polarization and field-induced magnetization. The dichroism signal ($\mu_+ - \mu_-$) is obtained by subtraction of the absorption spectra in each panel and normalization to the L_2 peak.

bulk Co and two-dimensional (2D) has remarkable consequences for the relative size of the local orbital (m_L) and spin (m_S) magnetic moments. Both m_L and m_S are expected to increase as the atomic coordination is reduced in passing from the bulk to the monatomic chains. Fig.3 shows the XAS spectra and corresponding XMCD spectra for the

nanostructure varying from atomic chain(a) to 1 monolayer(b) and thick Co film on Pt(997) (c). The sample was mounted onto a UHV variable-temperature insert that could be rotated with the respect to the direction of the external magnetic field applied parallel to the incident photon beam. Spectra were recorded in the electron-yield mode at T =10 K and B= 7 T. As the structures from the non-magnetic substrate do not exhibit a dichroic effect, they do not contribute to the dichroic signal. Changes in the L_3 XMCD intensity indicate that the orbital moment is substantially increased in going from bulk Co to a 2D Co monolayer and, finally, to the 1D chains. As it is shown in Fig.4, the observed peculiar magnetic anisotropy of the atomic chains was found perpendicular magnetization with respect to the chain axis.

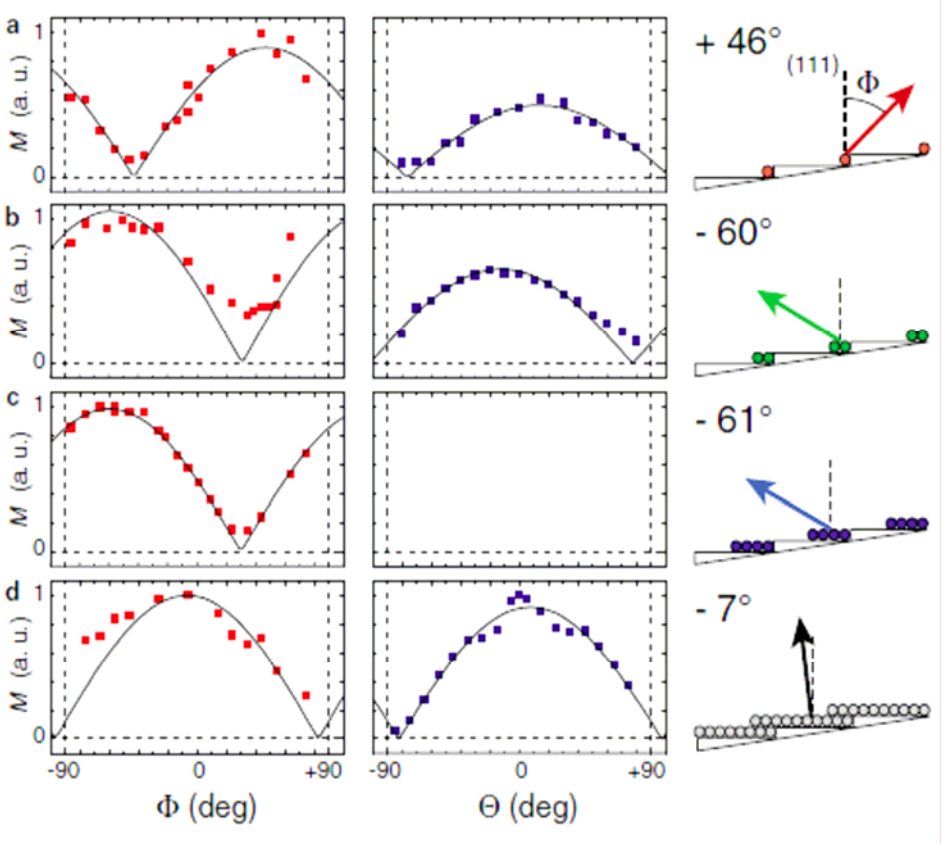

Fig.4 Co wire magnetization *M* measured at a field *Br* in the plane perpendicular to the wire axis (left column) and parallel to the wire axis (right column). The data points represent the XMCD signal at the Co L_3 edge (779 eV) normalized by the total absorption yield.

On the other hand, the critical behavior in low dimensional material represents another attractive topic but so far there are few reports on the critical behavior in one-dimensional nanostructure. Elmers *et al.* [4, 5, 7] have investigated a critical behavior of Fe one-layer ribbons on stepped W(110),shown in Fig.5. They have concluded that the critical exponent β (β is given by $M(T) = M_0(T_c - T)^{\beta}$ where M and M_0 are the magnetizations at temperatures T and T =0, respectively, and T_c the Curie temperature) is estimated as ~ 0.133, which is close to the value for the two-dimensional Ising model (0.125) and is much smaller than that for the three-dimensional Ising one (0.325).

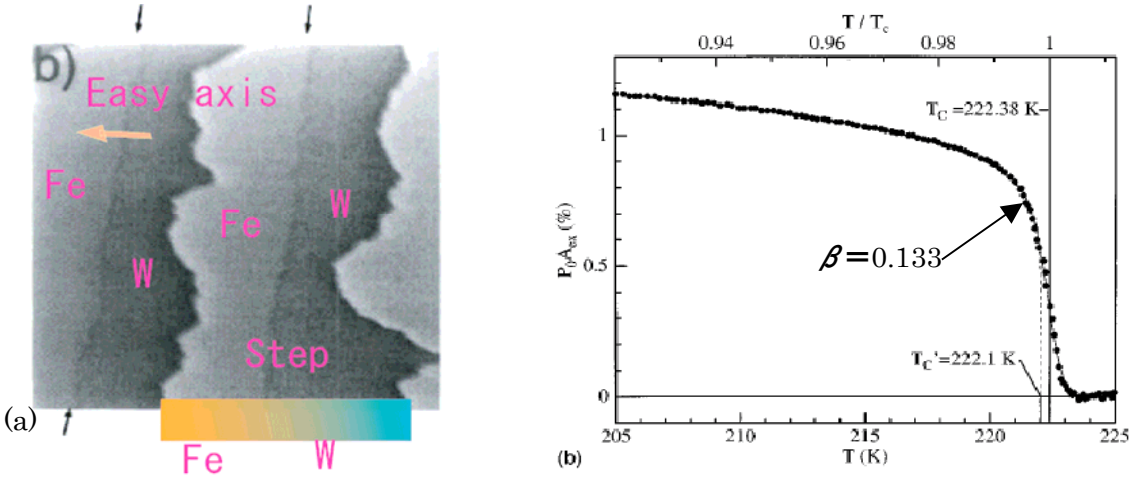

Fig. 5 (a) STM image of Fe(110) film. The strong contrast marks the edge of Fe layer. The faint contrast represents the transition from W to Fe the same level, at W steps (b) Exchange assymetry (SPLEED) versus temperature

Although these previous works concerning one-dimensional materials have successfully provided important fundamental information, the materials investigated are confined in atomic chains or one-layer ribbons. No researches have been reported so far concerning nanorods with several atoms width and height. This is mainly because the magnetic layers in these previous studies grow on step edges of the substrate surfaces in a layer-by-layer fashion and the one-layer ribbon structure is eventually merged before the second or higher layer grows. This merging tendency can be easily confirmed from the structure models presented in Fig.2 and Fig.3. Recently, York and Leibsle [9] however

discovered a self-assembled growth of Co nanorods with several atoms width and height on Cu(110)-(2×3)N (Fig.6). The Co nanorods extend along the [1 -1 0] direction and are well isolated from each other up to nominal as much as 2 ML (monolayer) Co coverage with six times periodic intervals along the [001] direction.

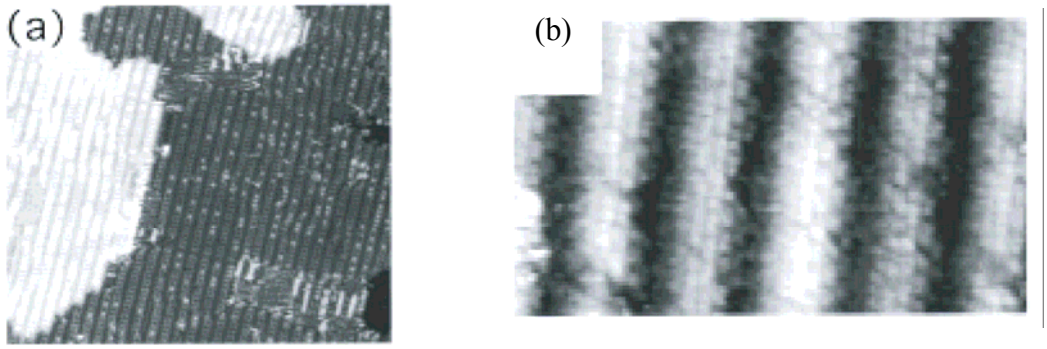

Fig.6 (a) $30\times30nm^2$ STM images showing clean Cu(110)(2×3)N structures. (b) $10\times5nm^2$ image showing atomic resolution on the surface of the nanowires.

3.2 Experimental details

Sample cleaning

The experiments were performed in an ultrahigh vacuum (UHV) surface analysis chamber with the base pressure of 1×10^{-10} Torr, equipped with an UHVcompatible electromagnet (max.3000 Oe) that allows us to measure longitudinal/polar MOKE using lasers and XMCD using synchrotron radiation. A Cu(110) single crystal was at first mechanically polished using alumina ultrafine powder with mirror finish and was subsequently cleaned in UHV by repeated cycles of Ar+ sputtering and annealing at 900 K.

N_2 treatment

Since N_2 will neither dissociate nor adsorb in molecular form on copper surfaces at room temperature, atomic nitrogen was deposited by using an ion gun to baombard the clean crystal. In order to get highly sharp LEED pattern of (2×3)N, there are several

factors which has been optimized. These parameters are summarized as follows:

N_2 sputtering time

The dose of amount of N2 is about 3600 μC. There exists a roughly saturated amount for N sputtering. In order to optimize the sputtering duration to reach the saturation, we have performed N-K edge X-rat Absorption Spectroscopy(XAS). Fig.7 shows the results. The peak intensity at 395eV(N- K edge), there is a great increase after 2 hours sputtering and the more extended sputtering does not change the N peak intensity too much.

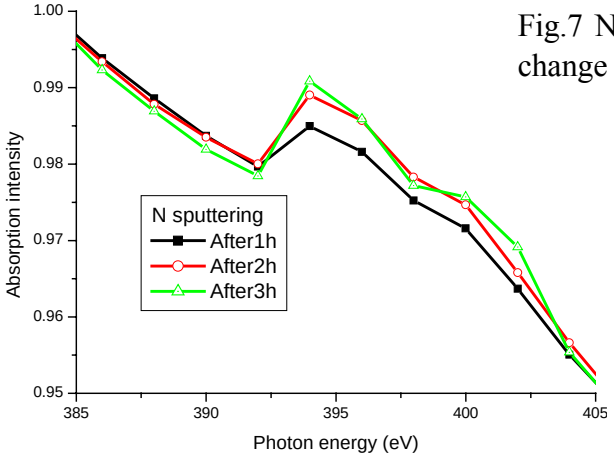

Fig.7 N-K edge XAS peak intensity change with the N sputtering time.

Annealing after N sputtering:

Although Annealing temperature after N sputtering has been suggested as around 450K~600K in many references, it is still a crucial parameter to be optimized based on the sample in use in order to get extremely good (2×3) reconstructed structure. To get the optimized factor is pure a process of trial and error. Annealing with too high temperature will immediately desorb the attached N atoms while with too low temperature the reconstruction process can not be fully completed resulting very poor LEED pattern. In this experiment, instead of watching temperature, the emission between

Annealing parameters after N sputtering:
T=650K High voltage= ~290V Emission=**39** Annealing duration=**10-12min**

annealing filament and the sample holder was monitored. Meanwhile the annealing duration is another factor of importance and it must be optimized with the chosen annealing temperature. The annealing parameters in this experiment are summarized as the above.

3.3 Structure properties:

Figure 8 shows the N-KLL and Co, Cu-MNN Auger electron spectra and the LEED images of Co-deposited Cu(110)-(2×3)N. In the LEED images of Figs. 8(d)-1(f), the (1×6) superstructures are clearly seen after Co deposition. Although the (1×6) spots become more diffuse with increasing Co coverage, the 1.8 ML Co [Fig. 8(f)] still shows the spots. The (1×6) structure is consistent with the previous STM and LEED works [9] and confirms successful preparation of the Co nanowires.

In the N-KLL Auger spectra in Fig. 8(a), it is found that the N-KLL intensity does not vary even after 5 ML Co deposition, while the Cu-MNN intensity [Fig. 8(b)] is rapidly attenuated upon Co deposition. These findings indicate that N acts as a surfactant and is located always at the surface, as in the case of Co/Cu(001)-*c*(2×2)N [12], while Cu does not significantly come up on the surface. The geometry and bonding of the Cu(110)-(2 × 3-N surface has received considerable attention because the complicated surface geometry represents a challenge to current methods of structural determination. Indeed, it has only been recently that a consensus has been reached regarding the basic geometry of the Cu atoms at the surface. The most reliable model proposed so far is a structure with the buckling at the overlayer Cu and with the surface N atoms bounded at the four fold Cu hollow sites [13-22]. Fig.9 described this mode including a assumptive

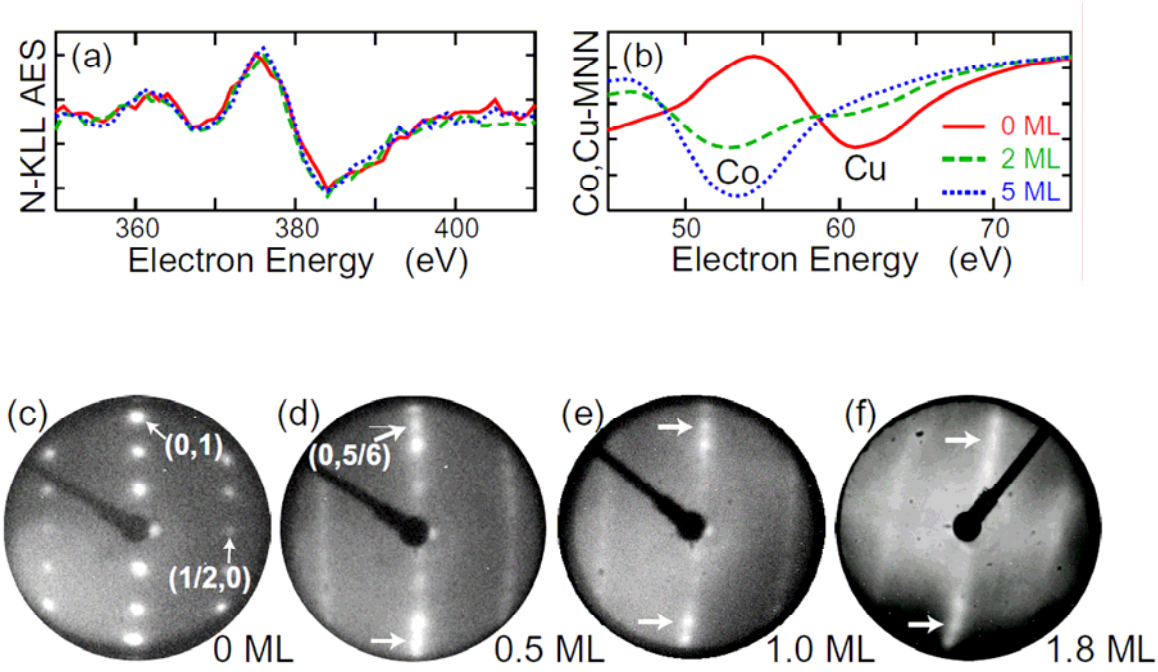

FIG. 8: (a,b) AES of N-KLL (a) and Co/Cu- MNN (b) for Co coverages of 0 (red), 2 (green) and 5 (blue) ML on Cu(110)-(2×3)N. (e-f) LEED for Co coverages of (c) 0 ML, (d) 0.5 ML, (e) 1.0 ML, and (f) 1.8 ML on Cu(110)- (2×3)N with the primary electron energies of 29 eV. Figs. 8(c), (d), and (e) were taken at 298 K, while (f) at 90 K.

growing mode for Co nanowire. This model incorporates an additional [1 –1 0] row in the outermost layer of Cu for every three found in the bulk, raising the density in this layer of 4/3 and tripling the periodicity in the [001] direction. Several important extensions are also included in this model: a large outward expansion of the compressed copper layer(57% greater then bulk spacing), a large corrugation amplitude in this layer (50% of the bulk interlayer spacing), and a related corrugation with diminished amplitude extending several layers into the substrate.

The Co nanowire formed on this substrate has an apparent ×6 periodicity rather than ×3 periodic pattern. This coagulation tendency of six times interval is the decisive driving force for the nanorod formation. However nothing is known for the dynamics regarding this coagulation behavior. Furthermore, from the Auger spectra , we have found

the N is always located on the top of Co atoms because there is no N Auger intensity reduction at all for the sample ranging from 2ML to 5ML. Including the surfactant effect from N atom during nanowire formation, it would be fascinating to perform the structure dynamics study on this system in the further study.

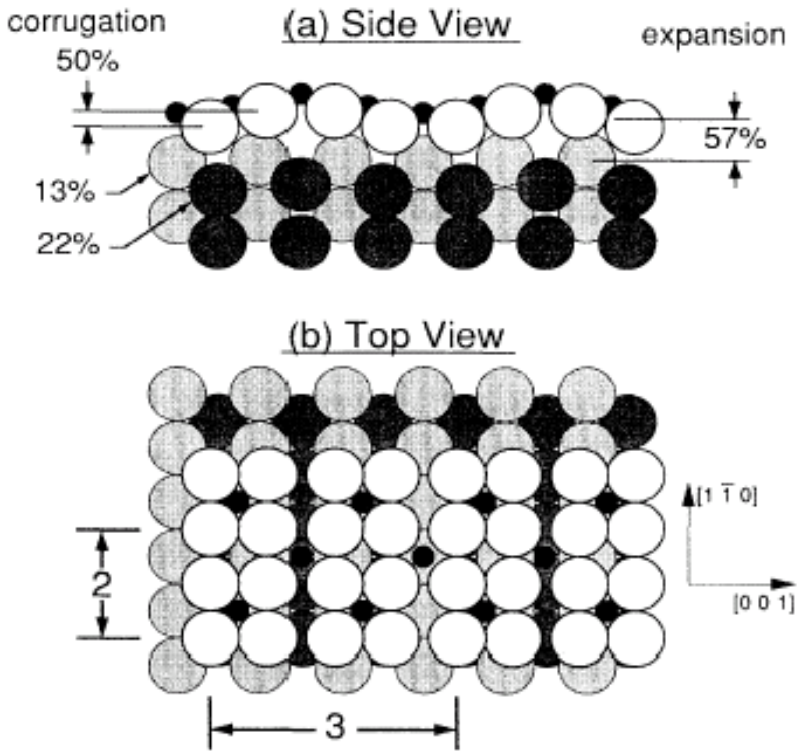

3.4 Magnetic anisotropy of Co nanorods

3.4.1 SMOKE results

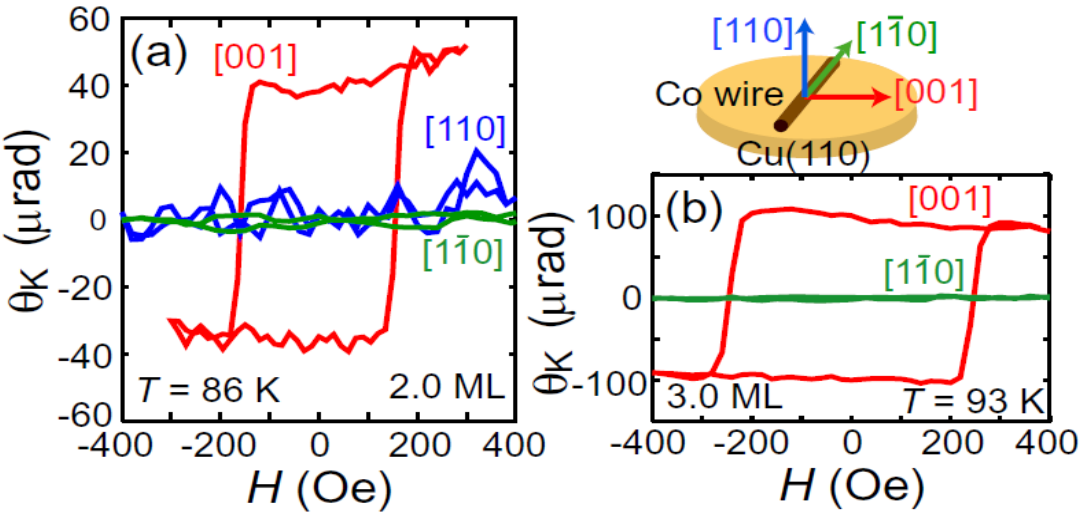

Fig. 10. Longitudinal (along [001] for red and along [1-10] green) and polar (along [110], blue) MOKE magnetic curves of (a) 2.0 and (b) 3.0 ML Co on Cu(110)-(2 × 3)N. The wire direction is depicted in the right upper panel.

Figure 10 shows the anisotropic magnetization curves of Co/Cu(110)-(2×3)N taken by the longitudinal MOKE. Both the 2 and 3 ML Co show the hysteresis loops along the [001] axis, while no prominent magnetization is seen either along [1-10] or along [110]. This implies that the magnetic easy axis is [001], which is perpendicular to the wire axis in the substrate plane. This is inconsistent with the simple consideration of the shape anisotropy but is the same as in Co islands grown on clean Cu(110) [23,24]. Since the N atom comes up to the surface, the interface interaction between Co and Cu should be similar between (2 ✕3)N and clean surfaces, possibly yielding the same easy axis. The difference of the magnetic properties between (2 ✕3)N and clean surfaces can be found in the thickness dependence and critical thickness *dc* at room temperature.

Prior to address the thickness dependence, it must be noticed that there exists strong

time effect on the magnetization variation for the Co on clean Cu(110) substrate. As it is shown in Fig.11, for the 5ML Co thin film prepared on clean Cu(110) substrate, the longitudinal Kerr signal was completely disappeared after leaving it untouched in the

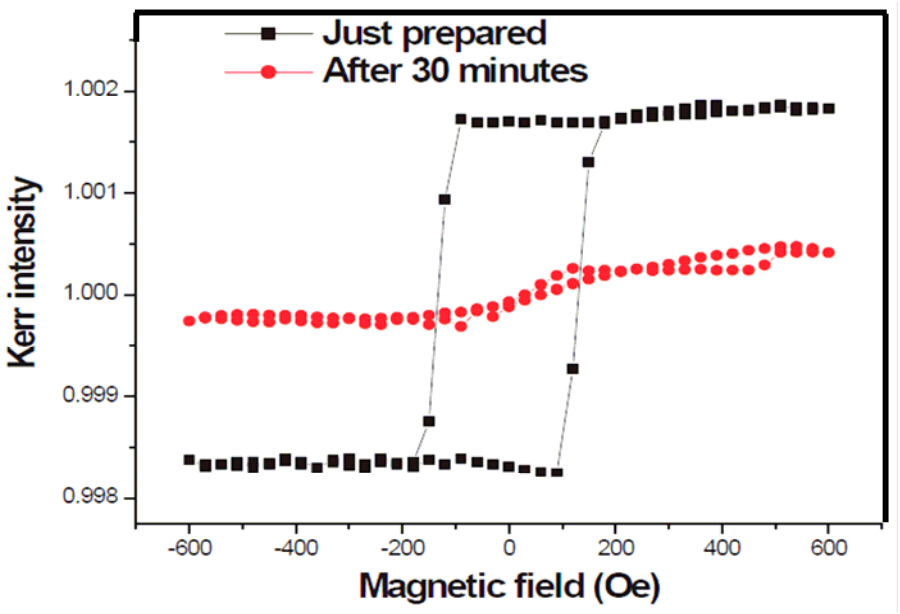

Fig.11 Time effect of 5ML Co thin film on clean Cu(110) substrate. The longitudinal Kerr signal was recorded along the [100] direction.

UHV chamber for 30min. Meanwhile the Kerr signal along the [1 –1 0] direction was detected indicating in plane spin reorientation was happened from [1 0 0] to [1 –1 0]. It has already been found out that the reason for this spin reorientation is the adsorption of CO in the UHV chamber.

However, magnetic property of the Co thin film prepared on N terminated Cu(110) substrate is found extremely stable even after leaving it in the UHV chamber for several days. This reveals another extremely important role from the relocation of N atoms on the top most of the sample. Besides aiding in the formation of nanorods as a surfactant , these top N atoms have also played a role in shielding the underneath Co nanorods from the contaminations of ambient residual gas such as the CO in the UHV chamber. This is extremely crucial for this study because it has been mentioned just before that the magnetic anisotropy of Co film on clean Cu(110) shows great time dependence due to the

CO adsorption. Owing to this natural shielding effect, the nanorods investigated here are well protected and shows very stable and long-holding magnetization. The 2.5ML Co nano ripple can be kept as long as even several days with little change of magnetization.

Thickness dependence:

Except the time effect, the N terminated system shows very different thickness

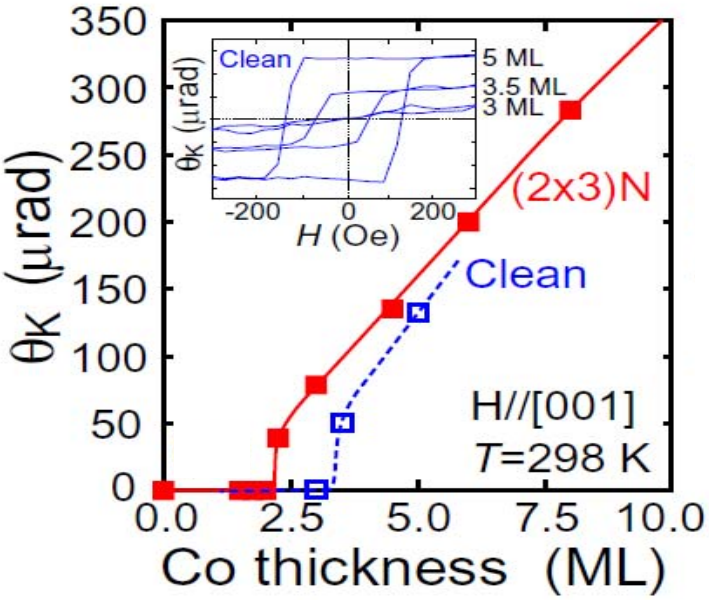

Fig.12 Critical thickness comparison for the sample prepared on clean Cu (110) substrate and the one on N terminated substrate. Inset is the thickness dependence of the Co on clean Cu substrate.

dependence from its counterpart Co thin film preparted on clean Cu substrate as shown in Fig.12. The critical thickness, where the spontaneous magnetization disappears at room temperature, is estimated as ~2.2 ML for Co/Cu(110)-(2×3)N, which is noticeably smaller than the one of ~3.3 ML for Co/clean Cu(110). It is well known that on clean Cu(110) Co exhibits an island growth mode [9,25,26] and gives much lower T_c than the layer-by-layer grown Co on Cu(001) [27]. Although the present Co/Cu(110)-(2×3)N does not show the layer by- layer growth fashion either (early grow period with thickness <2ML), the nanorods should be a larger magnetic unit than the island, resulting in higher T_c and smaller d_c.

Coercive force versus thickness

It is worthwhile to address one noticeable feature found in the Co film on N termianated Cu(110) surface. As it is shown in Fig.13, the coercivity of the Co film prepared on N terminated substrate keeps almost constant with the thickness changing from 2.25ML to 8ML. However, in contrast to this, coercivity of the Co thin film

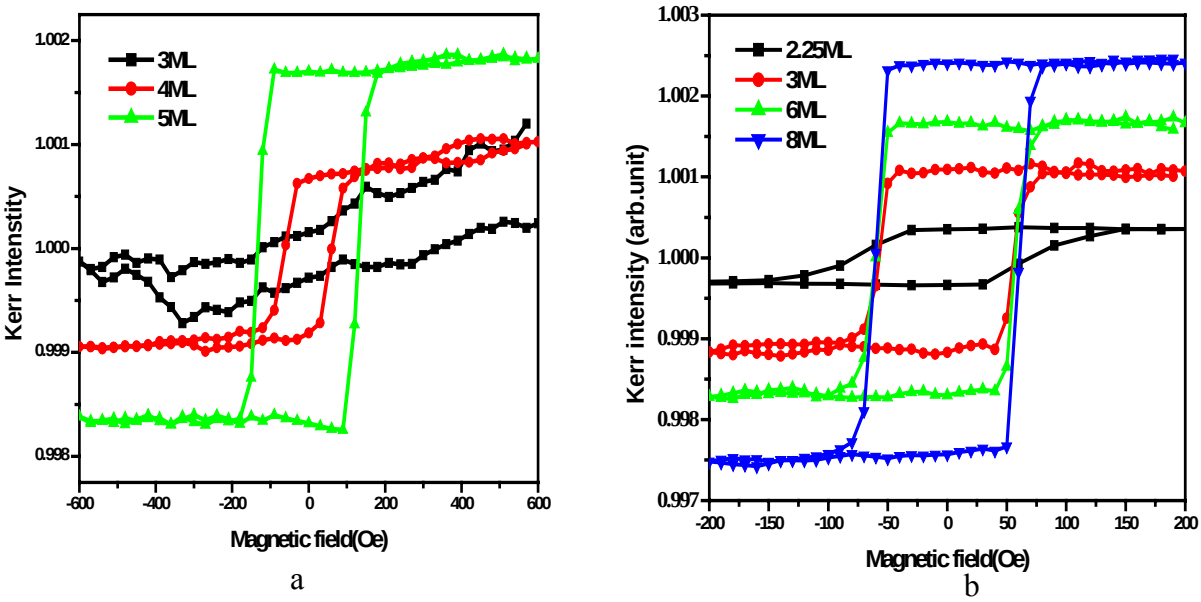

Fig.13 The dependence of coercive force on the film thickness. a: Co thin film on clean Cu(110) substrate. b: Co thin film on N terminated Cu(110) surface.

(Fig.13a) on clean Cu(110) substrate shows very strong dependence on the thickness.

The mechanism of coercivity is an enduring topic in magnetism. According to the Stoner–Wohlfarth model (SW) which based on the rotation of magnetic moments of single-domain particles with respect to their easy axes. A simplified function can be given to describe the coercivity for a bulk material with an easy axis parallel to the applied field direction [28].

$$Hc = H_K = 2K/(\mu_0 Ms)$$

Here K is the dominant crystal anisotropy constant, and Ms is the saturation

magnetization. A more complicated version can also be given by taking the surface roughness into consideration[29,30]:

$$Hc = \frac{1}{2Ms}\left(\frac{\partial \sigma_w}{\partial t} + \frac{\sigma_w}{t}\right)\rho_{ms}$$

Where ρ_{ms} is the local slope of surface. t is thickness Ms is the saturated magnetization. From the two formula, suggests that the saturation magnetization/monolayer and the local slope of surface is probably constant because the measured coercive force Hc keeps constant. In current system this means a magnetically unified structure is prepared on the N terminated substrate. It is consistent with the STM study of this system where well constructed surface ripple structure is formed by a layer by layer growing mode after the nanorods converged when the thickness >2ML. The smooth and harmonized ripple structure is the most probable reason for the extremely constant coercivity obtained.

3.4.2 XMCD results

Figure 14(a) shows the Co L-edge XMCD spectra of 2.0 ML Co on Cu(110)-(2×3)N taken at *T*=90 K and *H*=1500 Oe in UVSOR-II Beamline 4B. Note that [001] and [1-10] directions were investigated in the grazing geometry (30° away from the in-plane direction) and the spectra were normalized with cos30°. In the inset of Fig. 14(a), the normalized XMCD spectra are given, and the spectra indicate that the easy axis gives larger magnetization due to insufficient external magnetic field of 1500 Oe along the hard axes. Figure 14 (b) is the XMCD spectra normalized with the L_{II} peak intensity in order to compare the L_{III} intensities. The [001] spectrum gives the largest L_{III} intensity. The sum-rule analysis has been performed using those for the orbital magnetic moment [31] and the spin magnetic moment [32], and the results are depicted in Fig. 14(c). As the Co thickness decreases, the effective spin magnetic moment m_{spin}^{eff} (m_{spin}^{eff}=m_{spin}+7m_T), where m_{spin} the spin magnetic moment and m_T the magnetic dipole moment) along [001]

is slightly reduced from 8.8 to 2.0 ML and is abruptly suppressed from 2.0 to 1.6 ML (see the inset). The critical thickness at 90 K is estimated as ~1.6 ML. The ratio of the orbital magnetic moment with respect to the effective spin magnetic moment, m_{orb}/m_{spin}^{eff}, is larger along [001] than along [1-10] and [110], and is enhanced with decreasing the Co thickness. These results imply that the spin-orbit interaction determines the magnetic easy axis [33], as in the cases of metal thin films [34,35] and clusters [36,37].

(*see the next page*)

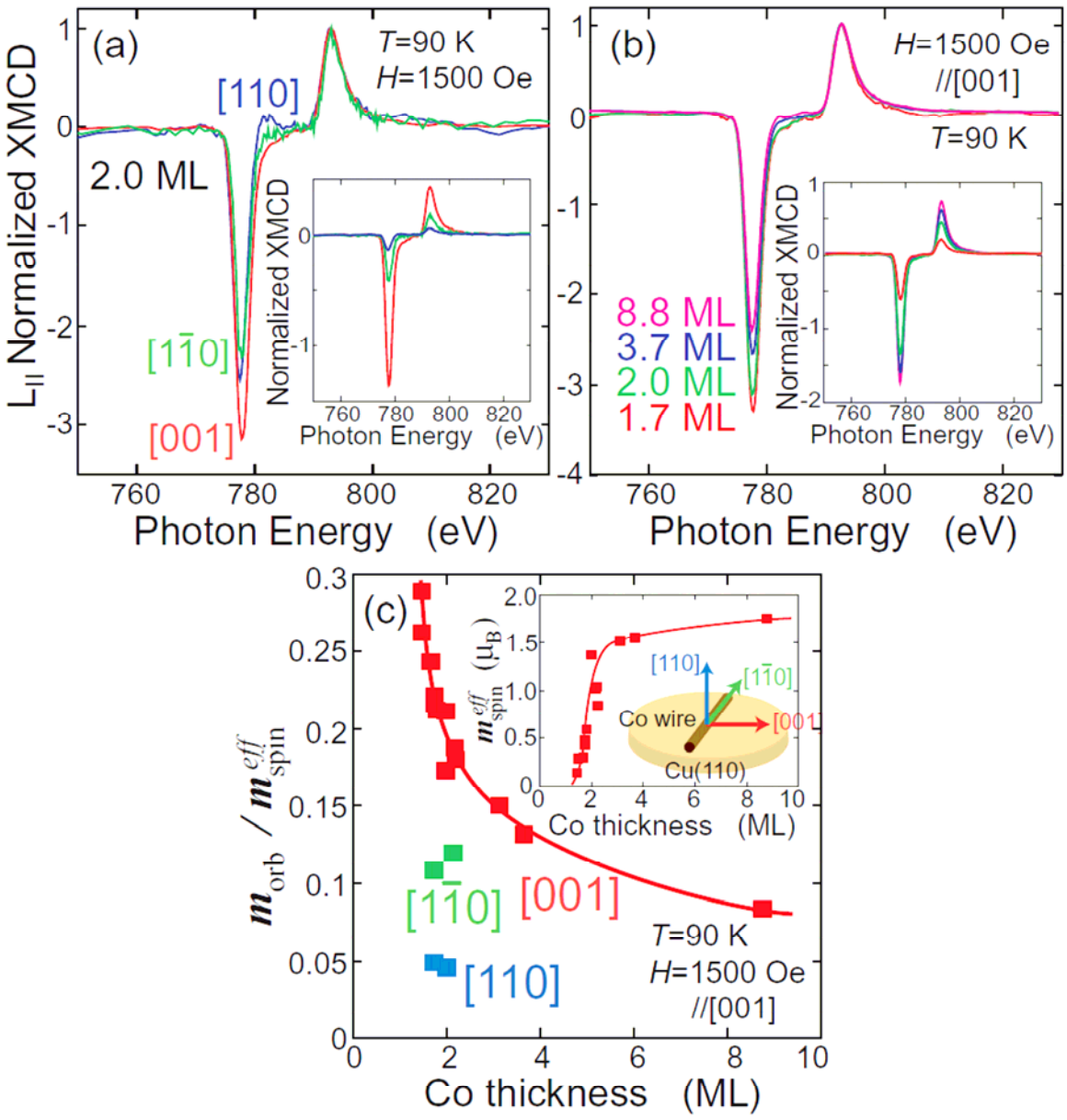

Fig. 14. (a) Co L-edge XMCD spectra of 2.0 ML Co on Cu(110)-(2´3)N at T=90 K and H=1500 Oe along the [001], [1-10], and [110] directions, normalized with the LII peak intensity. Inset shows the XMCD spectra normalized with the edge jump. (b) Thickness dependence of the Co L-edge XMCD spectra of Co on Cu(110)-(2´3)N at 90 K along the [001] direction, normalized with the LII peak intensity. Inset shows the XMCD spectra normalized with the edge jump. (c) The ratio of the orbital magnetic moment and the effective spin magnetic moment as a function of Co thickness. Inset shows the effective spin magnetic moment.

3.5 Experimental results of magnetic critical behaivor

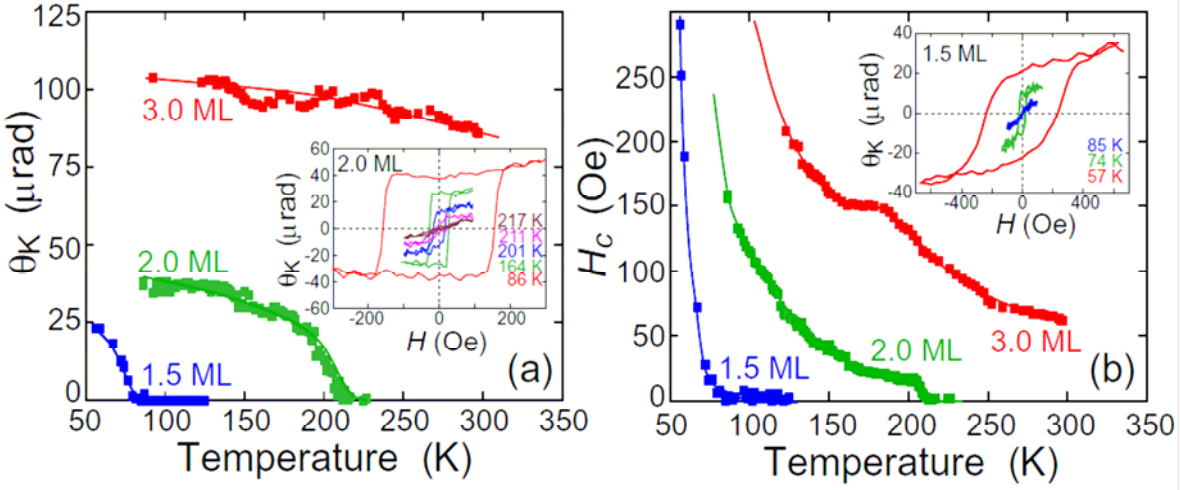

Fig.15 (a) Saturated MOKE rotation angles and (b) coercive fields of 1.5, 2.0, and 3.0 ML Co on Cu(110)-(2´3)N. Insets show the magnetization curves of 2.0 and 1.5 ML Co.

Fig.15 shows temperature dependence of the magnetizations and the coercivities of 1.5, 2.0 and 3.0 ML Co on Cu(110)-(2×3)N, recorded by the longitudinal MOKE along [001]. The insets give the typical magnetization curves. The Curie temperatures were obtained as 78.5±1.0 K (1.5 ML), 211±2 K (2.0 ML) and >300 K (3.0 ML) which can be compared to the one of ~15 K for an atomic Co chain [2]. It has been demonstrated that low-dimensional magnets show a more abrupt suppression of the magnetization in the vicinity of *Tc* than three-dimensional bulk ones. The critical exponents β were found to be 0.125 experimentally for an ultrathin Ni/W(110) film [38] and also for quasi-one-dimensional one-layer ribbons [1,4]. The value of β=0.125 corresponds to that for the two-dimensional Ising model and is smaller than the bulk Ising one of 0.325 [39]. The present observations however show more gradual attenuation of the magnetization with approaching the Curie temperature. From the curve fitting analysis of the experimental data, the critical exponents β yield β=0.56±0.10 for 1.5 ML and

β=0.32±0.05 for 2.0 ML. The critical exponent β of 1.5 ML Co is larger than the bulk value. Even when the broadening of the Curie temperature is taken into account, the same value of β is reasonable in order to explain the tail above the Curie temperature (see the right panel of Fig. 15). The broadening may be caused by the finite length of the Co nanowire.

3.6 Monte-Carlo simulations of the critical behavior

In order to obtain deeper insight of the critical behavior observed, we have performed Monte-Carlo (MC) simulations concerning the magnetic hysteresis curves and the temperature dependence. Although the magnetic reversal process accompanying hysteresis is not an equilibrium character, MC simulations are known to give reliable non-equilibrium properties, as long as the acceptance ratio is set in the range of 0.20-0.40 and slow and prolonged MC simulations are conducted [40]. Here we have employed two magnetic models for 1.5 ML Co. The first one is the single domain superparamagnetic particle (model A). Since the domain is always single in this model, only the rotational

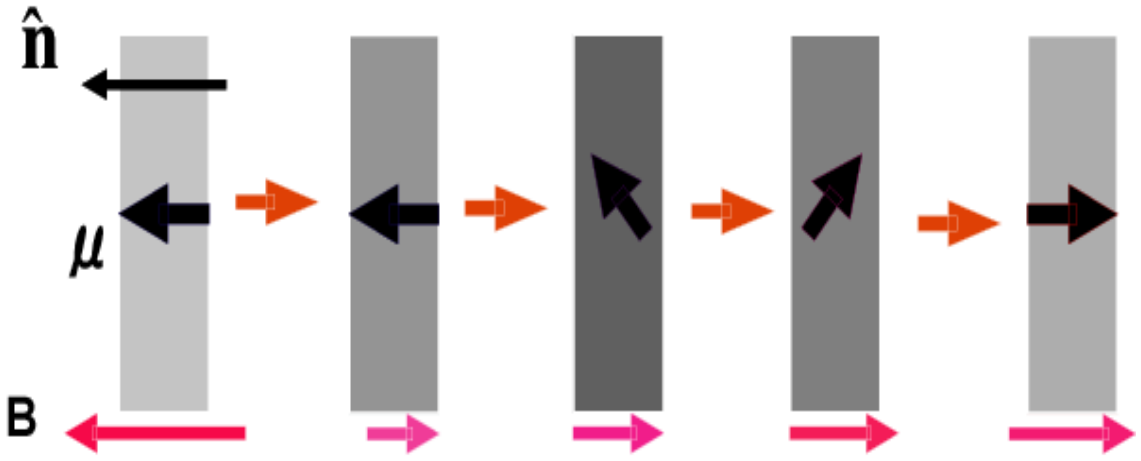

Fig. 16 Single-domain (SD) superparamagnetic model.

magnetic reversal process can occur. The Hamiltonian is expressed as: $H = -\boldsymbol{\mu}\cdot\mathbf{B} - K_u(\hat{\boldsymbol{\mu}}\cdot\hat{\mathbf{n}})^2$, where μ is the magnetic moment of the particle, B the external magnetic field, K_u the uniaxial magnetic anisotropy constant, and $\hat{\boldsymbol{\mu}}$ and $\hat{\mathbf{n}}$ are the unit

vectors along μ and the [001] axis. In this simulation, the number of MC steps was $N_{MC}=10^6$ for $N_{wire}=10^3$ nanowire particles with the acceptance ratio of 0.3-0.4. From the STM images [4], the number of atoms in each particle was set at $N_{atom}=3000$ with the assumption of the atomic magnetic moment of $1.6\mu_B$ ($\mu=3000\times1.6\mu_B$). In the simulation of the temperature dependence, the magnetization was calculated with the applied external field of 50 Oe. Figure 6 shows the simulated magnetization curve and the temperature dependence of the magnetization (green dashed lines). The magnetic hysteresis obtained experimentally is well reproduced with this model when the uniaxial

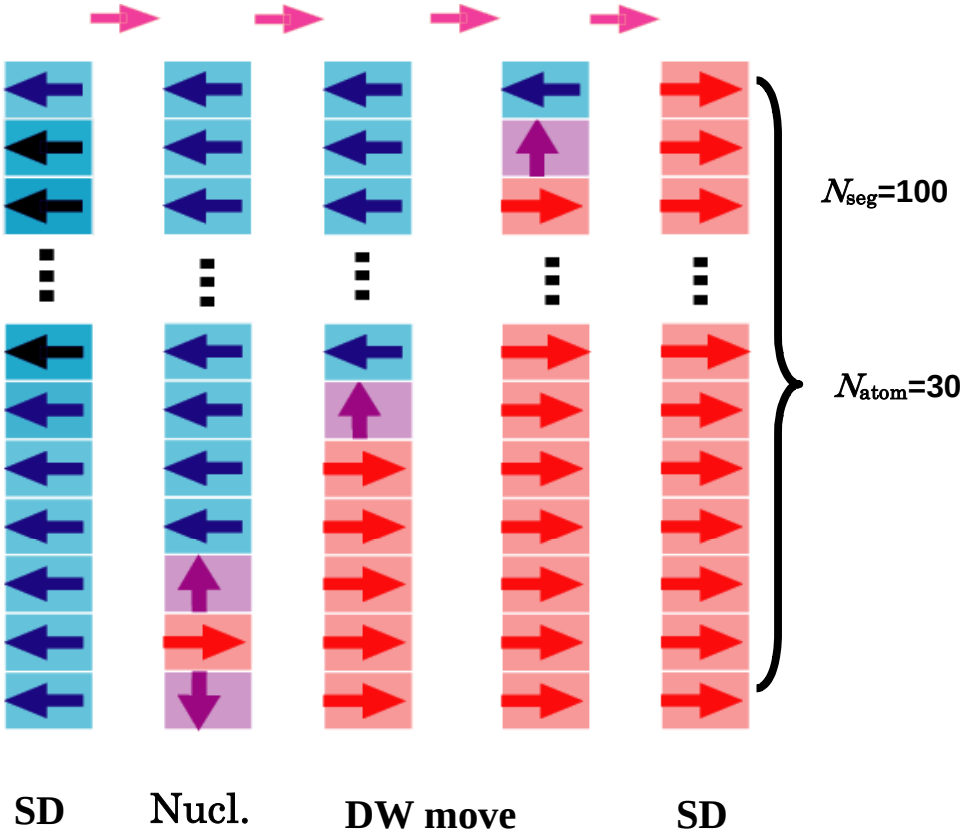

Fig. 17 Multiple domain spin segment model:

magnetic anisotropy constant is assumed as 0.29 μeV/atom. Although the model is not realistic, the estimated Curie temperature is 78 K, which excellently agrees with the experimental observation of 78.5 K, and the broadening of the critical behavior is also identified. Moreover, we have performed the MC simulations using the second model whereby the domain wall movement can be taken into account (model B). The model can

be called multidomain spin segment model. The Hamiltonian is given as

$$H = -\sum_{i} (\mathbf{B} \cdot \boldsymbol{\mu}_i + K_u (\hat{\boldsymbol{\mu}}_i \cdot \hat{\mathbf{n}})^2) - J \sum_{<i,j>} \boldsymbol{\mu}_i \cdot \boldsymbol{\mu}_j$$

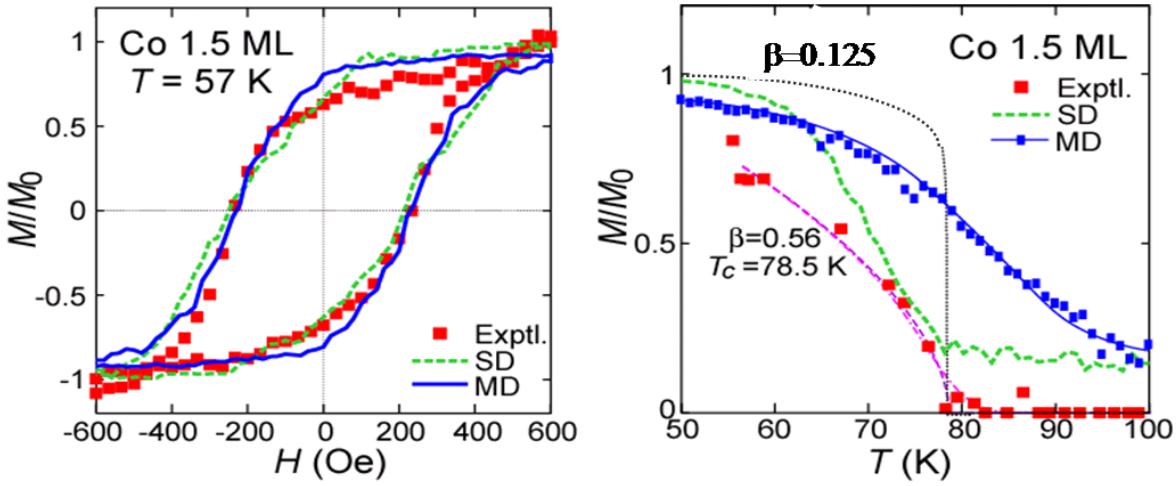

where J is the exchange coupling constant between nearest neighbor spin segments i and j. Exchange or magnetic dipole interactions between wires were neglected. Here we set N_{wire}=100, $N_{segment}$=100, N_{atom}=30, μ=30×1.6μ_B, and N_{MC}=10^5. The number of atoms in each wire is N_{atom}=3000. The experimental magnetic hysteresis curve is again reproduced quite well when the uniaxial magnetic anisotropy constant is 46 μeV/atom. This value is much larger than the fourth-order megnetocrystalline anisotropy for bulk fcc Co (0.21 μeV/atom) and also the uniaxial magnetic anisotropy for bulk hcp Co (28 μeV/atom). The temperature dependence shows more gradual reduction of the magnetization with increasing temperature. It can be concluded that the present finding of the broadened critical behavior is cuased by the finite length of the Co nanowires.

Conclusion:

The dense Co nanorod with several atoms wide and high grown on Cu(110)-(2×3)N shows the [001] magnetic easy axis perpendicular to the rod axis within the substrate plane and correspondingly a significant enhancement of the orbital magnetic moment along [001]. The critical behavior of the Co nanorods is found to be much broader than that of the two-dimensional Ising model, due to the finite length of the Co nanorods.

Reference:

[1] H. Fujisawa, S. Shiraki, et al J. Electron Spectrsc. Relat. Phenom. 144-147, 519 (2005).

[2] P. Gambardella, A. Dallmeyer, et al, Nature 416, 301 (2002).

[3] P. Gambardella, A. Dallmeyer, et al, Phys. Rev. Lett. 93, 077203 (2004).

[4] H. J. Elmers, J. Hauschild, et al, Phys. Rev. Lett.73, 898 (1994).

[5] H. J. Elmers, J. Hauschild, et al, Phys. Rev.B 54, 15224 (1996).

[6] J. Shen, R. Skomski, et al , Phys. Rev. B 56, 2340 (1997).

[7] J. Hauschild, H. J. Elmers, et al Phys. Rev. B 57, R677 (1998).

[8] F. Komori, K. D. Lee, K. Nakatsuji, et al Phys. Rev. B 63, 214420 (2001).

[9] S. M. York and F. M. Leibsle, Phys. Rev. B 64, 033411 (2001).

[10] T. Nakagawa, H. Watanabe, and T. Yokoyama, Phys.Rev. B 71, 235403 (2005).

[11] T. Gejo, Y. Takata, T. Hatsui, et al, Chem. Phys. 289, 15 2003).

[12] D. Sekiba, S. Doi, K. Nakatsuji, et al, surf.Sci. 590, 138 (2005).

[13] D. Hesket, A. Baddorf and E.W. Plummer, Surf. Sci. 195, 94 (1988)

[14] A.W. Robinson, D.P. Woodruff, et al. 237, 99 (1990)

[15] M.J. Ashwin and D.P. Woodruff, Surf. Sci. 237, 108 (1990)

[16] H. Niehus, R. Spitzl, K. Besocke and G. Comsa, Phys. Rev. B 43, 12t619 (1991).

[17] D.T. Vu Grimsby, M.Y. Zhou et al Surf. Sci. 271, 519 (1992)

[18] A.P. Baddorf, D.M. Zehner, et al Phys. Rev. B 48, 9013 (1993). .

[19] D.T. Vu and K.A.R. Mitchell, Phys. Rev. B 49, 11t515 (1994).

[20] H.A. Dürr, D.B. Poker, D.M. et al, Phys. Rev. B 49, 16t789 (1994).

[21] L. Wilde, N. Pangher and J. Haase, Surf. Sci. 347, 33 (1996)

[22] A.P. Baddorf and D.M. Zehner, Surf. Sci. 238, 255 (1990)

[23] J. Fassbender, G. G üntherodt, et al, Phys. Rev. B 57, 5870 (1998).

[24] W. L. Ling, Z. Q. Qiu, et al, Phys. Rev. B 63, 024408 (2000).

[25] E. Gu, S. Hope, et al, Phys. Rev. B 60, 4092 (1999).

[26] S. Hope, E. Gu, et al , Phys. Rev. B 57, 7454 (1998).

[27] P.Poulopoulos, P. J. Jensen, et al, Phys. Rev. B 65, 064431 (2002).

[28] G P Zhao, M G Zhao et al J. Phys.: Condens. Matter 17, 151–160 (2005)

[29] Y.-P. Zhao, R. M. Gamache, et al J. Appl. Phys. 89, 1325(2001)

[30] M.P.Sharrock J. Appl. Phys. 76, 6413 (1994)

[31] B. T. Thole, P. Carra, et al, Phys. Rev. Lett. 68, 1943 (1992).

[32] P. Carra, B. T. Thole, M. Altarelli, and X. Wang, Phys. Rev. Lett. 70, 694 (1993).

[33] P. Bruno, Phys. Rev. B 39, R865 (1989).

[34] M. Tischer, O. Hjorstam, D. Arvanitis, J. H. Dunn, et al , Phys. Rev. Lett. 75, 1602 (1995).

[35] N. Nakajima, T. Koide, et al, Phys. Rev. Lett. 81, 5229 (1998).

[36] C. Antoniak, J. Lindner, et al, Phys. Rev. Lett. 97, 117201 (2006).

[37] P. Gambardella, et al., Science 300, 1130 (2003).

[38] Y. Li and K. Baberschke, Phys. Rev. Lett. 68, 1208 (1992).

[39] D. C. Mattis *The Theory of Magnetism*, vol. II (Springer-Verlag, Berlin, 1985).

[40] D. A. Dimitrov and G. M. Wysin, Phys. Rev. B 54, 9237 (1996).

Effect of surface chemisorption on the spin reorientation transition in magnetic ultrathin Fe film on Ag(0 0 1)

Xiao-Dong Ma, Takeshi Nakagawa, Toshihiko Yokoyama

Surface Science, 600, 4605▪4612 (2006)

4.1 Introduction:

Magnetic thin films have been exciting subjects for researchers due to its novel behavior of quasi-two-dimensional systems. The broken symmetry at the interfaces in these systems has been confirmed to contribute directly to the characteristic magnetic properties such as moment enhancements, magnetic surface anisotropy effects, unusual spin-excitation spectra and reduced Curie temperature [1-10]. Among them, epitaxial Fe(001) thin film grown on Ag(100) presents a very attractive model of being such a system. The lattice constants of bcc Fe and fcc Ag differ by $\sim 2^{1/2}$; therefore, a 45° relative orientation of the (100) surfaces results in almost perfect registry(0.8 mismatch) [1,2], as shown in Fig.1.

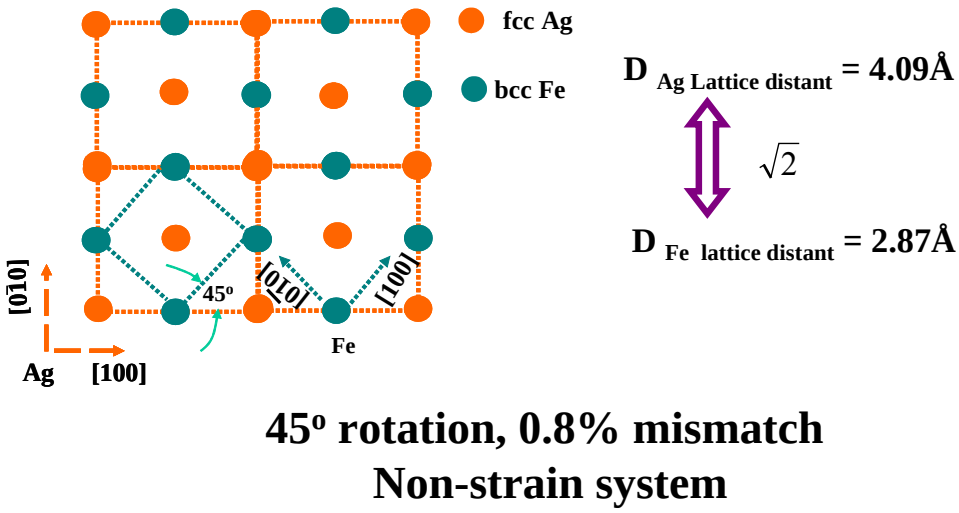

Fig.1: The structure feature of epitaxial Fe thin film grown on Ag(001) substrate.

Furthermore, the overlayer and substrate bands has a very little interaction; the only hybridization is through the Ag *sp* bands and is nearly negligible [2-4]. Both theoretical prediction[2,4] and the direct squid observation[3] showed significantly enhanced magnetic moments (>30% above the bulk value) for monolayer or bilayer Fe films on Ag (100). Meanwhile the modifications of DOS(density of states) from narrowed *d* bands which cause larger spin moments are likely to produce enhanced orbital moments through

spin-orbit coupling like those found in Co on Cu(100) [36]. Fig.2 shows energy bands along high-symmetry directions for a monolayer of Fe on Ag(001). Majority spin bands are on the left and minority-spin bands are on the right. In (a) are those bands that are odd with respect to reflection in the mirror plane perpendicular to the surface and (b) exhibits the even bands. The solid (dashed) energy bands correspond to wave functions symmetric (anti-symmetry) with respect to the reflection in the $z = 0$ plane. The Fe *d* bands are lie essentially within the horizontal solid lines above the Ag *d* bands and are quite narrow. Also the Ag minority-spin *d* bands differ relatively little from the majority-spin bands,

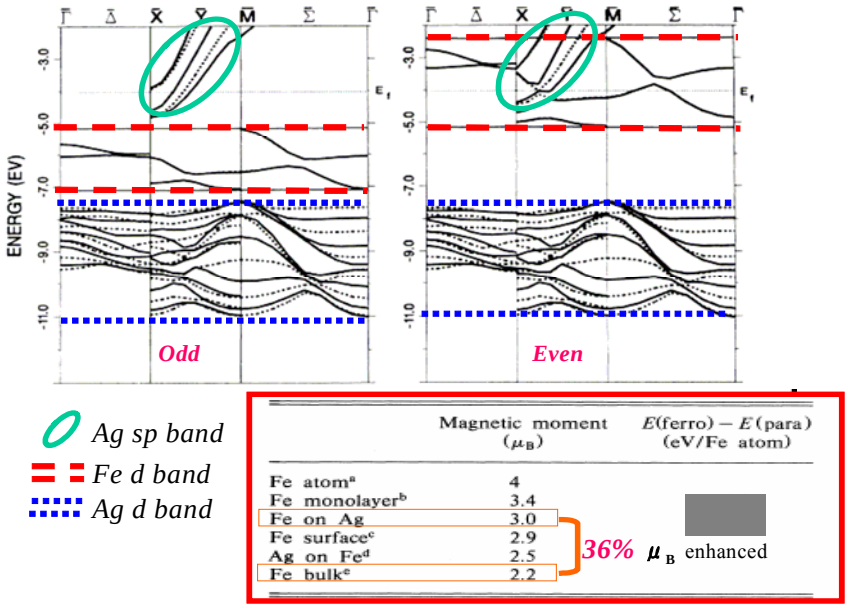

Fig.2: The band structure feature of epitaxial Fe thin film grown on Ag(001) substrate.

while the *sp* bands show large difference. The most striking feature of Fig.1 is the large splitting between minority- and majority- spin *d* bands o-f Fe. This splitting is slightly larger than the Fe *d*-band width, leading a separation of majority- and minority-spin bands. This system is extremely unique because the Fe d bands do not overlap the Ag d bands even after spin polarization. The total energy difference listed in Fig.1 confirms this. The total energy of the Fe/Ag(100) system is lowered by 1.2 eV per Fe atom as a result of spin polarization, that of the isolated Fe monolayer is lowered by1.3eV. Thus the change in binding energy of Fe layer to the Ag is –0.1eV., the bond is weakened very slightly.

Regarding the magnetic anisotropy property, this system has been explored by numerous experimental approaches and extensive theoretical calculations since the first theoretical calculations by Gay and Richer [2] have predicted that a free-standing Fe(001) thin film should possess a large uniaxial anisotropy with easy axis perpendicular to the surface [4,10-15].

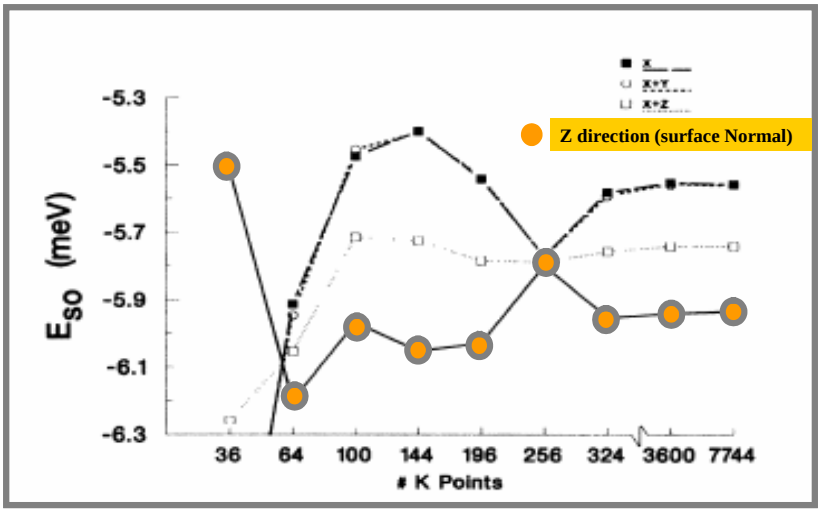

Fig.3: Spin-orbit energy Eso of a Fe monolayer for four directions of spin quatization as a function of the number of $k_{//}$ vectors used to approximate the intetral over the first Brillouin zone. The easy axis is presented by yellow spots.

Fig.3 shows Sself consistent local-orbital (SCLO) Calculation of Free standing Fe 1ML using lattice constant of Ag so as to represent as closely as possible a Fe thin film grown on Ag(001) substrate . The plot shows the spin-orbit energy Eso of a Fe monolayer for four directions of spin quatization as a function of the number of $k_{//}$ vectors used to approximate the integral over the first Brillouin zone. z is perpendicular to the plane of the monolayer and x is along a nearest neighbor direction in the plane of the monolayer. The plots shows the large number of k vectors required for convergence and that, at convergence, the easy axis is perpendicular to the monolayer.

Based on the magnetic anisotropy mentioned above, we can go further to address the spin reorientation occurred in this system. As having been described in the introduction

part, it has been generally accepted that the easy axis of two-dimensional ultrathin magnetic films is governed by its magnetic anisotropy energy, which is dominated by a competition among spin orbit coupling governed magnetoelastic and magnetocrystalline anisotropy as well as the dipolar interaction involved shape anisotropies [16-18]. Variation in surroundings such as thickness and temperature can have a large effect on the morphology in thin film, which accordingly alters both the magnetocrystalline and the magnetic dipolar anisotropy and results in the spin reoriented toward the easy axis of the magnetization. In the Fe/Ag system, It has been confirmed[10] that the surface anisotropy which favors perpendicular magnetization in this system can prevail over the shape

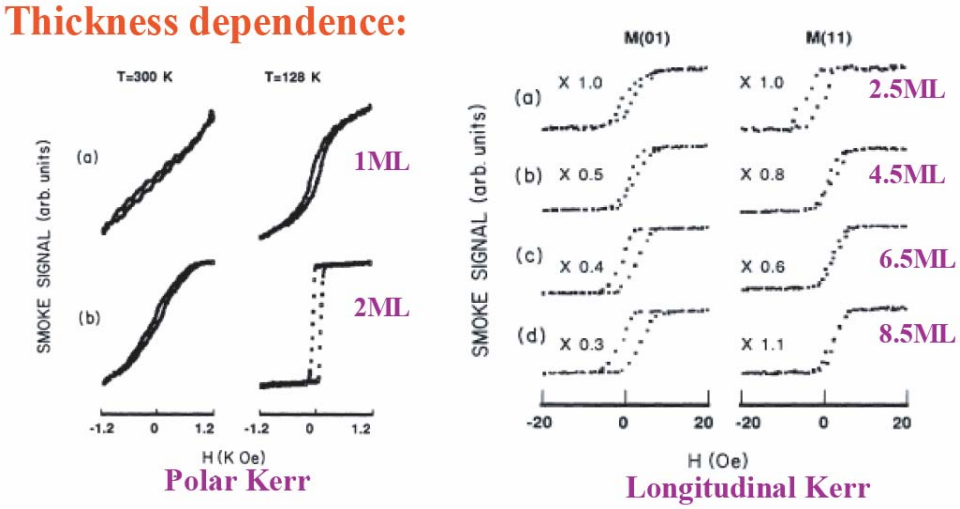

Fig.5: Thickness variation induced spin reorientation in Fe/Ag(001) surface.

anisotropy in the ultrathin region(<2ML) and cause an out of plane magnetization easy axis. A detailed second-variation full-potential linear augmented-plane-wave total-energy calculation [19] implied the spin orbital interaction is the key reason for surface magnetic anisotropy preferring perpendicular magnetization. The temperature and thickness dependent spin reorientation transition have been intensively investigated on Fe films on flat and wedge shaped Ag samples [6, 20,21].

Fig.5(left) displays hysteresis curve for epitaxial films of Fe on Ag(100) using the longitudinal configuration in which the applied magnetic field is in the plane of the film

and parrel the plane of incidence. Two orientations of the crystal were investigated, one in which the [1 1] direction was parallel to the applied filed *H* and one in which the [1 0] direction was arranged to parallel to *H*. Fig.5(right) shows corresponding hysteresis cureves for the polar configuration in which H is applied along the crystal's normal direction.. It apparently shows that a single of Fe film is ferromagnetic. The coercive force of the film at room temparture is small (suggest that multiple domains are present for zero applied field) and temperature dependent. No kerr-effect signals were detected for H parallel to the surface for films less than 2-ML while polar Kerr-effect was observed for single and double layers of Fe film. These features are consistent with preferred spin alignment perpendicular to the surface for thickness<2ML and parallel to the surface for above 2ML.

Besides the thickness and temperature, the effect of surface chemisorption on the spin reorientation transition in magnetic thin film represents another interesting subject [22-25]. For Fe/Ag system, the first and only experimental chemisorption study done by *Chen* et al[15] revealed that oxygen adsorption, acting as a surfactant, increased the order of the thin film structure. A flatter surface was thus obtained due to the reduction of surface energy

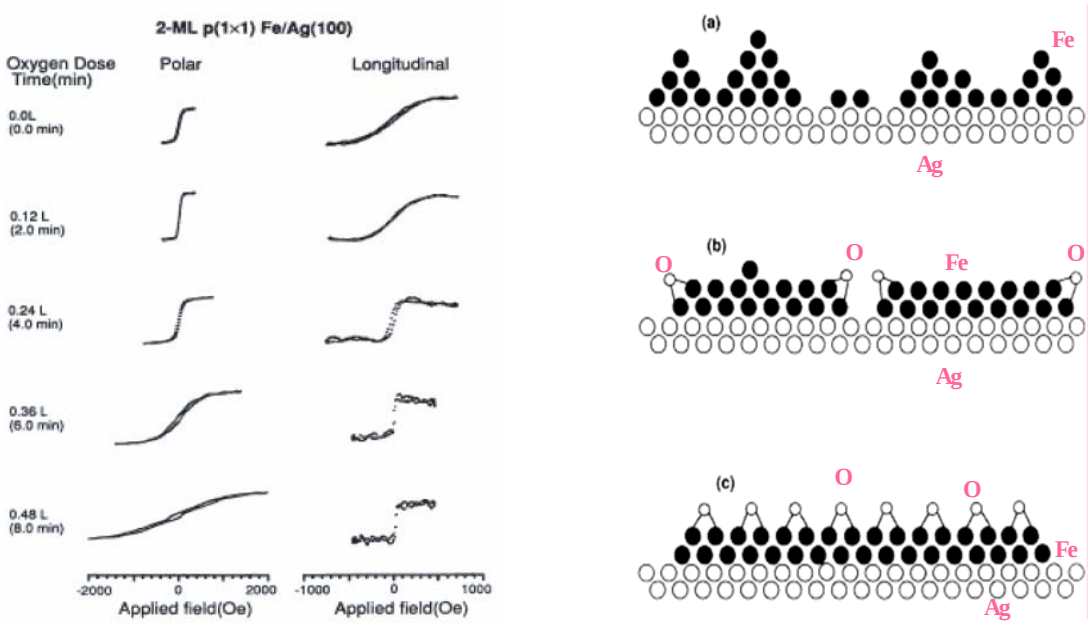

Fig.6: Oxygen adsorption induced Spin reorientation from out of plane to in plane. O_2 acting as a surfactant to flatten Fe thin film on Ag(001).

and the promoted wetting between Fe and Ag (shown in Fig.6). Meanwhile a destabilization of perpendicular magnetization was found due to the oxygen adsorption. However, since the critical thickness of transformation from perpendicular to parallel was found insensitive to the films having different step densities and the films prepared at different temperature, the results appeared to suggest the thin film anisotropy of Fe/Ag(001) is dominated by spin orbit contributions which govern the surface anisotropy parameter while the structure reconstruction effect is not the driving force for the change of magnetization direction.

Pick et al [27] carried out a theoretical calculation based on a semiempirical tight-binding model to study the chemisorption effect. The calculated results showed that the originally preferred perpendicular magnetization changed into in-plane one and the energy change grew with Fe interlayer expansion driven by oxygen. We must notice here that the key hypothesis used in this calculation that the surface magnetism is by no means quenched by oxygen may not always hold due to the following reason. Theoretical calculation[28] in oxygen adsorption on single crystal Fe surface do have found that the magnetic moment of the clean metal film was not quenched by oxygen adsorption. However, the experiment results based on single crystal always can not be extended to cover the thin film study, especially we are here dealing with ultra thin film with thickness of 2ML or less. The variation of spin magnetic moment cannot be ruled out due to chemical bonds between Fe and O atoms.

There have been reported also no experimental proofs to directly verify that the spin-orbit coupling is decisively responsible for the observed destabilization of perpendicular magnetization after oxygen absorption on Fe/Ag(001). Moreover, a deeper insight of the effect of oxygen absorption on the morphology of thin films is usually hampered without making a comparison to other sorts of gas adsorption. Therefore, a systematic study regarding various gas adsorption effects on the Fe/Ag(001) system is necessary. For these purposes and requirements, we have performed a combined *in situ* magneto-optical Kerr effect (MOKE) and X-ray magnetic circular dichroism (XMCD)

studies of chemisorption induced spin anisotropy change in ultrathin Fe films grown on Ag(001) at 100 K. As the source of chemisorbed gases, we have employed three different gases of O_2, NO and H_2. Our sample preparation is based on Ref. [25], where a layer-by-layer growth mode was observed by reflection high energy electron diffraction (RHEED) for Fe films prepared on Ag(001) at 100 K. We have examined the spin reorientation transitions in clean and adsorbed Fe/Ag(001) by means of polar and longitudinal MOKE. We have also performed the XMCD measurements of all the samples in order to obtain the spin and orbital magnetic moments, which are directly related to the microscopic origin of the magnetic anisotropies.

4.2 Experimental details

Films in the experiment reported here were prepared and studied *in situ* at pressure below 2×10^{-8} Pa in our MOKE and XMCD chamber [26]. The Ag(001) substrate was cleaned by repeated cycles of Ar^+ sputtering at 1 keV and subsequent annealing at 900 K. The sample was annealed by electron bombardment from the rear side of the crystal, and its temperature was monitored by a chromel-alumel thermocouple. Carbon contamination was removed under oxygen gas ambient by annealing the sample at 600 K with the pressure around 2×10^{-6} Pa. The cleanliness and structure ordering were confirmed by low energy electron diffraction (LEED) and X-ray absorption spectroscopy (XAS). A sharp 1×1 LEED pattern was obtained with low background indicating a well-defined Ag(001) substrate. The Fe films were deposited from commercial evaporators at substrate temperature of 100 K and pressure below 4×10^{-8} Pa and the evaporation rate was set at ~0.2 ML/min. The wedge films were prepared by placing a Cu mask in front of the Ag substrate to block part of the evaporated Fe beam and by slowly translating the mask along the [010] crystal direction. The speed of the translation motion was automatically motor-controlled. The Fe wedge gives a thickness gradient of 0.6 ML/mm. Regarding the critical thickness of perpendicular magnetization transformed into in plane in Fe/Ag(001) system, several important discrepancies exit between various experimental results [13,22]. We calibrated the thickness by a XAS intensity ratio between Ag *M* and Fe *L* edges and determined the d_c (critical thickness) is around 3 ML, which is consistent with the one

reported by Chen *et al*. [22]. The dosages of oxygen, nitric oxide and hydrogen were determined through a relation of one Langmuir 1 L=1×10^{-6} Torr·s [1 Torr = 133 Pa]. *In situ* LEED observation was used during oxygen adsorption. It showed more blurred spots with higher oxygen dosage rather than a significant reduction of the spot size.

The MOKE experiment was performed at 100 K using a diode laser (635 nm, CW), a pair of polarizers and an electromagnet with a maximum magnetic field of ~2500 Oe. The laser was focused onto the sample (~0.2 mmϕ) with the incident angle of 45° for both longitudinal and polar configurations. The Kerr rotation angles were measured as a function of a magnetic field to yield magnetization hysteresis curves. Both flat and wedge-shaped Fe films were prepared depending on the purpose.

The XMCD experiment setup is basically the same as our previous report [26]. The Fe $L_{III,II}$-edge XMCD spectra were taken at the bending-magnet station Beamline 4B [27] at UVSOR-II, Institute for Molecular Science (IMS), Okazaki, Japan. Circularly polarized X-rays were obtained by using the upper (0.4±0.1 mrad, positive helicity) or lower (–0.4±0.1 mrad, negative helicity) part from the synchrotron orbit plane. The circular polarization factor P_c is estimated to be 0.70 from the storage ring and beamline parameters, and is in good agreement with the evaluation from the reference spectra of thick Co films. The energy resolution was $\Delta E/E$~10^{-3} around ~700 eV. For the XMCD experiments, flat Fe films were prepared with the Fe thicknesses of 1.2 and 4.8 ML, which show perpendicular and in-plane magnetic easy axes, respectively. Before the XMCD measurement of each sample, hysteresis curves were recorded by measuring polar (for 1.2 ML Fe) or longitudinal (for 4.8 ML Fe) MOKE in order to make direct comparison between XMCD and MOKE reliable. The incident angles of X-rays were set at 0° (normal X-ray incidence) for the 1.2 ML Fe film and at 30° (grazing X-ray incidence) for the 4.8 ML Fe film. During the XMCD measurements, a magnetic field of 1000 G was applied to saturate the sample magnetization along the easy axis, and the XMCD spectra were recorded with the reversal of the magnetic field as well as the helicity of X-rays. We took all the XAS by monitoring the total electron yield, and simultaneously we measured the intensity of the incident X-rays (I_0) with an Au-coated *W* mesh placed in front of the sample.

It is here noted that the Fe $L_{III,II}$-edge XAS of the 1.2 ML Fe films are originally overlapped with the Ag *M*-edge XAS and show weak but non-negligible oscillations with a long period due to the appearance of the Ag *M*-edge EXAFS (extended X-ray absorption fine structure). This provides, however, no serious problem in the XMCD analysis as long as the subtraction of the background spectrum from clean Ag(001) was performed prior to the XMCD analysis. Measurements of the background spectrum were found to be important. After the subtraction of the background spectrum, we successfully performed pre-edge linear background subtraction and normalization with the Fe $L_{III,II}$ edge jumps. This correction was conducted for all the spectra of 1.2 ML Fe.

4.3 SMoke Results

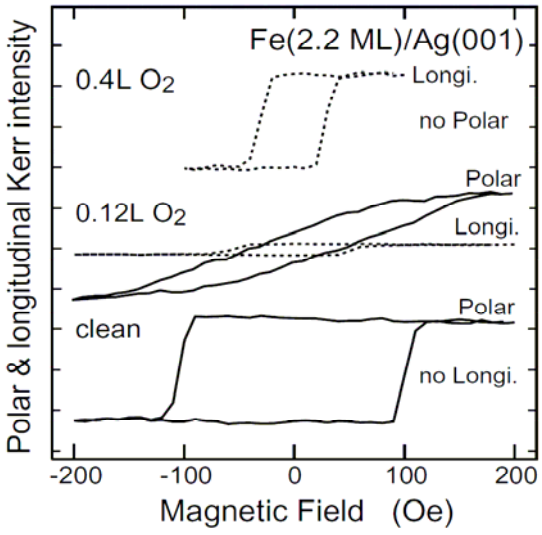

Fig. 7. Magnetization hysteresis curves taken at 100 K by the polar and longitudinal MOKE measurements for clean and O-adsorbed Fe(2.2 ML) films on Ag(001). The flat Fe film was used.

First, we will present the experimental results obtained from MOKE. Fig. 7 shows the magnetic hysteresis curves taken by the polar and longitudinal MOKE measurements of the 2.2 ML Fe film on Ag(001) with O_2 adsorption at 100 K. The clean Fe film exhibits only the hysteresis in the polar MOKE with the coercive field H_c of ~100 Oe. The hysteresis looks almost rectangular, and the magnetic easy axis is surface normal. Upon

0.12 L O_2 exposure, the polar MOKE turns to a smoother curve with H_c~40 Oe, and the longitudinal MOKE appears with an almost rectangular shape (H_c~50 Oe). Upon 0.4 L O_2 exposure, no polar MOKE signal was detected and the longitudinal MOKE gives an almost rectangular hysteresis loop with H_c~30 Oe. The magnetic easy axis is in the surface plane, and the SRT was actually reproduced as in the previous work. Oxygen adsorption is confirmed to destabilize the PMA. It is also noted that the coercive fields in both the perpendicular and in-plane magnetization processes are noticeably larger in the mixed region of 0.12 L O_2 exposure than in the perfectly perpendicular or in-plane magnetized

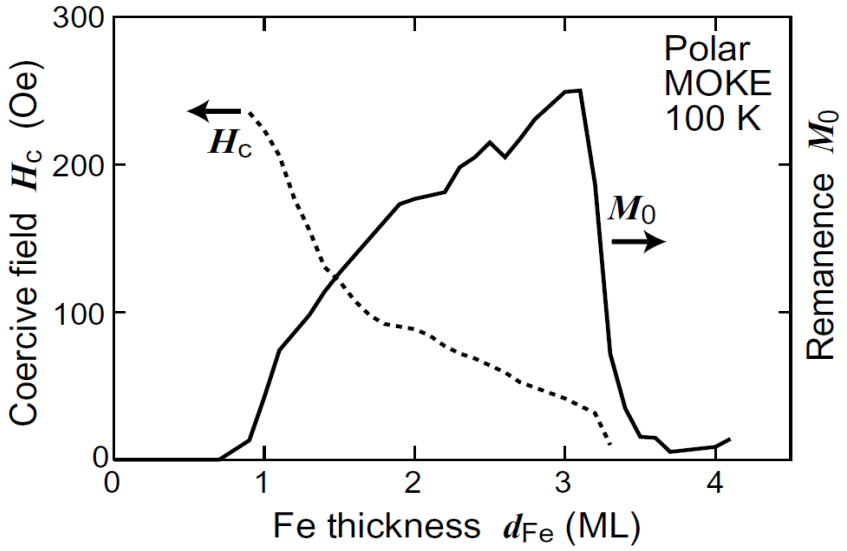

Fig.8 Remanent magnetization and the coercive field of clean Fe films on Ag(0 0 1) taken at 100 K by the polar MOKE measurements. The wedge-shaped Fe film was used.

films with the same thickness.

Before discussing the detailed experimental results on the chemisorption effects, let us pay short attention to the clean Fe films. Fig. 8 shows the Fe thickness dependence of the remanent magnetization and the coercive field recorded by the polar MOKE measurements on the wedge-shaped film at 100 K. As the Fe thickness decreases, the perpendicular remanence appears abruptly around ~3.3 ML to exhibit the PMA. Thicker films than ~3.3 ML give the in-plane magnetic easy axis. In the range of 3.0-1.5 ML, the remanent magnetization is almost proportional to the Fe thickness, exemplifying a

complete PMA feature. At ~1.5 ML, the remanent magnetization drops more rapidly and disappears below ~0.9 ML. This should be caused by the temperature effect; the measurement temperature of 100 K is not sufficiently low compared to the Curie temperature. In Fig. 8, it is also noted that the coercive field is enhanced monotonically with the decrease in the Fe thickness.

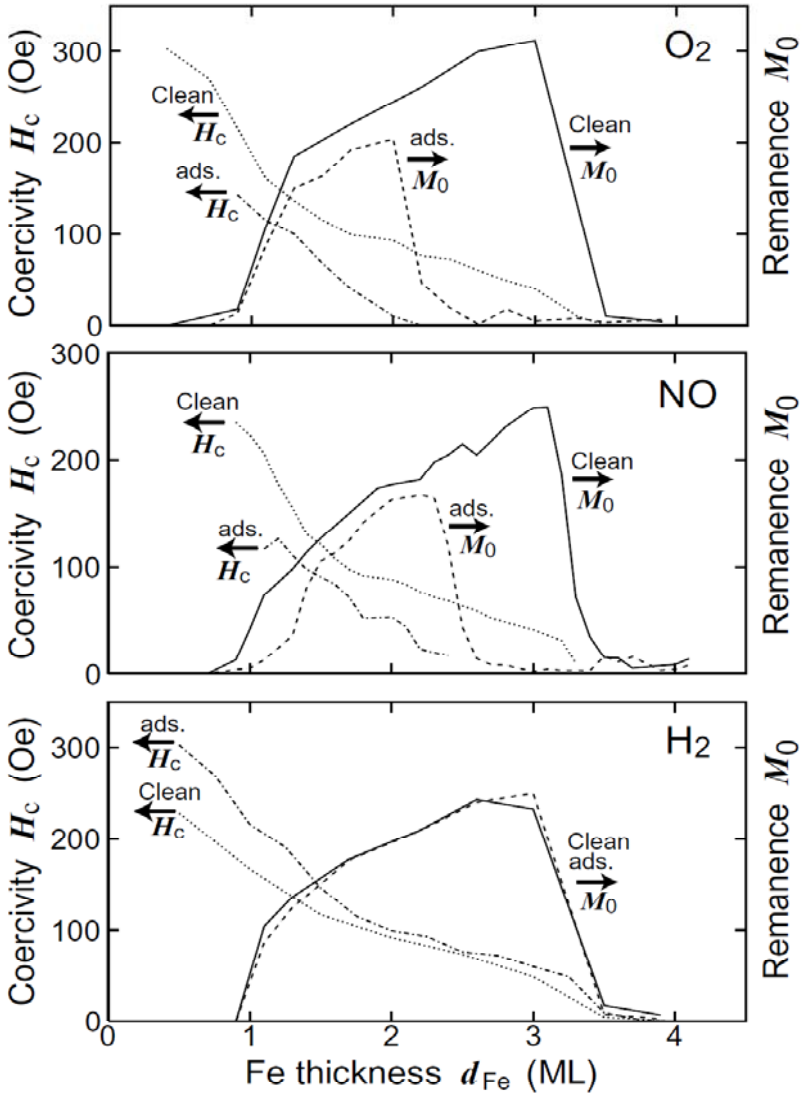

Fig.9 Remanent magnetization and the coercive field of the Fe films on Ag(0 0 1) before and after gas (O_2, NO and H_2) adsorption recorded at 100 K by the polar MOKE measurements. The wedge-shaped Fe film was used.

Fig. 9 shows the Fe thickness dependence of the remanent magnetization and the coercive field before and after gas adsorption obtained by the polar MOKE measurements of the wedge-shaped Fe films at 100 K. In the cases of O_2 and NO adsorption, the critical thickness d_c for the SRT is found to shift to a thinner side: the critical thicknesses of ~3.4, ~2.3 and ~2.5 ML for clean, O- and NO-adsorbed films, respectively. The finding for O_2

adsorption is consistent with the previous work [22]. For these two gases, the coercive fields are found suppressed after adsorption. In contrast, H_2 adsorption shows a different effect on magnetic anisotropy. No critical thickness shift even after 5 L dosage of H_2 is detected. The remanent magnetization is not suppressed, while the coercive field is enhanced. These findings are essentially dissimilar to the O_2 and NO adsorption cases.

4.4 XMCD results

Let us here present the XMCD results in order to clarify microscopic origins of the adsorption induced SRT. Fig. 10 shows the circularly polarized Fe $L_{III,II}$-edge XAS of clean and oxygen-adsorbed Fe films (1.2 ML) on Ag(001), taken at normal X-ray incidence (both the X-ray helicity and the magnetization perpendicular to the surface) at a temperature of 100 K. The quality of the spectra is sufficient. In these spectra, the

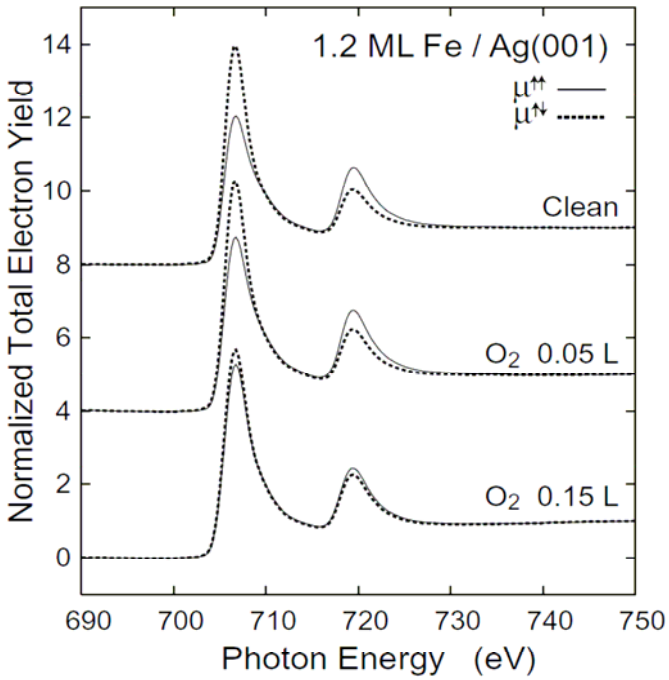

Fig.10 Fe $L_{III,II}$-edge XAS of clean and oxygen-adsorbed Fe (1.2 ML) films on Ag(0 0 1), taken at normal X-ray incidence at 100 K. $\mu^{\uparrow\uparrow}$ ($\mu^{\uparrow\downarrow}$) is the spectrum with the electron spin direction parallel (antiparallel) to the X-ray helicity.

so-called self-absorption effect [28] was taken into account with the assumption that the films are uniformly flat. Although the effect is important for 4.8 ML Fe and negligibly small for 1.2 ML Fe, all the spectra were corrected prior to the XMCD analysis. The experimentally obtained yield spectrum $Y(t)$ (t is the thickness) is given as

$$Y(t) = \frac{C\mu(E)\{1-\exp[-t(1/\lambda_e + 1/\lambda_x(E)\cos\varphi)]\}}{1+\lambda_e/\lambda_x(E)\cos\varphi} \quad ,$$

where λ_e the electron escape depth assumed to be 2.5 nm, $\lambda_x(E)$ the X-ray penetration depth, φ the X-ray incidence angle with respect to the surface normal, C the constant, and $\mu(E)$ the absorption coefficient. $\lambda_x(E)$ is inversely proportional to $\mu(E)$. The absorption coefficients $\mu(E)$ at certain energies below the L_{III} edge (pre-edge baseline) and sufficiently above the L_{II} edge (baseline + edge jump) can be given from the literature table [29] since these values are purely atomic origins and do not depend on the sample state. By solving the equation numerically, the absorption coefficient $\mu(E)$ is eventually determined. In Fig. 10, the absorption spectra normalized with the edge jump are plotted. It is clearly found in Fig. 10 that the white line (peaks at $L_{III,II}$ edges) intensity increases with the oxygen dosage, implying an increase in the 3*d* hole number. The difference between the left- and right-circularly polarized spectra, proportional to the XMCD, correspondingly decreases. This is easily understandable since the Fe film is gradually oxidized with oxygen dosage and this leads to the reduction of the magnetization.

Fig. 11 shows the Fe $L_{III,II}$-edge XMCD for all the samples investigated. The spectra were scaled by factors of the circular polarization (P_c=0.70 in this experiment) and the X-ray incidence angle θ with respect to the magnetization direction ($\cos\theta=\sqrt{3}/2$ for 4.8 ML Fe and $\cos\theta=1$ for Fe 1.2 ML). As expected in Fig. 10, the XMCD intensity noticeably decreases with the oxygen dosage in the 1.2 ML Fe film. O_2 and NO adsorption on 1.2 ML Fe shows similar behaviors, and this is well consistent with the above MOKE results. The XMCD spectrum for hydrogen adsorption on 1.2 ML Fe is, on the other hand, almost identical to the one of clean Fe, which is also consistent with the MOKE result given and implies that the effect of hydrogen adsorption is quite small. In order to obtain the *effective* spin and orbital magnetic moments, m_{spin}^{eff} and m_{orb}, we performed the analysis using well-known sum rules for XMCD [30,31]. Note here that the spin magnetic moments m_{spin}^{eff} is just effective since a small magnetic dipole term m_T is included as

$m_{spin}^{eff} = m_{spin} + 7m_T$.

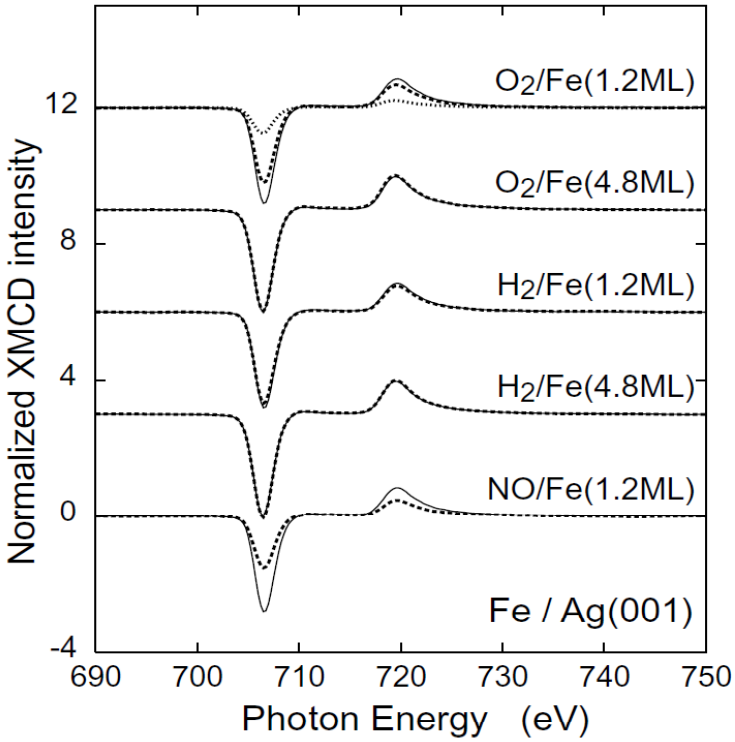

Fig.11 Fe $L_{III,II}$-edge XMCD of clean (solid lines) and adsorbed (dashed and dotted lines) Fe films on Ag(0 0 1), taken at normal X-ray incidence (1.2 ML) and grazing X-ray incidence (4.8 ML) at 100 K. The amounts of gas dosage are as follows: (a) dashed: 0.05 L O_2; dotted: 0.15 L O_2, (b) dashed: 0.15 L O_2, (c) dashed: 1.0 L H_2, (d) dashed: 50 L H_2, and (e) dashed: 0.1 L NO.

Ohresser *et al*. [32] investigated the contribution of the magnetic dipole term compared to the spin magnetic moment in the Fe nanoclusters and ultrathin films on Au(111) by using a 7 T superconducting magnet. They concluded that in the Fe film thicker than 2 ML the magnetic dipole term. In the 1.2 ML Fe films, the ratio of $7m_T/m_{spin}$ is estimated as ~0.1. We should note that the effective spin magnetic moments for the 1.2 ML films investigated here are roughly by 10% overestimated. Table 1 summarizes the results of the analysis. The evaluated 3*d* hole numbers d_{hole} are also given to show the oxidation states. There can be seen several remarkable results in this table. We will first compare the results of the two clean Fe films with the thickness at 1.2 and 4.8 ML. The *d* hole number of the clean 1.2 ML Fe film is 3.73±0.10, which is noticeably larger than the one of the clean 4.8

ML Fe film (d_{hole}=3.40). Moreover, the ratio of the orbital/spin magnetic moments, m_{orb}/m_{spin}^{eff}, is enhanced in a thinner film: m_{orb}/m_{spin}^{eff}=0.075±0.010 for the 1.2 ML Fe

Table1: Results of the Fe spin(m_{spin}^{eff}) and orbital(m_{orb}) magnetic moments of clean and adsorbed Fe films on Ag(001), together with the 3d hole number

Sample			m_{spin}^{eff} (μ_B)	m_{orb}/m_{spin}	d_{hole}
1.2 ML Fe		Clean	2.35(15)	0.075(10)	3.73(10)
	(a)	0.05 L O_2-ads.	1.89(15)	0.052(5)	3.88(10)
		0.15 L O_2-ads.	0.64(10)	0.000(5)	4.22(20)
	(b)	0.1 L NO-ads.	1.34(15)	0.028(3)	3.94(10)
	(c)	1.0 L H_2-ads.	2.22(15)	0.066(5)	3.70(10)
4.8 ML Fe		Clean	2.65(10)	0.036(4)	3.40*
	(d)	0.15 L O_2-ads.	2.71(10)	0.031(3)	3.41(5)
	(e)	50 L H_2-ads.	2.71(10)	0.034(3)	3.40(5)

Errors given in parentheses are effective for the last digit. The value of d_{hole} in clean 4.8 ML Fe indicated by an asterisk was assumed as a reference to obtain d_{hole} for the other samples

and m_{orb}/m_{spin}^{eff}=0.036± 0.004 for the 4.8 ML Fe. The spin magnetic moment of the clean 1.2 ML Fe film is, on the contrary, 2.35±0.15 μ_B, which is smaller than the one of the clean 4.8 ML Fe film (m_{orb}/m_{spin}^{eff}=2.65±0.10 μ_B).

The effects of O_2 and NO adsorption are quite similar to each other. The spin magnetic moments are reduced, while the *d* hole number increases. More interestingly, the ratios of the orbital/spin magnetic moments, m_{orb}/m_{spin}^{eff}, are also suppressed. This implies that the orbital magnetic moment is quenched more rapidly than the spin magnetic moment. On the other hand, the effect of H_2 adsorption is again found to be quite small when one compares the spin magnetic moment and the ratio of the orbital/spin magnetic moments. moments are reduced, while the *d* hole number increases. More interestingly, the ratios of the orbital/spin magnetic moments, m_{orb}/m_{spin}, are also suppressed. This implies that the orbital magnetic moment is quenched more rapidly than the spin magnetic moment. On the other hand, the effect of H_2 adsorption is again found to be quite small when one compares the spin magnetic moment and the ratio of the orbital/spin magnetic

moments.

4.5 Discussion

(a) *Clean Fe films*

Let us first discuss the results of the clean Fe films on Ag(001) obtained by the MOKE and XMCD measurements. As seen in Fig.8, the remanent magnetization along the perpendicular direction was found to be proportional to the Fe thickness over the thickness range of 1.5-3.0 ML. This implies that the Fe magnetic moment does not differ depending on the Fe thickness. The spin magnetic moment of 1.2 ML Fe given by XMCD was found to be smaller than that of 4.8 ML Fe. This is due to the temperature effect as seen in Fig. 8. The effective spin magnetic moment of 4.8 ML Fe (m_{spin}^{eff} =2.65±0.10 μ_B) might be nevertheless enhanced compared to the bulk value of ~2.32.4 μ_B, although a definite conclusion cannot be given because of the difficulties of the employment of the spin sum rule in the XMCD analysis. On the other hand, it can be concluded that the *d* hole number and the ratio of the orbital/spin magnetic moments are enhanced in a thinner film. Although there seems to be no direct information on the enhancement of the orbital magnetic moment in Fe/Ag(001) even in theoretical works, this finding is in good accordance with the Co thin films [17,33-35].

In the thickness dependence of the coercive field shown in Fig. 8, we found that the thinner the film is, the larger the coercive field is. There are many reasons for the enhancement of the coercive field. One possible reason is the enhancement of the PMA. In the magnetization reversal process of the present system, the domain nucleation may at first occur, and subsequently the domain wall movement may take place. As seen in Fig. 7, the magnetization hysteresis curve is of almost rectangular shape, implying that the domain wall movement takes place immediately after the domain nucleation and that the domain nucleation is important to determine the coercive field. The domain wall formed in the perpendicular magnetization reversal process is a Bloch type. The in-plane magnetic moment in the domain wall is energetically unfavorable because of the PMA film. The

nucleation of reversed domains thus requires the activation energy, with which the barrier related to the magnetic anisotropy can be overcome. In the present system, the surface anisotropy favors the PMA, implying that the PMA is stronger in a thinner film. Since the coercive field corresponds to the activation energy for the magnetization reversal, it should be enhanced in a thinner film. Although this reason may be most probable, the other possible factors such as morphology might not be ruled out. Since the thicker film is the flatter, the domain wall moves more freely in thicker films, yielding a smaller coercive field.

(b) *Effects of chemsorption on magnetic anisotropy*

Chen *et al*. [22] clarified that adsorption of O_2 on the Fe film on Ag(001) destabilizes the PMA. This may be an unique example since all the other films lead to the stabilization of the PMA on adsorption: H_2 and CO on Ni/Cu(001) [17,18], CO on Co/Pd(111) [17], Cu on Ni/Cu(001) [26,36] and so forth. This is because all the latter systems give negative surface magnetic anisotropies that favor the in-plane magnetization and are weakened on adsorption on the surface. On the other hand, the present Fe/Ag(001) system has a positive surface anisotropy [22], which is similarly suppressed on gas adsorption. In the cases of O_2 and NO adsorption on Fe/Ag(001), the surface anisotropy is reduced, leading to the destabilization of the PMA, while in the case of H_2 the interaction is too weak to shift the critical thickness.

Chen *et al* also studied the microscopic origin for the destabilization of the PMA in O_2 adsorption (order is changed). They observed the sharpening of the LEED spot after O_2 adsorption and speculated that the surface roughness of the Fe film is noticeably reduced by O_2 adsorption. Although the flattening of the film may induce the destabilization of the PMA, they supposed that the destabilization of the PMA originates from the changes of the spin-orbit interaction, but no information on the orbital magnetic moment was given. This is partly the reason why we have reinvestigated the effect of O_2 adsorption by means of the XMCD, which yields the orbital magnetic moment directly. Actually, we found that the perpendicular orbital magnetic moment is quenched more significantly than the perpendicular spin magnetic moment upon O_2 and NO adsorption. We can conclude that the quenching of the perpendicular orbital magnetic moment plays a key role for the

destabilization of the PMA.

In the present study, it was found to be difficult to derive the difference of the orbital magnetic moment between the perpendicular and in-plane directions, which is essentially important to discuss the magnetic anisotropy in terms of the spin-orbit interaction [37]. In our previous works on Co/Pd(111) [17] and Ni/Cu(001) [17,26], we have determined both the perpendicular and in-plane orbital magnetic moments by measuring thin and thick films separately. Although we have done the same measurements for the 1.2 and 4.8 ML films here, the difference of the spectral features of the 4.8 ML film is too small to discuss the orbital magnetic moment, partly because Fe has inherently a smaller orbital moment than Co or Ni. In order to compare the magnetic anisotropy with the orbital magnetic moment directly, the measurement under a strong magnetic field using a superconducting magnet is required.

Nevertheless, we have successfully observed significant reduction of the orbital magnetic moment in the 1.2 ML Fe film. An illustration regarding the variation of orbital moment with different adsorption (comparison was deleted) geometry is given here for better understanding. In the case of CO adsorption on Co/Pd(111) and Ni/Cu(001), as shown in Fig. 12(b), it was found that the perpendicular orbital magnetic moments do not change so much upon gas adsorption. This is in clear contrast to the present system and is the reason for the different behaviors of the stabilization or destabilization of the PMA. This should be ascribed to a different geometric configuration during gas adsorption. In the previous systems, CO adsorbs with the molecular axis perpendicular to the surface. This geometry interrupts the in-plane orbital magnetic moment more efficiently than the perpendicular moment since the perpendicular orbital magnetic moment originates from the electron rotation within the surface plane, which interacts with the adsorbate less strongly compared to the electron motion out of the surface plane. In the present case, however, the gas atom displays a geometric configuration that easily generates lateral interaction between adsorbents and Fe atoms, This lateral interaction tends to hamper the electron rotation within the surface that favors PMA. A sketch of adsorption model is given in Fig.12 (c). Oxygen atom is usually located at the fourfold hollow site on the topmost Fe layer [22] but is noticeably embedded in the first Fe layer in the current case

because *bcc* Fe(001) has a larger unit cell than *fcc* Co(111) or *fcc* Ni(001). The lateral interaction between the adsorbents and substrate thus becomes important and consequently the perpendicular orbital magnetic moment is efficiently quenched.

In NO adsorption on Fe, Suzuki *et al.* [38] claimed that the NO molecular axis was highly tilted or even lying-down on the Fe surface by comparing with NO adsorption on Ni(001) [39]. Another support for this structure model is the existence of similar molecular axis tilting or lying-down observed in CO adsorption on Fe (001) surface [40,41]. This configuration of NO may induce strong lateral interaction and therefore suppress the in-plane electron motion that contributes to the perpendicular magnetic orbital moment. In contrast to O_2 and NO, H_2 shows almost no effect on the shift of critical thickness. This is due to a fact that the tiny hydrogen atom is always located on the top of the second Fe layer, which brings negligible lateral interaction with topmost Fe atoms.

(*see the next page*)

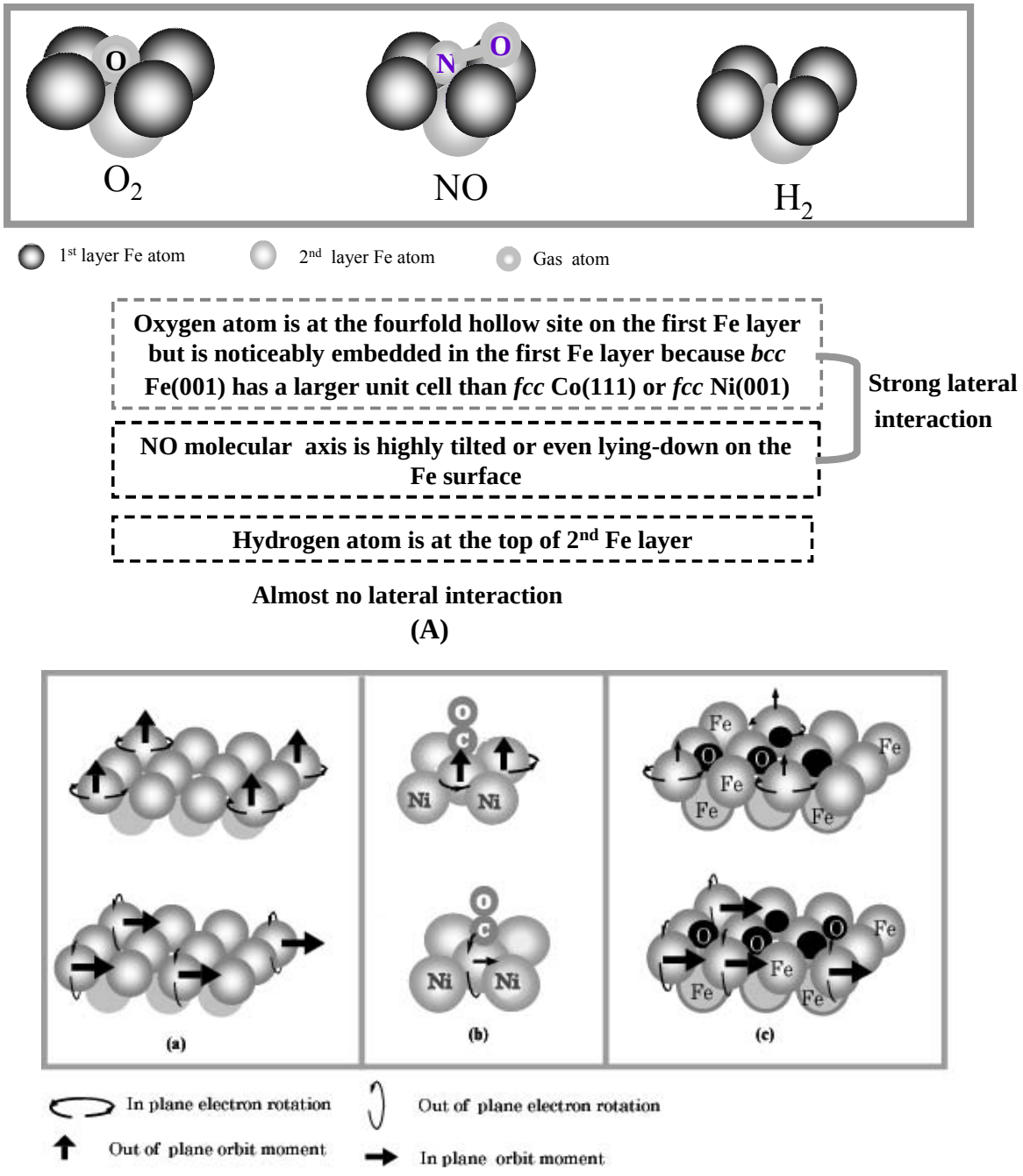

Fig. 12. (A): Adsorption geometries for three gases; (B): Comparison of the variation of the out-of-plane and in-plane orbital moments with different adsorption geometries: (a) bcc(001) clean surface, (b)atop site adsorption for CO/Ni/Cu(001) and (c) fourfold hollow site adsorption for O/Fe/Ag(001). Thin rounded arrows represent the rotational motions of 3d electrons, while thick straight arrows the orbital magnetic moments.

Finally, we will shortly discuss the changes of the coercive field upon gas adsorption. As shown in Fig. 8, we found that O_2 and NO adsorption suppresses the coercive field of the Fe film as well as the magnetization, while H_2 adsorption enhances the coercive field leaving the magnetization unchanged. The enhancement of the coercive field along the surface normal direction may often be associated with the stabilization of the

perpendicular magnetic anisotropy. In the present case of H_2 adsorption, however, the critical thickness for the SRT does not change at all (see Fig. 8), implying no effect on the magnetic anisotropy. This may be caused by the other origin such as a pinning effect for the domain wall movement.

Conclusion:

We have investigated the effect of surface chemsiorption on the spin reorientation transitions in magnetic ultrathin Fe films on Ag(001) by means of the polar and longitudinal MOKE and XMCD measurements. It was found that adsorption of NO destabilizes the perpendicular magnetic anisotropy, as in the case of O_2 adsorption, while H_2 adsorption does not modify the magnetic anisotropy. Although both the spin and orbital magnetic moments

along the surface normal are noticeably reduced upon O_2 and NO adsorption, the reduction of the perpendicular orbital magnetic moments are more significant, indicating that the destabilization of the perpendicular magnetic anisotropy upon chemisorption of O_2 and NO originates from the change of the spin-orbit interaction at the surface. These findings are in good contrast to the systems of CO adsorption on Ni/Cu(001) and Co/Pd(111), which show the stabilization of the perpendicular magnetic anisotropy and the corresponding reduction of the in-plane orbital magnetic moment. This fact is attributed to a different adsorption behavior during gas adsorption. The O atom is embedded in the top layer of Fe, and the NO molecule is lying down on the surface, while CO on Ni/Cu(001) and Co/Pd(111) is standing up on the surface.

References

[1] C.S. Wang and A.J. Freeman, Phys. Rev. B 24, 4364 (1981),.

[2] S. Ohnishi, M. Weinert and A.J. Freeman, Phys. Rev. B 30, 36 (1984),.

[3] C.L. Fu, A.J. Freeman and T. Oguchi, Phys. Rev. Lett. 54, 2700. (1985)

[4] R. Richter, J.G. Gay and J.R. Smith, Phys. Rev. Lett. 54, 2704 (1985)

[5] C.L. Wooten, J. Chen, et al, Phys. Rev. B 49. 10023 (1994)

[6] J.A.C. Bland, C. Daboo, et al, Phys. Rev. B 51, 258 (1995),.

[7] J.G. Gay and R. Richer, J. Appl. Phys. 61, 3362. (1987).

[8] C. Li, A.J. Freeman, H.J.F. Jansen and C.L. Fu, Phys. Rev. B 42, 5433 (1990).

[9] B. Heinrich, K.B. Urquhart, et al, Phys. Rev. Lett. 59, 1756 (1987)

[10] N.C. Koon, B.T. Jonker, et al, Phys. Rev. Lett. 59, 2463 (1987)

[11] M. Stampanoni, A. Vaterlans, et al Phys. Rev. Lett. 59, 2483 (1987)

[12] J. Araya-Pochet, C.A. Ballentine and J.L. Erskine, Phys. Rev. B 38, 7846 (1988).

[13] Z.Q. Qiu, J. Pearson and S.D. Bader, Phys. Rev. Lett. 70, 1006 (1993)

[14] A. Berger and H. Hopster, Phys. Rev. Lett. 76, 519 (1996), p.

[15] D.M. Schaller, D.E. Burgler, et al, Phys. Rev. B 59 ,14516 (1999)

[16] H. Van Vleck, Phys. Rev. 52, 1178. (1937)

[17] D. Matsumura, T. Yokoyama, et al, Phys. Rev. B 66,024402(2002)

[18] R. Vollmer, Th. Gutjahr-Löser, et al, Phys. Rev. B 60, 6277 (1999)

[19] S. Hope, E. Gu, B. Choi and J.A.C. Bland, Phys. Rev. Lett. 80, 1750 (1998).

[20] S. Hope, E. Gu, B. Choi and J.A.C. Bland, Phys. Rev. B 57, 7454 (1998)

[21] H.J. Elmer, J. Hauschild et al, J. Magn. Magn. Mater. 198–199, 222.(1999)

[22] J. Chen, M. Drakaki and J.L. Erskine, Phys. Rev. B 45, 3636 (1992)

[23] Š. Pick and H. Dreyssé, Phys. Rev. B 63, 205427 (2001)

[24] S.R. Chub and W.E. Pickett, Phys. Rev. Lett. 58,1248 (1987)

[25] W.F. Egelhoff Jr. and I. Jacob, Phys. Rev. Lett. 62, 921 (1989)

[26] T. Nakagawa, H. Watanabe and T. Yokoyama, Phys. Rev. B 71,235403 (2005)

[27] T. Gejo, Y. Takata, et al, Chem. Phys. 289,15 (2003)

[28] R. Nakajima, J. Stöhr and Y.U. Idzerda, Phys. Rev. B 59, 6421 (1999)

[29] B.L. Henke, E.M. Gullikson et al, Atom. Data and Nucl. Data Table. 54,181 (1993)

[30] B. Thole, P. Carra, F. Sette and G.V. der Laan, Phys. Rev. Lett. 68, 1943 (1992)

[31] P. Carra, B. Thole, M. Altarelli and X. Wang, Phys. Rev. Lett. 70,694 (1993)

[32] P. Ohresser, N.B. Brookes, et al, Phys. Rev. B 64, 104429 (2001)

[33] M. Tischer, O. Hjortstam, D. Arvanitis, et al, Phys. Rev. Lett. 75,1602 (1995)

[34] N. Nakajima, T. Koide, et al, Phys. Rev. Lett. 81, 5229 (1998)

[35] T. Koide, H. Miyauchi, et al, Phys. Rev. Lett. 87, 257201 (2001)

[36] W.L. O'Brien and B.P. Tonner, Phys. Rev. B 49, 15370 (1994)

[37] P. Bruno, Phys. Rev. B 39 R865 (1989)

[38] T. Suzuki, M. Kurahashi and Y. Yamauchi, Surf. Sci. ,181507–510 (2002)

[39] A. Sandell, A. Nilsson and N. Mårtensson, Surf. Sci. Lett. 241, L1 (1991)

[40] D.W. Moon, S. Cameron, F. Zaera, et al, Surf. Sci. 180, L123 (1987).

[41] R.S. Saiki, G.S. Herman, M. Yamada, et al, Phys. Rev. Lett. 63,283 (1989)

Electronic states and local structures of the photomagnetic Cu-Mo cyanides $Cu_2Mo(CN)_8 \cdot 8H_2O$ and $Cs_{0.5}Cu_{1.75}Mo(CN)_8 \cdot 1.5H_2O$ studied by x-ray absorption fine structure spectroscopy

X-D Ma, T.Yokoyama, T. Hozumi, K. Hashimoto and S. Ohkoshi

***Phisical Review* B 72**, 094107 (2005)

5.1 General introduction:

Prussian blue bimetallic analogs often exhibit noble magnetic properties such as photoinduced magnetization with high Curie temperature [1-5]. The reversible modification upon light irradiation confirmed so far on these materials makes them a type of very promising molecular magnet used for new writing/erasing devices. The photoinduced magnetization in these bimetallic compounds involves a charge transfer from metal to metal which causes a change in both metal spin states during light irradiation and thus the magnetic property is modified. A metal to metal charge transfer band in the optical spectrum is possibly developed when both metal centers have oxidation state flexibility with close redox potentials and thus an internal photo-redox process may occur under appropriate light irradiation. The first photoinduced phase transition in CoFe cyanides by optical stimuli was reported by Sato[3]*et al*, where the compounds show weak paramagnetism at low temperature (LT), and they become ferrimagnets upon visible light (500-750nm) irradiation.

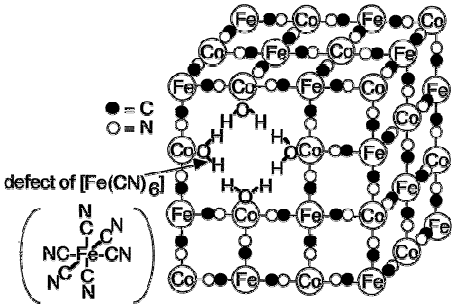

Fig,1 Unit cell of cobalt-iron cyanide. Certain $Fe(CN)_6$ sites are vacant, and the bridging oxygen of H_2O fills the empty nitrogen end. Interstitial alkali metal cations have been omitted for clarity

Furthermore the ordered ferromagnetic state undergoes a reversed transition to initial paramagnetic LT state after irradiation from a near-infrared light

(1319nm) source. Structure information during photon induced magnetization process is indispensable to disclose the nature of the photomagnetic behavior in detail.

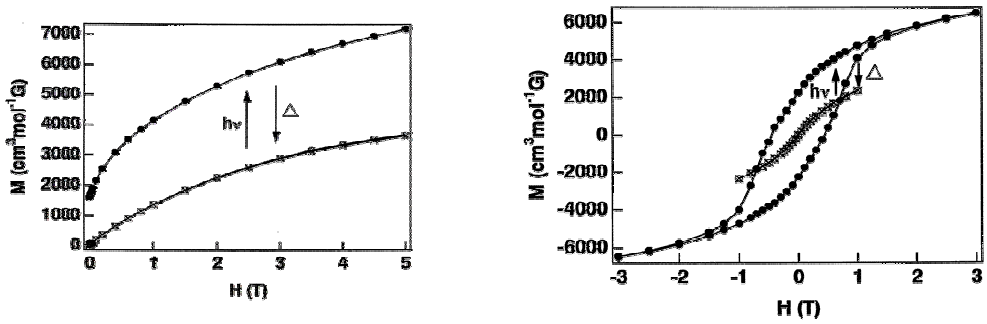

Fig.2 right: Field dependence of the magnetizations for $Rb_{0.66}Co_{1.25}[Fe(CN)_6]\cdot 4.3H_2O$ before and after light illumination ($h\nu$) at 2 K. left: Hysteresis loops for $Rb_{0.66}Co_{1.25}[Fe(CN)_6]\cdot 4.3H_2O$ at 2 K. ○, before light illumination; ·, after light illumination; × after thermal treatment at 150 K. (○ and × fall on the same line.) △represents thermal treatment.

However the conventional structure analysis such as single crystal XRD is hardly applicable to these Prussian blue analogs since the sample usually can only be prepared as fine powder. In this case, extended x-ray absorption fine structure (EXAFS) spectroscopy is useful to obtain local structures around metal atoms. It can allow us to obtain information on coordination numbers and interatomic distance around the x-ray absorbed atoms. Meanwhile electronic property can be revealed meanwhile by the measurements of x-ray absorption near edge structure (XANES) spectra. The x-ray absorption fine-structure (XAFS) studies on photomagnetic Prussian-blue analogs have been performed for CoFe [6–8] CoW [9] and MnFe [10] cyanides.

In the present study we have measured and analyzed Cu and Mo *K*-edge XAFS(x-ray-absorption fine-structure) spectra taken before and after

photoirradiation for two new CuMo cyanides: $Cu_2Mo(CN)_8 \cdot 8H_2O$ [15] (No**1**hereafter) and $Cs_{0.5}Cu_{1.75}Mo(CN)_8 \cdot 1.5H2O$ [8] (No**2** hereafter).

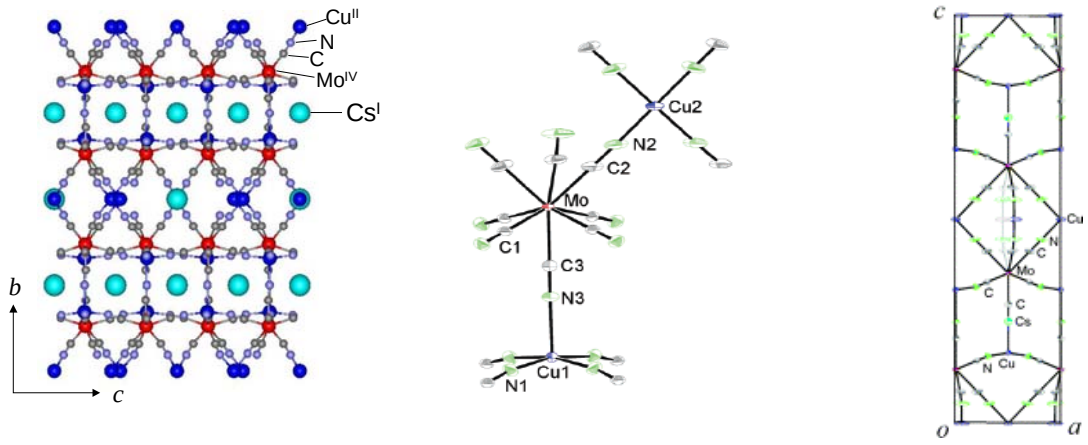

Fig.3 (a) Three-dimensional crystal structure using polyhedral model. Pink, blue, and light-blue polyhedron show MoC_8, $Cu1N_5$, and $Cu2N_4$, respectively. Water molecules and cesium atoms are omitted for clarity. (b) ORTEP drawing of the coordination environments around Cu and Mo. Blue, red, gray, and yellow-green ellipsoids represent Cu, Mo, C, and N, respectively. Displacement ellipsoids are drawn at a 50% probability level. Cu2, C2, and N2 atoms are disordered, and only selected atoms are drawn for clarity. (c) ORTEP drawing of the unit cell. Blue, red, light-blue, gray, and yellow-green ellipsoids represent Cu, Mo, Cs, C, and N, respectively. Displacement ellipsoids are drawn at a 50% probability level. Water molecules are omitted for clarity.

CuMo cyanides have also been attractive photomagnets. $Cu_2Mo(CN)_8 \cdot 8H_2O$ undergoes a photoinduced phase transition at low temperature (LT) with a Curie temperature of 17 K [11–14]. Fig.3 and Fig.4 show the crystal structural of the two cyanide samples. X-ray analysis reveals that there are two Cu sites (Cu1 and Cu2) in sample No2. Cu1 site has square pyramid coordination geometry and is coordinated to five CN ligands which includes four equatorial Cu1-N bonds and one axial Cu1-N bond. On the other hand, Cu2 site is coordinated by four CN ligands and has a square planar geometry.

For sample No1, although no single crystal structural information has been obtained so far, a coordination geometry in which Cu site has an octahedral coordination sphere with four square planar Cu-N bonds and two axial Cu-O bonds has been proposed.

The investigation on these samples is extremely important for the following reasons. First, the photoinduced phase is an essentially different state for these compounds. Usually, the photoinduced phase at low temperature (LT) is considered to be structurally identical to that of the corresponding high-temperature (HT) phase. The CuMo cyanides are, however, in the LT phase even at room temperature and are likely to decompose with the temperature rise before the thermally driven phase transition takes place. Second, these compounds, which show ferromagnetism, consist only of magnetic ions of Cu and Mo, which seldom exhibit ordered magnetism. No typical magnetic ions such as Mn, Fe, Co, or Ni are present. Third, the change of local structures around Cu in a redox cycle is an important issue in various scientific fields such as catalysis and biology. In the CuMo cyanides, a reduction of Cu from divalent to monovalent is expected on the photoirradiation

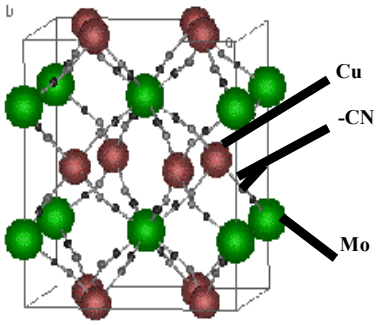

Fig.4 Schematic illustration of $Cu_2Mo(CN)_8 \cdot 8H_2O$ crystal

as in the previous cases of the CoFe, CoW, and MnFe cyanides. In the previous examples, however, significant changes in the interatomic distances occurred. On the contrary, only a slight or negligible change in the interatomic distance is expected in the reduction of Cu. Instead, there have been several known structural models, although in some materials there still remains controversy. In divalent Cu, square planar coordination with four ligands is usually most stable, while in monovalent Cu, trigonal pyramid with three ligands, tetrahedron with four ligands, and square pyramid with five ligands are known. The changes of the local structure around Cu is thus interesting also in the present CuMo cyanides.

5.2. EXPERIMENTS

1 sample preparation:

Samples1 and 2 were synthesized as the following procedure [15]:

The target material was electrochemically prepared by reducing a 30 cm^3 mixed aqueous solution of $Cu^{II}(NO_3)_2 \cdot 3H_2O$ (36 mg, 0.15 mmol) and $Cs_3[Mo^V(CN)_8] \cdot 2H_2O$ (55 mg, 0.075 mmol) in a standard three-electrode cell at a constant potential condition of +500 mV vs Ag/AgCl electrode using a Hokuto-Denko HSV-100 potentiostat. The electrolytic aqueous solutions were adjusted to pH 3 with HNO_3. After 3 days, a single crystal of the compound was obtained on a Pt wire electrode (0.5 mm Φ). A film-type of material was prepared on a SnO_2 (20 Ω/square)-coated glass with a loaded electrical capacity of 45-605 mC. Elemental analyses by an inductively coupled plasma mass spectroscopy (ICP-MS) and standard microanalytical methods confirmed that the formula of

the single crystal was $Cs^{I}_{2}Cu^{II}_{7}[Mo^{IV}(CN)_8]_4 \cdot 6H_2O$ (No2). Calculated: Cs, 13.1; Cu, 21.9; Mo, 18.9; C, 18.9; N, 22.0%. Found: Cs, 12.3; Cu, 22.0; Mo, 18.4; C, 19.0; N, 21.5%. The formula of the film was consistent with that of the single crystal. Found: Cs, 12.4; Cu, 21.8; Mo, 18.4; C, 18.9; N, 21.3%

Fig.5 Right: Photograph of electrochemically synthesized thin film; Left: SEM image of the cross-section of the film.

$Cu_2Mo(CN)_8 \cdot 8H_2O$(No1) was prepared following the same procedure. As reference sample, $Cu(cyclam)_2Mo(CN)_8) \cdot 10H_2O$ (No3) and $Cs_3Mo(CN)_8 \cdot 2H_2O$(No4) were also prepared.

XAFS measurement:

The XAFS measurements were performed at Beamlines 10B and 12C of the Photon Factory at High Energy Accelerator Research Organization (KEK-PF, Tsukuba, Japan). The storage ring was operated with the electron energy of 2.5 GeV and the ring current of 400–250 mA. At Beamline 10B, transmission XAFS spectra were taken for Cu and Mo *K* edges of No 1,2, and 3 at 30 K. Mo *K*-edge XAFS spectra of (No4) were also recorded. A Si(311) channel-cut crystal monochromator was employed. Higher-order harmonics were less important in the operation of the ring energy of 2.5 GeV. Incident I_0 and transmitted I x-ray intensities were simultaneously measured with ionization chambers lengths of 17

cm for *I*0 and 31 cm for *I* filled with appropriate gases: N2 100% (I_0) and N2 50%/Ar 50% (*I*) for the Cu *K* edge and N2 50%/Ar 50% (I_0) and Ar 100% (*I*) for the Mo *K* edge.

At Beamline 12C, fluorescence XAFS spectra were taken for 1 and 2 at 30 K. Fluorescence detection was essential to measure XAFS of the photoinduced phase because the penetration depth of the visible light is much smaller than that of the x rays and the appropriate thickness of the sample is too thin to record transmission XAFS spectra. A thin film of 2 was used as it was. On the other hand, sample 1 was obtained as a fine powder, and a thin film was produced by dispersing powder on an adhesive tape uniformly so as to make it as transparent as possible. A Si (111) double crystal monochromator was employed and detuned slightly (80%) in order to reduce higher-order harmonics. The incident x-ray intensity (I_0) was measured with an ionization chamber filled with N_2 100% for the Cu *K* edge and N_2 50%/Ar 50% for the Mo *K* edge. The fluorescence x-ray intensity was also detected with an ionization chamber filled with Ar for both edges. In order to record the XAFS spectra of the photoinduced phases, the samples were irradiated by blue light from a solid state laser 473 nm for 30–60 min. During the laser irradiation, continuous XANES measurements were performed.

5.3 X-ray adorption near edge spectra(XANES) RESULTS

Figure 1 a shows the Cu *K*-edge XANES of No1 and No2 before and after photoirradiation, together with the reference spectra of CuO and Cu_2O. As illustrated in the reference spectra, monovalent Cu shows a typical resonance

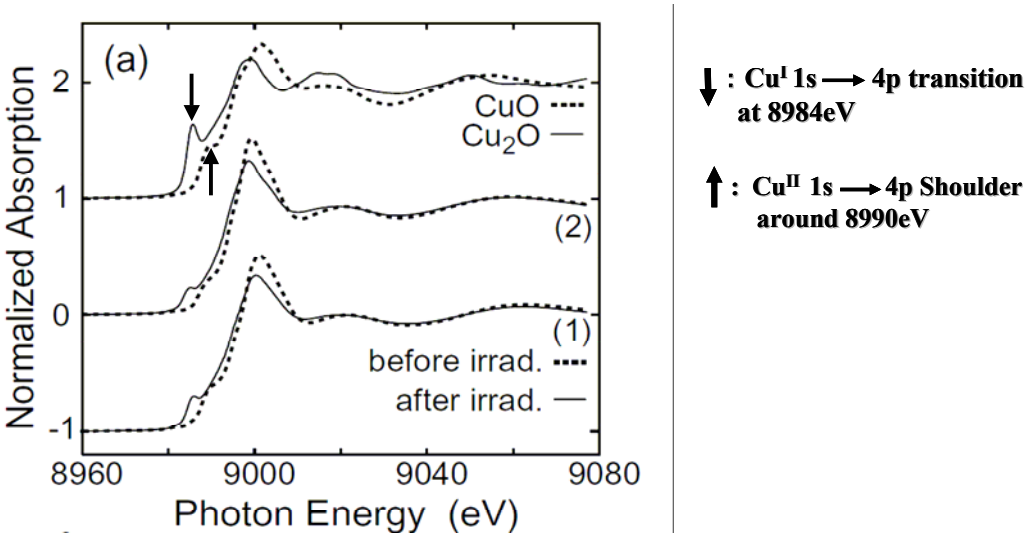

Fig.6 Cu K-edge XANES of No.1, (bottom) No2 (middle) together

peak at 8984 eV, while divalent Cu gives a weak $1s \rightarrow 3d$ absorption at 8981 eV and a shoulder at 8990 eV. One can immediately conclude that Cu^{II} in 1 and 2 is reduced to Cu^{I} after photoirradiation. This is the first direct proof that the charge transfer actually occurs in the photoinduced phase transition of the CuMo cyanide. Figure 6 (b) gives the time evolution of Cu *K*-edge XANES of 2 during photoirradiation. It shows that the typical shoulder for Cu^{II} is apparently weakened, while the one for Cu^{I} is increased during irradiation. It is noted that when the intensities of the peaks at 8984 and 8990 eV are plotted logarithmically, linear kinetics of the present photoreaction is suggested (shown in **C**) and the saturation of the reaction was also confirmed.

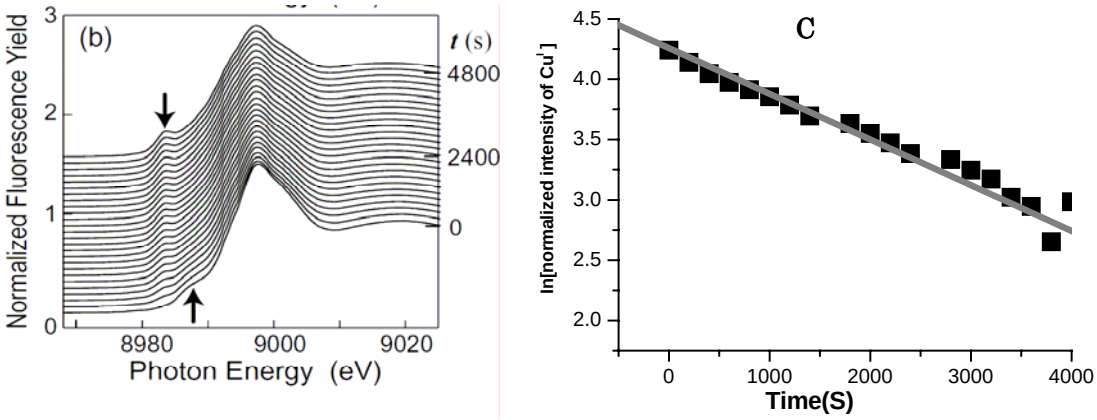

Fig.6 Right: Time evolution of Cu *K*-edge XANES of sample (2) during laser irradiation.

The mechanism of photo-magnetization

From the electronic state information derived from XANES, we can go further to address the mechanism of the photoinduced magnetization in the CuMo cyanides [11]. From the analogy of the potential surfaces of $Cu^{II}/[Mo^{IV}(CN)_8]^{4-}$ in the solution state, those of the solid compound No**1** could be schematically shown as Fig.7. The compound No**1** in the initial state (state I) is paramagnetic. By the irradiation, the compound No**1** is excited to the charge transfer state (state II). The compoundNo**1** in the state II immediately relaxes to the initial state (state I) or forms the mixed-valence isomer (Mo^{V}–CN–Cu^{I}) (state III). In this valence isomer state, Mo^{V} ion ($4d^1$, S=1/2) has unpaired electrons but Cu^{I} ion ($3d^9$, S=0) does not have unpaired electron. However, half of the copper ions should remain as Cu^{II} ion due to the stoichiometric limitation in the present compound. Therefore, the irradiated compound (No**1**) will be expressed as $Cu^{I}Cu^{II}[Mo^{V}(CN)_8]\cdot 7.6H_2O$ (**1′**). Because the magnetic coupling between unpaired electrons on Cu^{II} and those on Mo^{V} ions in the reference sample **2** is

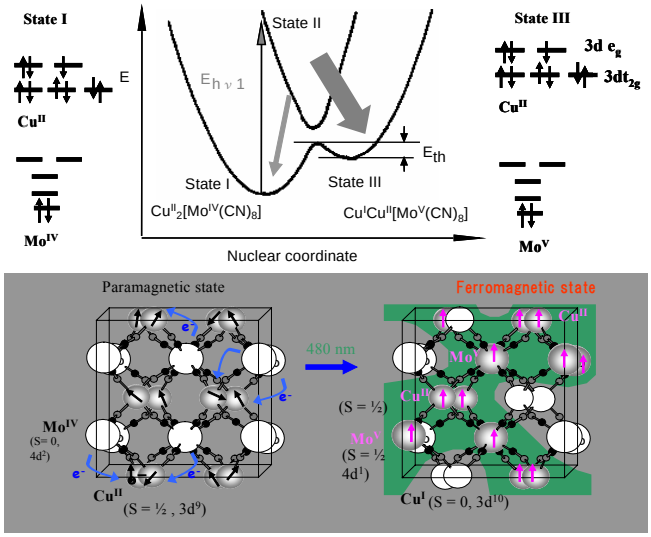

Fig. 7. (top) Potential energy diagrams in the solid state of $Cu_2^{II}[Mo^{IV}(CN)_8]\cdot 7.6H_2O$ mixed-valence compound; (bottom) schematic illustration of magnetic coupling in the solid state of $Cu_2^{II}[Mo^{IV}(CN)_8]\cdot zH_2O$ by the irradiation.

ferromagnetic, the unpaired electrons on Mo^V (S=1/2) ions and those on Cu^{II} (S=1/2) ions of **1′** are expected to interact ferromagnetically. The possible mechanism of the spin alignment is schematically shown in Fig.7(bottom). The ferromagnetic coupling can be understood based on a model in terms of a superexchange mechanism through the cyanide ligands. The superexchange mechanism is summarized on the basis of the Goodenough-Kanamori rule [16–18] which includes consideration of the symmetry of the metal and ligand orbital concerned and the bond angle. There are two mechanisms for superexchange interactions: Kinetic exchange J_{KE} is mediated by a direct pathway of the overlapping orbitals, It is antiferromagnetic in nature as a consequence of the Pauli principle, leading to an antiparallel spin ordering via a

common covalent bond. While potential exchange is effective between orthogonal magnetic orbitals with comparable orbital energy. In this case Hund's rule leads to a parallel spin alignment, i.e., a ferromagnetic interaction. Prussian blue analogs, the metal *d* orbitals are split into t_{2g} and e_g sets by the CN ligands. Therefore, based on magnetic orbital symmetry, we can understand whether the superexchange interaction among metals ions is J_{KE} or J_{PE} . When

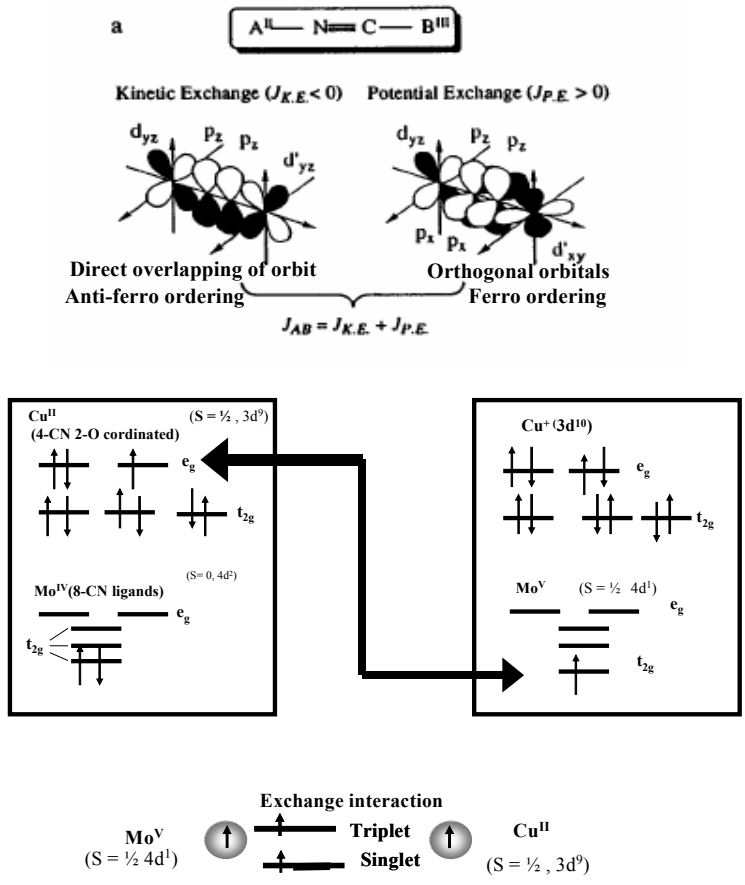

Fig.8 Model of exchange coupling between two CN-bridged magnetic ions (Cu^{II} and Mo^{V})

the magnetic orbital symmetries of the metals are the same, the superexchange interaction is J_{KE} . Conversely, when the magnetic orbital symmetries of the

metals are different, the superexchange interaction is J_{PE}. In the current case, the superexchange interaction is apparently J_{PE} dominated resulting in ferromagnetic ordering.

5.4 Structure from extended X-ray absorption fine structure (EXAFS)

Fig.9 shows the Mo and Cu *K*-edge EXAFS oscillation Functions $k^3\chi(k)$ and their Fourier transforms FT of (No1–4) taken in the transmission mode. The EXAFS functions were obtained by standard procedures as the subtraction of the preedge baseline and the postedge background (cubic spline functions), followed by normalization using the atomic absorption coefficients. For assignments of the features in the FTs, let us briefly summarize structural information reported previously[14–16,19]. In all samples of (No1–4), there exist $Mo(CN)_8$ units, and in samples (1–3) the $Mo(CN)_8^{4-}$ unit is linked to Cu. In (1) [14], Cu is surrounded by four equatorial NC^- and two axial H_2O. On the other hand, in (2)[15], there exist two inequivalent Cu with the composition ratio of

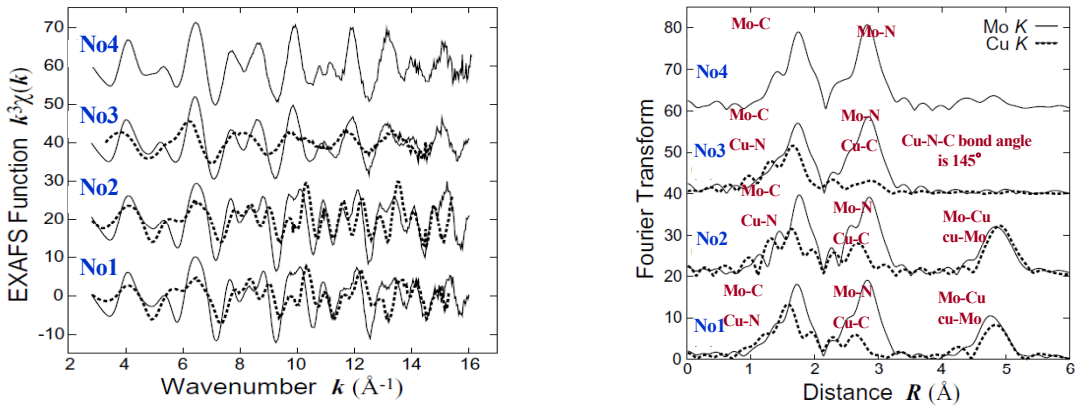

Fig.9 (Right) Mo and Cu K-edge EXAFS Oscillation functions $k^3\chi(k)$ and (left) their corresponding Fourie transforms

Cu1:Cu2=4:3. Cu1 shows square pyramidal coordination consisting of four equatorial and one axial NC−, while Cu2 exhibits similar structure to that in sample(1).

In all of the FTs of the Mo *K*-edge EXAFS, contributions of the Mo-C (~1.7 Å) and Mo-N (~2.9 Å) shells are clearly seen, while in the FTs of 1 and 2, additional contributions are found at ~4.8 Å, which can be assigned to the Mo-Cu shell. The fact that the Mo-N and Mo-Cu shells appear prominently in the FTs implies essential collinearity of the Mo-CN-Cu configuration. Although sample 4 also shows some weak contributions around 4.0–5.3 Å, these features can be ascribed to Cs contribution [19]. On the other hand, in the FTs of the Cu *K*-edge EXAFS of 1 and 2, contributions of the Cu-N (~1.6 Å), Cu-C(~2.7 Å), and Cu-Mo shell(~5.0 Å) are observable. On the contrary, in the FTs of (3), the corresponding Cu-C shell is quite weak and the Cu-Mo shell is completely missing. This is because the Cu-N-C angle is strongly bent (145°) and the multiple-scattering focusing effect is not important.

Fig.10 shows the Mo and Cu *K*-edge EXAFS functions $k^3\chi(k)$ and the FTs of (No2) before and after photoirradiation, taken in the fluorescence yield mode. The EXAFS oscillations are quite similar between the LT and photoinduced phases, although the EXAFS amplitude is noticeably reduced after photoirradiation. Curve-fitting analysis was performed for each contribution in *k* space. In order to obtain the backscattering amplitudes and the phase shifts, we have performed theoretical simulations using the FEFF (version 8.00)(Ref. 20) code for (No2–4) based on the reported crystal structures[15,16,19]. Since the

Mo-C-N-Cu configuration is nearly collinear, the EXAFS function of the higher-nearest neighbor (NN) shells such as Mo-N, Mo-Cu, Cu-C, and Cu-Mo should be given as a sum of all the corresponding single- and multiple-scattering components [21-24]. By summing up all the components, the one-shell analysis can be performed as in the first-NN single scattering cases. This simplification is physically valid when the Mo-C-N-Cu configuration is nearly collinear. This is because the interatomic distances and the Debye-Waller factors are all equal among these single- and multiple-scattering paths, as long as the dynamic effect mainly due to the bending vibration does not contribute so much to the reduction of the backscattering amplitudes [25-27]. Moreover, this simplification is mathematically valid even for noncollinear cases, although the interatomic distance and the Debye-Waller factor are not identical for each scattering path and the Debye- Waller factor obtained from the analysis corresponds to some average and is less physically meaningful. These treatments for the multiple-scattering paths are identical to our previous data analysis [6,7,9,10].

In the FTs of the Mo *K*-edge EXAFS (typical *k* range employed was 2.7~16.0 $Å^{-1}$), the three shells of Mo-C, Mo-N, and Mo-Cu are well separated from each other, and thus the single-shell analysis could be done. The *R* and *k* ranges employed were around 1.2–2.2 Å and 3.5–15.0 Å for Mo-C, 2.2–3.3 Å and 3.5–15.5 Å−1 for Mo-N, and 4.2–5.3 Å and 6.5–15.5 Å−1 for Mo-Cu, respectively. On the contrary, in the Cu *K*-edge EXAFS _typical *k* range employed in the FT was 2.8–15.3 Å−1_, weak contributions from the axial N and O atoms with longer distances should be overlapped between the first-NN

Cu-N_equatorial_ and the higher-NN Cu-C shells.

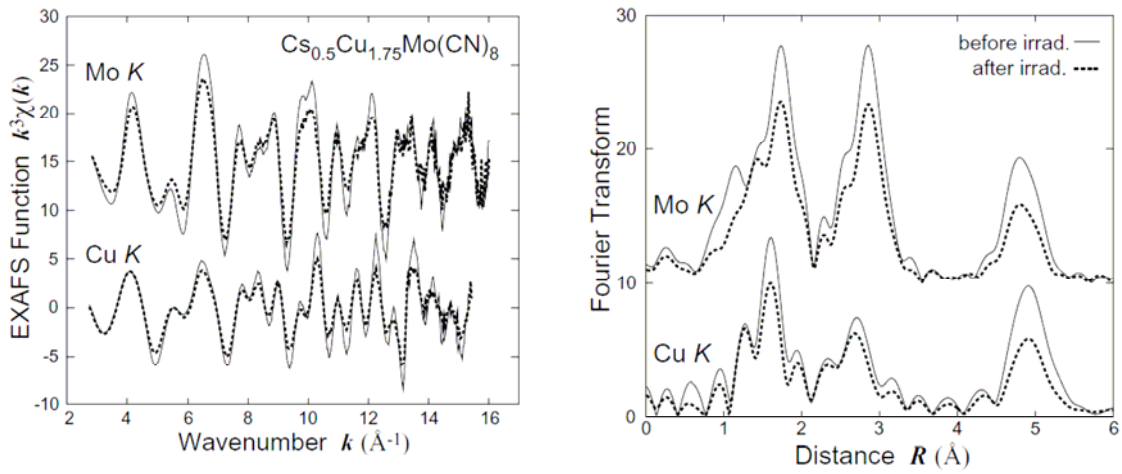

Fig.10 (Right) Mo and Cu K-edge EXAFS Oscillation functions $k^3\chi(k)$ and left Fourier transforms at 30K in the **fluorescence mode**

Thus the features appearing around 1.0–3.4 Å cannot be separated. A three -or five-shell curve fitting analysis was performed for these contributions, using the *R* and *k* ranges for the fitting of 1.1–3.4 Å and 4.0–15.0 $Å^{-1}$, respectively. The Cu-Mo shell for (No1 and No2) was treated as a single shell by employing the *R* and *k* ranges of 4.4–5.4 Å and 6.0–15.0 $Å^{-1}$, respectively.

The interatomic distances obtained are summarized in Tables I and II, while the coordination numbers are tabulated in Table III. Note that the errors shown in the tables are derived only from the statistical estimation in the fitting procedure, and no other contributions such as theoretical and/or model uncertainties are included. Examples of the curve fits are shown for the Mo-Cu and Cu-Mo shells in Fig. 11. Goodness of the curve fitting is excellent.

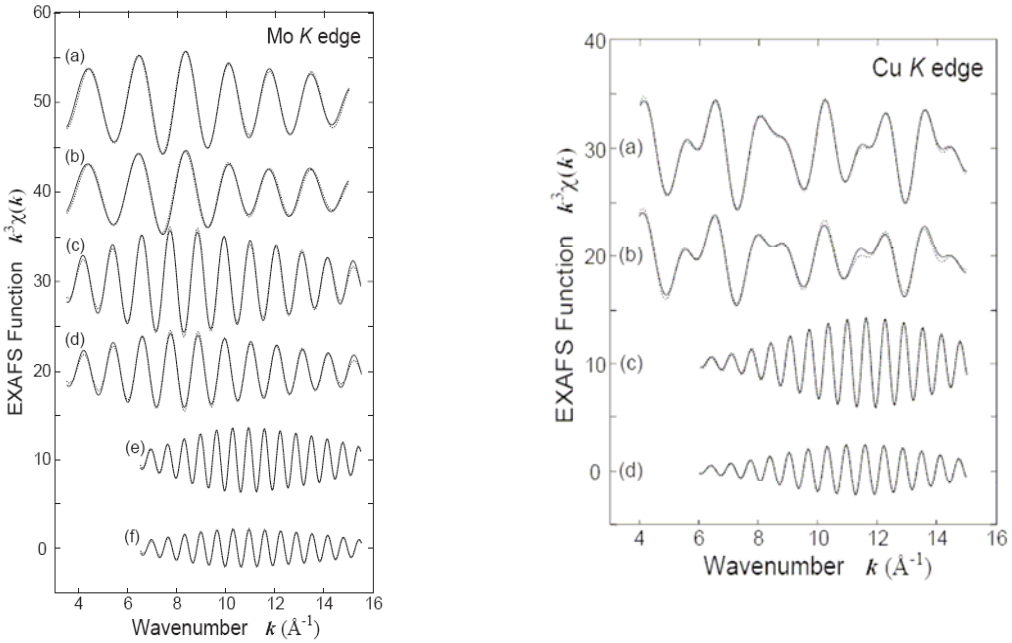

Fig.11 Right:Curve fitting plots for the Mo *K*-edge EXAFS analysis of No 2 before[(a),(c),(e)] and after [(b),(d),(f)] photoirradiation. (a,b) the Mo-C shell, (c,d) the Mo-N shell and (e,f) the Mo-Cu shell. Solid and dotted line denote the filtered and simulated $k^3\chi(k)$, respectively.Left: Curve fitting plots for the Cu *K*-edge EXAFS analysis of No 2 before[(a),(c)] and after [(b),(d)] photoirradiation. (a,b) the Cu-N,O,Cshell, (c,d) the Cu-Mo shell. Solid and dotted line denote the filtered and simulated $k^3\chi(k)$, respectively

It can be noted that the magnitudes of the EXAFS oscillations are considerably suppressed upon photoirradiation. Since the EXAFS oscillations of the photoinduced phases are still visible in the high *k* region as in the cases of the LT phases, the damping of the EXAFS amplitude is not mainly ascribed to the enhancement of the Debye-Waller factor but dominantly to the overall scale factor that normally originates from the coordination number. Let us first discuss the interatomic distances of the structurally known compounds by comparing to the x-ray crystallographic data. The average Mo-C distances are obtained as

2.168(3) Å for (No3) and 2.171(2) Å for (No4), and the average Mo-N distances are 3.326(2) and 3.311(2) Å, respectively. These results are in excellent agreement with the x-ray data[15,16] in Table I. In the LT phase of (No2) the obtained Mo-C and Mo-N distances of 2.159(3) and 3.310(2) Å are again in good agreement with the x-ray data[15]. From the crystal structure of (2), there exit three kinds of the Mo-Cu shells with the distances of 5.228 Å (N=2), 5.252 Å(N =2), and 5.548 Å (N=4/7). Since the EXAFS analysis of the Mo-Cu shell can be done within the one-shell analysis, the longer one may not be detected, while the closer one is consistent with the EXAFS results of 5.256(4) Å. Similarly, in the Cu K-edge EXAFS analysis, the longer Cu-Mo shell is not seen. The Cu-Mo

Table I Results of the CF analysis of Mo K-edge EXAFS

Table II Results of the CF analysis of Cu K-edge EXAFS

Sample		Shell	S_0^2N	R (Å)	C_2 (10^{-2} Å^2)	χ_ν^2
No1	LT	Cu-N(eq)	4.1(3)	1.946	0.55	
		Cu-O(ax)	[2.0]	2.183	1.81	
		Cu-C(eq)	2.7(4)	3.076	0.48	
		Cu-Mo(eq)	2.1(4)	5.201	0.63	2.95
	PI	Cu-N(eq)	4.0(4)	1.947	0.85	
		Cu-O(ax)	[2.0]	2.197	1.71	
		Cu-C(eq)	2.5(4)	3.085	0.58	
		Cu-Mo(eq)	1.2(5)	5.197	0.75	1.46
No2	LT	Cu-N(eq)	[4.0]	1.986	0.31	
		Cu-N(ax)	[1.43]	2.228	0.18	
		Cu-O(ax)	[0.57]	2.694	0.15	0.85
		Cu-C(eq)	[4.0]	3.130	0.48	
		Cu-C(ax)	[0.57]	3.351	0	
	PI	Cu-Mo(eq)	2.4(2)	5.270	0.39	
		Cu-N(eq)	[4.0]	1.988	0.52	
		Cu-N(ax)	[1.43]	2.230	0.16	
		Cu-O(ax)	[0.57]	2.693	0.25	0.15
		Cu-C(eq)	[4.0]	3.133	0.58	
		Cu-C(ax)	[0.57]	3.348	0.02	
		Cu-Mo(eq)	1.8(2)	5.277	0.49	

R (Å) *From XRD*	
Cu-N(eq)	1.949
Cu-N(ax)	2.234
Cu-O(ax)	2.478
Cu-O(eq)	2.842
Cu-C(eq)	3.092
Cu-C(ax)	3.379
Cu-Mo(eq)	5.240
Cu-Mo(eq)	5.548

Hozumi et al. J. Am. Chem. Soc. 127, 3864 (2005)

distance of (No2) before photoirradiation is obtained as 5.270(3) Å(see Table II), which agrees fairly well with the Mo-Cu distance. The Cu-N distance in (No2) seems a little different from that in (No1): 1.946(6) and 1.986(4) Å for(No1 and No2), respectively. This difference is also reflected in the Cu-Mo/Mo-Cu distances: 5.233(5)or 5.201(9) Å for (No1) and 5.256(4) or 5.270(3) Å for (No2). This may originate from a different environment around Cu. These results obtained indicate that the present analysis is reliable to discuss the structures of the photoinduced phases.

As apparent in Table I and II, the coordination numbers of the Mo-N, Mo-Cu, and Cu-Mo shells deviate from the real values, although those of the first-NN Mo-C shells are estimated rather accurately. Especially, the deviations of the Mo-Cu and Cu-Mo shells are significant. This discrepancy can be understood in the following manner. These higher-NN shell contributions contain a strong multiple-scattering process because of the almost collinear arrangement of the Mo -C-N-Cu path. When the bond angle deviates from 180° statically or dynamically, the EXAFS amplitude is rapidly reduced. This effect cannot be described within a simple Gaussian distribution function [25-27]. We can use the effect of the amplitude reduction as a semiquantitative indicator of the bond bending.

Local structural around Cu^{II} Before photomagnetic phase transition

The local structures of (No1) and (No2) before photoirradiation can be discussed based on the standard mentioned above. As shown in Table III, Compared to the

theoretical value(marked by *[ ]*), strong reduction can be seen in the second and third NN shell around Mo and Cu center. This indicates there is a distortion from the collinear bond arrangement.

Apparent coordination numbers of No.1 sample

	Mo-C	Mo-N	Mo-Cu
LT	8.4(4)	5.7(3) *[8]*	3.5(3) *[8]*
	Cu-N(eq)	**Cu-C(eq)**	**Cu-Mo(eq)**
LT	[4.0]	[4.0] *[4]*	2.4(2) *[4]*

Apparent coordination numbers of No.2 sample

	Mo-C	Mo-N	Mo-Cu
LT	8.3(4)	5.6(3) *[8]*	2.8(3) *[8]*
	Cu-N(eq)	**Cu-C(eq)**	**Cu-Mo(eq)**
LT	4.1(3)	2.7(4) *[4]*	2.1(4) *[4]*

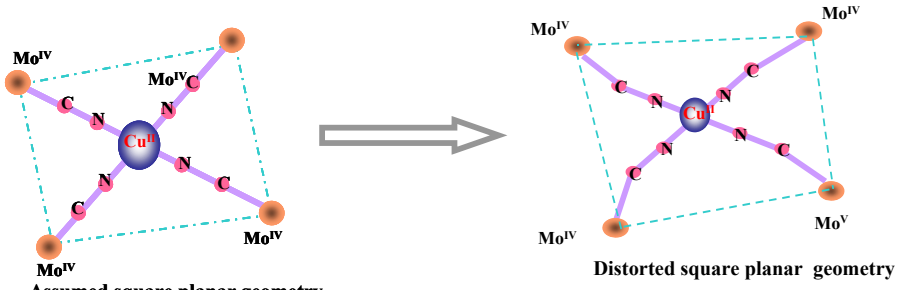

Assumed square planar geometry

(a)

Distorted square planar geometry

(b)

Table III

The curve fitting was performed according to the assumed square planar geometry [Model:(a)]. However, the curve fitting results reveals that there exists a distortion aroundthe Cu^{II} center and the final local structure is schematically expressed in the model (b). This result also suggests that the single crystal XRD results are not always reliable when it comes to discuss the local structure.

Let us now discuss the local structure of No 1 and No 2 sample after photoirradiation. The interatomic distances do not vary compared to those before photoirradiation, as given in Tables I and II. Differences between the LT and photoinduced phases can, however, be detected in the amplitude in the EXAFS oscillation. This was already seen in the EXAFS functions or the FTs in Fig. 10. From the curve-fitting results, the coordination numbers of the Mo-N, Mo-Cu,

and Cu-Mo shells are found to be reduced further compared to those before photoirradiation, while those of the Mo-C and Cu-N(eq) shells remain almost unchanged. The reduction of the EXAFS amplitude for the first-NN shells implies the enhancement of the static Debye-Waller factors. On the contrary, the apparent reduction of the coordination numbers for the higher-NN Mo-N, Mo-Cu, and Cu-Mo shells can be ascribed not to the breaking of the Mo-C bond but to the bending of the Mo-CN bond. The Cu-C coordination numbers in No2, however, do not vary so much upon photoirradiation. Although the curve-fitting analysis of the Cu *K*-edge EXAFS of No 1 was conducted by fixing the coordination numbers and it is hard to recognize whether the Cu-NC bond is also bent in the

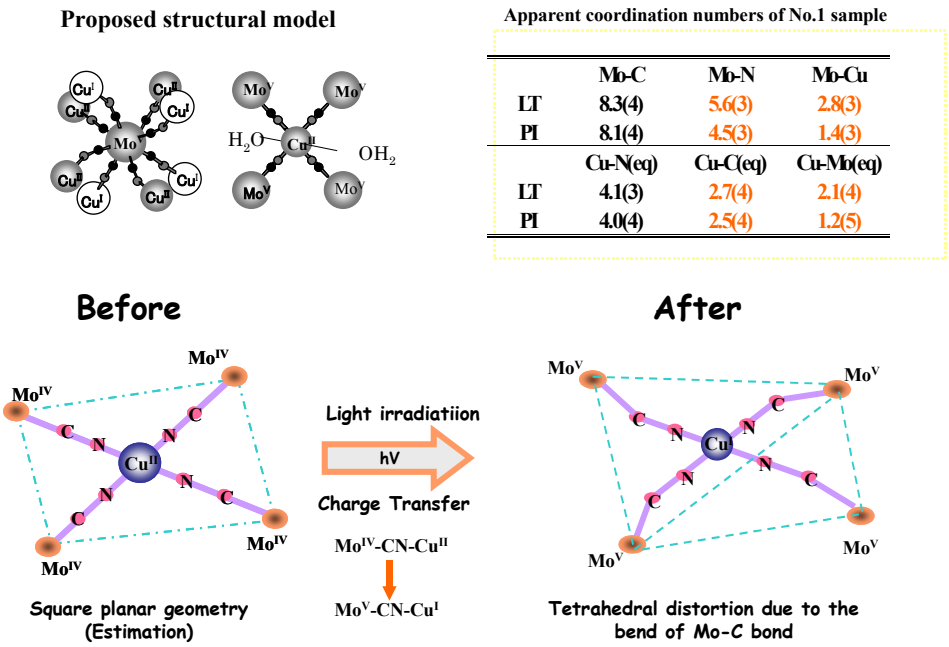

Fig.11 Schematic local structure of No.1 sample after photoirradiation

photoinduced phase. We have, however, verified that when the coordination

number of the Cu-C shell is assumed to be a smaller value, the resultant reliability factor becomes worse. These findings indicate that upon photoirradiation the Cu-N-C bond angles are left almost unchanged, while the Mo-C-N bond is bent (shown in Fig.11,12).

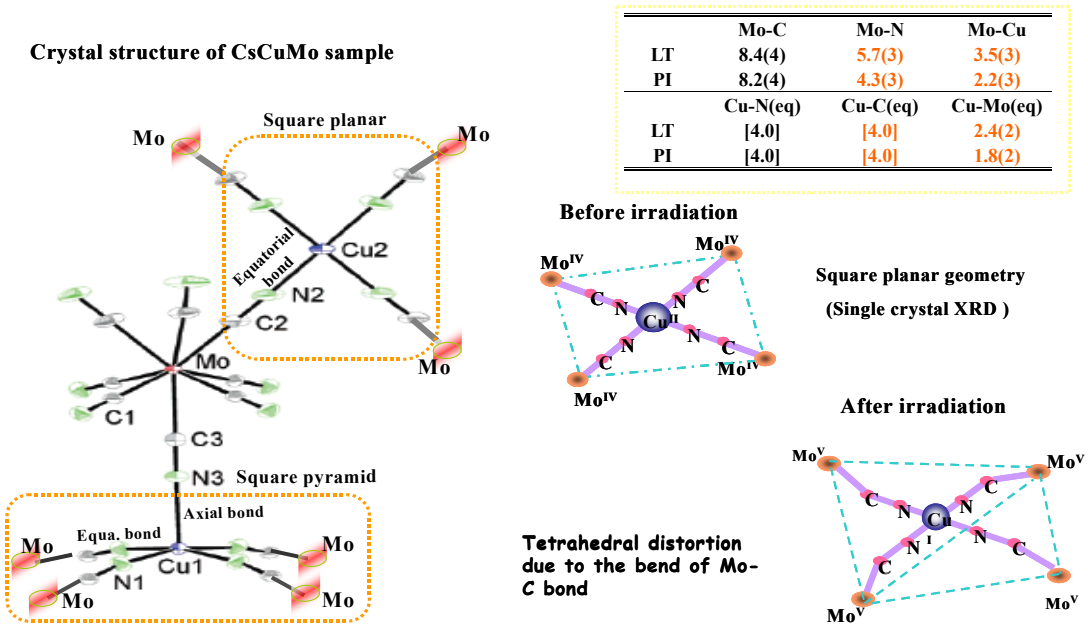

Fig.12 Schematic local structure of No.2sample after photoirradiation

It may ideally be possible to deduce the bent angles by performing the theoretical simulations [22-25]. In the present case, however, the photoinduced state contains both Cu^{I} and Cu^{II} even when the photoinduced phase transition is completed. The Cu^{I} : Cu^{II} ratio is at most 1.0 in No1 and should be a little smaller in the present experiments. Moreover, there exist two inequivalent Cu sites in No2 and the situation is more complicated. Although we have tried to estimate the bent angles by the FEFF simulations in No 2, the results should include much uncertainty and it might be better not to discuss the bent angles quantitatively.

The $Cu(NC)_4$ unit is inherently planar before photoirradiation because of the stability of the square planar structure in Cu^{II}, and the $Cu(NC)_4$ unit exhibits slight tetrahedral distortion after photoirradiation, which should be more stable in Cu^{I}. The tetrahedral distortion can also be understood from the electronic configuratio. Compared with Cu^{II} where $3d^9$ is configured, see the Fig.13, the 3d orbit of Cu^{I} is completely occupied. This closed electronic shell structure prefers non- directional geometry such as spherical configuration while tetrahedral is most closest to be spherical symmetry. Therefore during the redox process of Cu^{II} site being replaced by Cu^{I} site, there is strong tetrahedral deformation force which causes a bond-bending around the Cu^{I} site

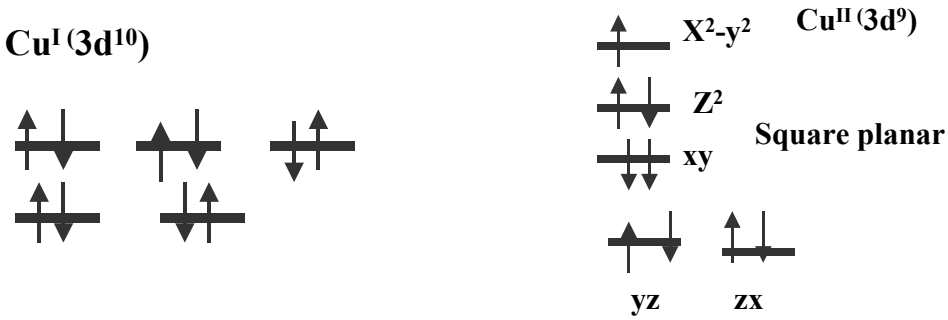

Fig.13 Electronic configuration for the reduced Cu^{I}

5.5 Discussion

1 Determination of the active site during phase transition

As shown in the crystal structure for No 2 sample, there are two Cu sites, Cu1with square pyramid geometry and Cu2 with square planar. The question raised here is which site is the active site during photoirradiation. The technique such as ESR and IR has been used but failed to probe the slight difference between these two sites. Recently a solid state NMR spectra was performed at University of Hokaido on CuMo sample and CsCuMo sample in which the $(CN)^-$

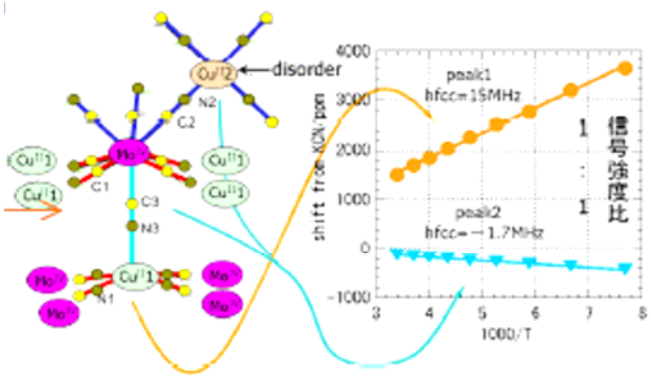

1 $(CN)^-$ ligand is enriched by C^{13}.
2 hfcc: hyper fine coupling constants which was used to evaluate the distortion degree of local structure.
Fig.14 Solid state NMR(C^{13}) results

is enriched by C^{13}. Their results (see Fig.14) have shown that before photoirradiation, for CuMo sample, a distortion from square planar geometry around Cu^{II} is found, while for CsCuMo sample, where there exists two Cu sites, they found distortion around $Cu(2)^{II}$ more pronounced than the one around $Cu(1)^{II}$. Although no photoirradiation experiment was carried out, one can presumably conclude that $Cu(2)^{II}$ site play more active reduction trole than the

Cu(1) during phase transition from Cu^{II} to Cu^{I}. To our research, these results also verified the distorted square planar structure for No1 and No2 sample, where a distortion was found from the curve fitting results.

2 Opposing view on local structure around Cu^{I} in one biological study

Although the present remark concerning the local structure changes in the reduction of Cu is rather qualitative, this information is essential because structural changes in the Cu redox processes have been attractive for various

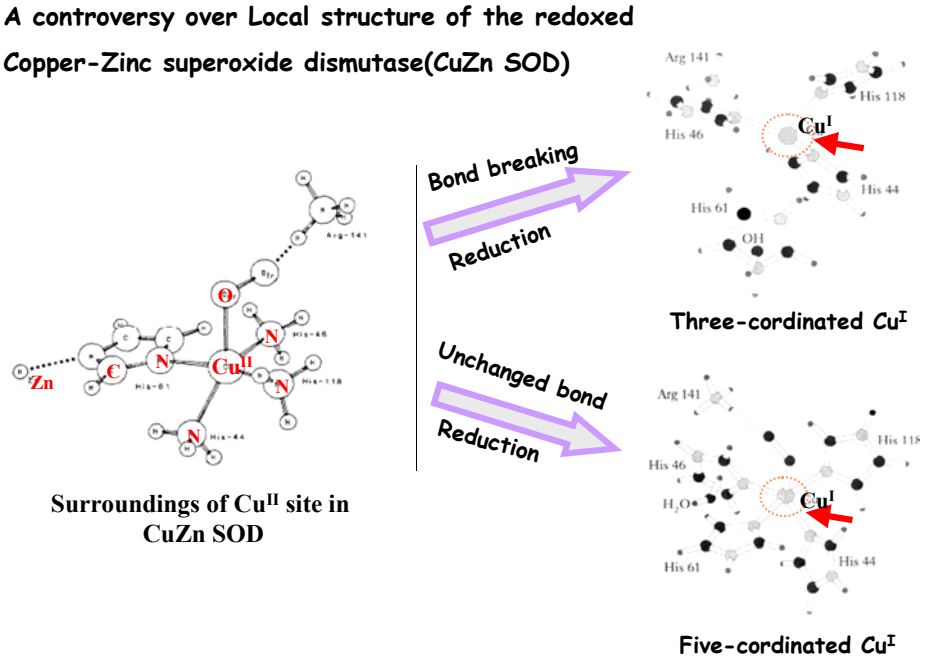

Fig.15 EXAFS results of local structure for CuZn superoxide dismutase

scientific fields. For instance, in CuZn superoxide dismutase, it is not yet settled whether Cu^{I} is coordinated by three or five ligands after reduction[28-30]. Both models (shown in Fig.15) are based on the fact that the square planar geometry is unstable at the Cu^{I} site. Although our present model may not match the case of CuZn superoxide dismutase, this model is in general worthwhile, taking into

account when one wants to discuss the structural changes in the Cu redox cycle.

Conclusion:

In this work, we have performed the XAFS study of the photoinduced phases of the CuMo cyanides. We found direct evidence for the charge transfer phase transition from the Cu *K*-edge XANES: Divalent Cu is reduced to monovalent after photoirradiation. Although the changes in the interatomic distances are not found, the EXAFS results qualitatively indicate that in the photoinduced phase, the Mo-CN bond is bent while the Cu-NC bond bending is left unchanged, possibly due to slight tetrahedral distortion at the Cu(I) site.

Reference:

[1]. O. Sato, T. Iyoda, A. Fujishima, and K. Hashimoto, Science 271, 49 (1996).

[2]. A. Bleuzen, C. Lomenech, et al, J. Am. Chem. Soc. 122, 6648 (2000).

[3]. O. Sato et al Inorg.Chem. 199,38, 4405-4412 (1999)

[4]. S. Ferlay, T. Mallah, et al, Nature (London) 378, 701 (1995).

[5]. S. Ohkoshi, et al, J. Phys. Chem. 104, 9365 (2000).

[6]. T. Yokoyama, T. Ohta, O. Sato, et al, Phys. Rev. B 58, 8257 (1998).

[7]. T. Yokoyama, M. Kiguchi, et al, Phys. Rev. B 60, 9340 (1999).

[8]. C. Cartier dit Moulin, F. Villain, et al, J. Phys. Chem. 122, 6653 (2000).

[9]. T. Yokoyama, K. Okamoto, et al, Phys. Rev. B 65, 064438 (2002).

[10]. T. Yokoyama, H. Tokoro, et al, Phys. Rev. B 66, 184111 (2002).

[11]. S. Ohkoshi, N. Machida, Z.-J. Zhong, et al, Synth. Met. 122, 523 (2001).

[12]. S. Ohkoshi, N. Machida, et al, Chem. Lett. 2001, 312(2001).

[13]. G. Rombaut, M. Verelst, et al, Inorg. Chem. 40, 1151 (2001).

[14]. G. Rombaut, C. Mathonière, et al, Inorg. Chim. Acta 326, 27 (2001).

[15]. T. Hozumi, K. Hashimoto, and S. Ohkoshi, J. Am. Chem. Soc. 127, 3864 (2005).

[16]. J. B. Goodenough, Phys. Rev. 100, 564 (1959)

[17]. J. B. Goodenough, J. Phys. Chem. Solids 6, 287 (1958)

[18]. J. Kanamori, J. Phys. Chem. Solids 10, 87 (1959) [CAS].

[19]. J. Larionova, R. Clérac, et al, Cryst. Growth Des. 3, 267 (2003).

[20]. S. S. Basson, J. G. Leipoldt, et al, Cryst. Chem. 36, 176 (1980).

[21]. A. L. Ankudinov, B. Ravel, et al, Phys. Rev. B 58, 7565 (1998).

[22]. B. K. Teo, J. Am. Chem. Soc. 105, 1144 (1983). [Inspec]

[23]. H. I. Liu, A. Filipponi, et al, J. Am. Chem. Soc. 116, 2418 (1994).

[24]. H. H. Zhang, A. Filipponi, et al, J. Am. Chem. Soc. 119, 2470 (1994).

[25]. M. Giorgetti, M. Berrettoni, et al, Chem. Phys. Lett. 275, 108 (1997).

[26]. A. Filipponi, A. Di Cicco, et al, Phys. Rev. B 52, 15122 (1995).

[27]. A. Filipponi and A. Di Cicco, Phys. Rev. B 52, 15135 (1995).

[28]. T. Yokoyama and T. Ohta, J. Phys. Soc. Jpn. 65, 3909 (1996).

[29]. W. E. Blumberg, J. Peisach, et al, Biochemistry 17, 1842 (1978).

[30]. R. Osman and H. Basch, J. Am. Chem. Soc. 106, 5710 (1984).

6 Conculsions:

In this thesis, I have succeeded in the investigation of the critical behavior and magnetic anisotropy of Co nanorods within several atoms range. The novel results from this research is expected to bridge the gap between magnetic properties of atomic-chain and large scale nanorods(>20nm). Meanwhile, the critical behavior observed is for the first pioneering report regarding one-dimensional magnetic nanostructure.. The theoretical model presented for large broadening critical behavior can also generalize into the common one-dimensional nanomaterial. These results are expected to stimulate the more thorough research in this respect.

The magnetization curves recorded by the magneto-optical Kerr effect (MOKE) clarify that the magnetic easy axis is perpendicular to the rod axis within the substrate plane, implying that the magnetic anisotropy is not dominated by the shape anisotropy. The x-ray magnetic circular dichroism measurement presents a significant enhancement of the orbital magnetic moment along the easy axis compared to the hard axes, confirming that the spin-orbit interaction determines the easy axis. The critical behaviors of the Co nanorods show that the critical exponent β is much larger than the value expected from the two-dimensional Ising model. By performing the Monte-Carlo simulations based on single domain model and multiple spin segment model, the staggered suppression of the magnetization around the critical temperature is undoubtfully ascribed to the finite length of the Co nanorods.

Meanwhile, the chemisorption effect on the magnetic anisotropy of Fe ultrathin film on Ag(001) surface is also studied systemically in this thesis. It is found by the MOKE that adsorption of O_2 and NO induces the shift of the critical thickness for the transitions to a thinner side, together with the suppression of the remanent magnetization and the coercive field of the Fe film. This implies destabilization of the

perpendicular magnetic anisotropy. On the other hand, H_2 adsorption is found not to change the magnetic anisotropy, though the enhancement of the coercive field is observed. The XMCD reveals that although both the spin and orbital magnetic moments along the surface normal are noticeably reduced upon O_2 and NO adsorption, the reduction of the orbital magnetic moments are more significant. This indicates that the destabilization of the perpendicular magnetic anisotropy upon chemisorption of O_2 and NO originates from the change of the spin-orbit interaction at the surface.

In the last part of this thesis I have succeeded in determining of local structure and electronic state of a novel unique molecular photomagnets of Cu-Mo cyanides. A direct evidence for the reduction of divalent Cu to monovalent is detected by Cu *K*-edge x-ray-absorption near-edge structure. The extended x-ray-absorption fine-structure confirms that the interatomic distances around Cu and Mo in the photoinduced phase are almost identical to those of the initial low temperature phase. The higher-nearest neighbor coordination numbers, however, are apparently reduced. We have interpreted this as the result of the bending of the Mo-CN bond due to the tetrahedral distortion around the monovalent Cu(I) site.

Acknowledgements

First of all, I would like to thank and express my deepest gratitude to Pro. Dr. Toshihiko Yokoyama for having given me the opportunity to work in his research group and introduced me into the fantastic world of nanomagnetism physics. His ongoing support has made it possible to pursue the different arguments treated in the present work. His competence, profound theoretical knowledge and persistent interest in all the works were for me extremely precious and will always guide me along the right track in the future research career.

I am grateful to Pro. Dr. Nobuyuki Nishi for association with supervising my Ph.D work.

I would like to, especially to thank Dr. Takeshi Nakagawa. His broad knowledge in all aspects in surface science and magnetism on ultrathin films is very impressive. Thanks for his support during all the stage in this work. His opinion and comments on physics are full significant meaning. I learnt a lot from his experience to approach and experimental setup.

I warmly thank all co-workers at Prof. Dr. Kazuhito Hashimoto research group, especially Dr. Toshiya Hozumi, and Prof.Dr. Shin-ichi Ohkoshi for their kindness and assistance in providing the CuMo Cyanide samples to me.

I am indebted to Prof. Dr.Toyohiko, Kinoshita and Prof. Dr. Yukio, Hasegawa for their intensive supervisions during my stay at ISSP (Buseiken) at University of Tokyo. The fundamental knowledge and technique in surface science that I learnt from them has contributed a lot to all my Ph.D works.

I would also like to address my deep appreciation to all the staff at UVSOR, who has provided a great deal of assistance both during my beam time in XMCD

experiments and off beam time.

I thank the crew of the mechanical workshop for their help and support during all my Ph.D work.

I thank also Ms. Madomi Noto for her support both in research and administration affairs.

Finally, I would like to thank the most important persons in my life, my parents who believed in and support my choice, my wife and my son who gives me so much courage and makes my life more fruitful and much sweeter.